# SWAN

## SCIENTIFIC
## AND
## TECHNICAL
## DOCUMENTATION

**SWAN Cycle III version 41.31AB**

# SWAN
# SCIENTIFIC AND TECHNICAL
# DOCUMENTATION

| | | |
|---|---|---|
| by | : | The SWAN team |
| mail address | : | Delft University of Technology |
| | | Faculty of Civil Engineering and Geosciences |
| | | Environmental Fluid Mechanics Section |
| | | P.O. Box 5048 |
| | | 2600 GA Delft |
| | | The Netherlands |
| e-mail | : | swan-info-citg@tudelft.nl |
| home page | : | *http://www.swan.tudelft.nl* |

# Contents

# Chapter 1

# Introduction

The main goal of the SWAN model is to solve the spectral action balance equation without any *a priori* restrictions on the spectrum for the evolution of wave growth. This equation represents the effects of spatial propagation, refraction, shoaling, generation, dissipation and nonlinear wave-wave interactions. The basic scientific philosophy of SWAN is identical to that of WAM cycle 3. SWAN is a third-generation wave model and it uses the same formulations for the source terms.

Whereas the WAM model considers problems on oceanic scales, with SWAN wave propagation is calculated from deep water to the surf zone. Since, WAM makes use of explicit propagation schemes in geographical and spectral spaces, it requires very small grid sizes in shallow water and is thus unsuitable for applications to coastal regions. For that reason, SWAN employs implicit schemes, which are more robust and economic in shallow water than the explicit ones. Note that SWAN may be less efficient on oceanic scales than WAM.

## 1.1 Historical background

Over the past two decades, a number of advanced spectral wind-wave models, known as third-generation models, has been developed such as WAM (WAMDI Group, 1988), WAVE-WATCH III (Tolman, 1991), TOMAWAC (Benoit *et al.*, 1996) and SWAN (Booij *et al.*, 1999). These models solve the spectral action balance equation without any *a priori* restrictions on the spectrum for the evolution of wave growth.

Based on the wave action balance equation with sources and sinks, the shallow water wave model SWAN (acronym for S̲imulating WA̲ves N̲earshore) is an extension of the deep water third-generation wave models. It incorporates the state-of-the-art formulations for the deep water processes of wave generation, dissipation and the quadruplet wave-wave interactions from the WAM model (Komen *et al.*, 1994). In shallow water, these processes have been supplemented with the state-of-the-art formulations for dissipation due to bottom friction, triad wave-wave interactions and depth-induced breaking. SWAN is fully spectral (in all directions and frequencies) and computes the evolution of wind waves in coastal regions

with shallow water and ambient current.

SWAN is developed at Delft University of Technology and is freely available at *http://www.swan.tudelft.nl.* It is used by many goverment authorities, research institutes and consultants worldwide. The feedback has widely indicated the reliability of SWAN in different experiment and field cases.

Initially, the SWAN cycle 1 was formulated to be able to handle only stationary conditions on a rectangular grid. Later on, SWAN cycle 2 model has been developed. This is considered as the second step in the development of SWAN models. Cycle 2 of SWAN is stationary and optionally nonstationary. It can compute the wave propagation not only on a regular rectangular grid, but also on a curvilinear grid. Previous official versions 30.62, 30.75, 40.01 and 32.10 belong to the cycle 2 of SWAN.

This section is under preparation.

## 1.2   Purpose and motivation

The purpose of this document is to provide relevant information on the mathematical models and numerical techniques for the simulation of spectra of random short-crested, wind-generated waves in coastal regions. Furthermore, this document explains the essential steps involved in the implementation of various numerical methods, and thus provides an adequate reference with respect to the structure of the SWAN program.

## 1.3   Readership

This document is, in the first place, addressed to those, who wish to modify and to extend mathematical and numerical models for shallow wind-wave problems. However, this material is also useful for those who are interested in the application of the techniques discussed here. The text assumes the reader has basic knowledge of analysis, partial differential equations and numerical mathematics and provides what is needed both in the main text and in the appendices.

## 1.4   Scope of this document

SWAN is a third-generation wave model for obtaining realistic estimates of wave parameters in coastal areas, lakes and estuaries from given wind, bottom and current conditions. However, SWAN can be used on any scale relevant for wind-generated surface gravity waves. The model is based on the wave action balance equation (or energy balance in the absence of currents) with sources and sinks. Good introductory texts on the background of SWAN are Young (1999) and Booij *et al.* (1999).

The following wave <u>propagation</u> processes are represented in SWAN:

- propagation through geographic space,

- refraction due to spatial variations in bottom and current,

- diffraction,

- shoaling due to spatial variations in bottom and current,

- blocking and reflections by opposing currents and

- transmission through, blockage by or reflection against obstacles.

The following wave <u>generation and dissipation</u> processes are represented in SWAN:

- generation by wind,

- dissipation by whitecapping,

- dissipation by depth-induced wave breaking,

- dissipation by bottom friction and

- wave-wave interactions in both deep and shallow water.

In addition, the wave-induced set-up of the mean sea surface can be computed in SWAN. However, wave-induced currents are not computed by SWAN. In 1D cases, computation of wave-induced set-up is based on exact shallow water equations, whereas in 2D cases they need to be approximated since the effects of wave-induced currents are ignored.

Diffraction is modelled in a restrict sense, so the model should be used in areas where variations in wave height are large within a horizontal scale of a few wave lengths. However, the computation of diffraction in arbitrary geophysical conditions is rather complicated and requires considerable computing effort. To avoid this, a phase-decoupled approach, as described in (Holthuijsen *et al.*, 2003), is employed so that same qualitative behaviour of spatial redistribution and changes in wave direction is obtained. This approach, however, does not properly handle diffraction in harbours or in front of reflecting obstacles.

SWAN is stationary and optionally nonstationary and can be applied in Cartesian or curvilinear (recommended only for small scales) or spherical (small scales and large scales) co-ordinates. The stationary mode should be used only for waves with a relatively short residence time in the computational area under consideration, i.e. the travel time of the waves through the region should be small compared to the time scale of the geophysical conditions (wave boundary conditions, wind, tides and storm surge).

## 1.5   Overview

The remainder of this document is subdivided as follows: In Chapter 2 the action balance equations used in SWAN are presented. Next, each source term of the governing equations is in depth described. In Chapter 3 the main characteristics of the finite difference method for the discretization of the governing equations in irregular horizontal planes are outlined. Various differencing schemes for spatial propagation are reported. Chapter 4 is concerned with discussing several boundary conditions and their implementation. Chapter 5 is devoted to the design of the two-dimensional wave set-up of sea surface. Chapter 6 is devoted to the linear solvers for the solution of the resulted linear systems of equations. Chapter 7 deals with some consideration on parallelization of SWAN on distributed memory architectures. Chapter 8 presents an unstructured-grid procedure for SWAN. Chapter 9 concludes this document by summarizing the overall solution algorithm of SWAN.

This document, however, is not intended as being complete. Although, this document describes the essential steps involved in the simulation of waves, so that the user can see which can be modified or extended to solve a particular problem properly, some issues involved in SWAN are not included. Below, a list of these issues is given, of which the information may be available elsewhere:

- reflection,

- iterative solvers,

- overall solution algorithm.

## 1.6   Acknowledgements

Transport, Public Works and Water Management, The Netherlands).

We are finally grateful to all those other people working on the Public Domain Software without which the development of SWAN would be unthinkable: Linux, Intel, GNU F95, LaTeX, MPICH2, Perl and many others.

# Chapter 2

# Governing equations

## 2.1 Spectral description of wind waves

Wind generated waves have irregular wave heights and periods, caused by the irregular nature of wind. Due to this irregular nature, the sea surface is continually varying, which means that a deterministic approach to describe the sea surface is not feasible. On the other hand, statistical properties of the surface, like average wave height, wave periods and directions, appear to vary slowly in time and space, compared to typical wave periods and wave lengths. The surface elevation of waves in the ocean, at any location and any time, can be seen as the sum of a large number of harmonic waves, each of which has been generated by turbulent wind in different places and times. They are therefore statistically independent in their origin. According to linear wave theory, they remain independent during their journey across the ocean. Under these conditions, the sea surface elevation on a time scale of one hundred characterstic wave periods is sufficiently well described as a stationary, Gaussian process. The sea surface elevation in one point as a function of time can be described as

$$\eta(t) = \sum_i a_i \cos(\sigma_i t + \alpha_i) \tag{2.1}$$

with $\eta$ the sea surface elevation, $a_i$ the amplitude of the $i^{\text{th}}$ wave component, $\sigma_i$ the relative radian or circular frequency of the $i^{\text{th}}$ wave component in the presence of the ambient current (equals the absolute radian frequency $\omega$ when no ambient current is present) and $\alpha_i$ the random phase of the $i^{\text{th}}$ wave component. This is called the random-phase model.

In the presence of the ambient current, it is assumed that it is uniform with respect to the vertical co-ordinate and the changes in the mean flow within a wave length are so small that they affect only negligibly the dispersion relation. The absolute radian frequency $\omega$ then equals the sum of the relative radian frequency $\sigma$ and the multiplication of the wave number and ambient current velocity vectors:

$$\omega = \sigma + \vec{k} \cdot \vec{u} \tag{2.2}$$

7

which is the usual Doppler shift. For linear waves, the relative frequency is given by

$$\sigma^2 = gk \tanh(kd) \tag{2.3}$$

where $g$ is the acceleration of gravity and $d$ is the water depth.

Ocean waves are chaotic and a description in the time domain is rather limited. Alternatively, many manipulations are more readily described and understood with the variance density spectrum, which is the Fourier transform of the auto-covariance function of the sea surface elevation:

$$E'(f) = \int_{-\infty}^{+\infty} C(\tau)e^{-2\pi i f \tau} d\tau \tag{2.4}$$

with

$$C(\tau) = < \eta(t)\eta(t+\tau) > \tag{2.5}$$

where $C(\tau)$ is auto-covariance function, $<>$ represents mathematical expectation of random variable and $\eta(t)$, $\eta(t+\tau)$ represent two random processes of sea surface elevation, $\tau$ represents the time lag.

In the field of ocean wave theory it is conventional to degfine a spectrum $E(f)$ slightly different from the above one:

$$E(f) = 2E'(f) \quad \text{for } f \geq 0 \quad \text{and } E(f) = 0 \quad \text{for } f < 0 \tag{2.6}$$

The description of water waves through the defined variance density spectrum $E(f)$ is called spectral description of water waves. It can be proved that the variance of the sea surface elevation is given by

$$< \eta^2 > = C(0) = \int_0^{+\infty} E(f) df \tag{2.7}$$

which indicates that the spectrum distributes the variance over frequencies. $E(f)$ should therefore be interpreted as a variance density. The dimensions of $E(f)$ are $m^2/Hz$ if the elevation is given in $m$ and the frequencies in $Hz$.

The variance $< \eta^2 >$ is equal to the total energy $E_{\text{tot}}$ of the waves per unit surface area if multiplied with a properly chosen coefficient:

$$E_{\text{tot}} = \frac{1}{2}\rho_w g < \eta^2 > \tag{2.8}$$

The terms *variance density spectrum* and energy density spectrum will therefore be used indiscriminately in this document.

In many wave problems it is not sufficient to define the energy density as a function of frequency alone. It is mostly required to distribute the wave energy over directions as well. This spectrum, which distributes the wave energy over frequencies and directions, will be

denoted with $E(f, \theta)$. As the total energy density at a frequency $f$ is dstributed over the directions $\theta$ in $E(f, \theta)$, it follows that:

$$E(f) = \int_0^{2\pi} E(f, \theta) d\theta \tag{2.9}$$

The energy density spectrum $E(f)$ and $E(f, \theta)$ are depicted in Figure 2.1. Based on the energy density spectrum, the integral wave parameters can be obtained. These parameters
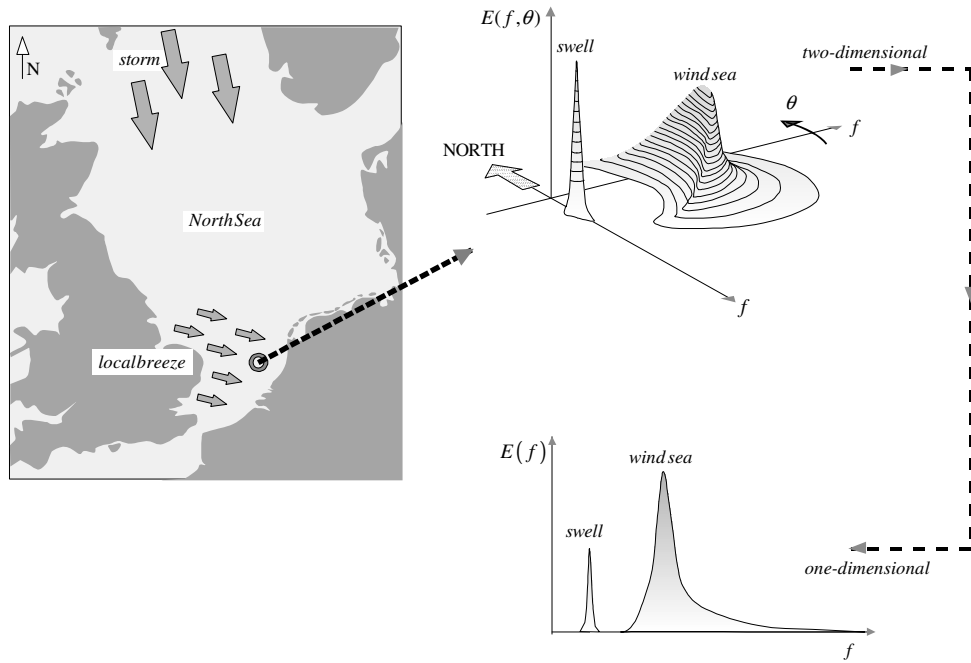


Figure 2.1: Illustrations of 1D and 2D wave spectra. (Reproduced from Holthuijsen (2007) with permission of Cambridge University Press.)

can be expressed in terms of the so-called $n-$th moment of the energy density spectrum:

$$m_n = \int_0^\infty f^n E(f) df \tag{2.10}$$

So, the variance of the sea surface elevation is given by $m_0 = <\eta^2>$. Well-known parameters are the significant wave height:

$$H_s = 4\sqrt{m_0} \tag{2.11}$$

and some wave periods:

$$T_{m01} = \frac{m_0}{m_1}, \quad T_{m02} = \sqrt{\frac{m_0}{m_2}}, \quad T_{m-10} = \frac{m_{-1}}{m_0} \tag{2.12}$$

In SWAN, the energy density spectrum $E(\sigma, \theta)$ is generally used. On a larger scale the spectral energy density function $E(\sigma, \theta)$ becomes a function of space and time and wave dynamics should be considered to determine the evolution of the spectrum in space and time. For brevity, the notation $E(\sigma, \theta)$ will still be used.

## 2.2 Propagation of wave energy

### 2.2.1 Wave kinematics

Using the linear wave theory and the conversion of wave crests, the wave propagation velocities in spatial space within Cartesian framework and spectral space can be obtained from the kinematics of a wave train (Whitham, 1974; Mei, 1983):

$$\frac{d\vec{x}}{dt} = (c_x, c_y) = \vec{c_g} + \vec{u} = \frac{1}{2}\left(1 + \frac{2|\vec{k}|d}{\sinh(2|\vec{k}|d)}\right)\frac{\sigma\vec{k}}{|\vec{k}|^2} + \vec{u} \tag{2.13}$$

$$\frac{d\sigma}{dt} = c_\sigma = \frac{\partial\sigma}{\partial d}\left(\frac{\partial d}{\partial t} + \vec{u}\cdot\nabla_{\vec{x}}d\right) - c_g\vec{k}\cdot\frac{\partial\vec{u}}{\partial s}$$

$$\frac{d\theta}{dt} = c_\theta = -\frac{1}{k}\left(\frac{\partial\sigma}{\partial d}\frac{\partial d}{\partial m} + \vec{k}\cdot\frac{\partial\vec{u}}{\partial m}\right)$$

where $c_x$, $c_y$ are the propagation velocities of wave energy in spatial $x-$, $y-$space, $c_\sigma$ and $c_\theta$ are the propagation velocities in spectral space $\sigma-$, $\theta-$space, $d$ is water depth, $s$ is the space co-ordinate in the wave propagation direction of $\theta$ and $m$ is a co-ordinate perpendicular to $s$. The expression for $c_\theta$ is presented here without diffraction effects. These are treated separately in Section 2.7.4.

Furthermore,
$$\vec{k} = (k_x, k_y) = \left(|\vec{k}|\cos\theta, |\vec{k}|\sin\theta\right), \quad \vec{u} = (u_x, u_y) \tag{2.14}$$

In addition, the operator $d/dt$ denotes the total derivative along a spatial path of energy propagation, and is defined as

$$\frac{d}{dt} = \frac{\partial}{\partial t} + (\vec{c_g} + \vec{u})\cdot\nabla_{\vec{x}} \tag{2.15}$$

### 2.2.2 Spectral action balance equation

All information about the sea surface is contained in the wave variance spectrum or energy density $E(\sigma, \theta)$, distributing wave energy over (radian) frequencies $\sigma$ (as observed in a frame of reference moving with current velocity) and propagation directions $\theta$ (the direction normal to the wave crest of each spectral component). Usually, wave models determine the evolution of the action density $N(\vec{x}, t; \sigma, \theta)$ in space $\vec{x}$ and time $t$. The action density is

defined as $N = E/\sigma$ and is conserved during propagation along its wave characteristic in the presence of ambient current, whereas energy density $E$ is not (Whitman, 1974). Wave action is said to be adiabatic invariant. It is assumed that the ambient current is uniform with respect to the vertical co-ordinate and is denoted as $\vec{U}$.

The rate of change of the action density $N$ at a single point in space $(\vec{x}; \sigma, \theta)$ is governed by the action balance equation, which reads (e.g., Mei, 1983; Komen *et al.*, 1994):

$$\frac{\partial N}{\partial t} + \nabla_{\vec{x}} \cdot [(\vec{c}_g + \vec{U})N] + \frac{\partial c_\sigma N}{\partial \sigma} + \frac{\partial c_\theta N}{\partial \theta} = \frac{S_{\text{tot}}}{\sigma} \qquad (2.16)$$

The left hand side is the kinematic part of this equation. The second term denotes the propagation of wave energy in two-dimensional geographical $\vec{x}$-space, including wave shoaling, with the group velocity $\vec{c}_g = \partial\sigma/\partial\vec{k}$ following from the dispersion relation $\sigma^2 = g|\vec{k}|\tanh(|\vec{k}|d)$ where $\vec{k}$ is the wave number vector and $d$ the water depth. The third term represents the effect of shifting of the radian frequency due to variations in depth and mean currents. The fourth term represents depth-induced and current-induced refraction. The quantities $c_\sigma$ and $c_\theta$ are the propagation velocities in spectral space $(\sigma, \theta)$. Notice that the second, third and fourth terms are divergence terms representing the amount of flux entering or leaving a point, and hence, they act as source (negative divergence, i.e. flux entering a point) or sink (positive divergence, i.e. flux leaving a point) terms. The right hand side contains $S_{\text{tot}}$, which is the non-conservative source/sink term that represents all physical processes which generate, dissipate, or redistribute wave energy at a point. They are defined for energy density $E(\sigma, \theta)$ (i.e. not wave action). Details are given in Section 2.3.

At deep water without ambient current, Equation (2.16) is reduced to

$$\frac{\partial E}{\partial t} + \nabla_{\vec{x}} \cdot (\vec{c}_g E) = S_{\text{tot}} \qquad (2.17)$$

which can be considered as a ray equation for a wave packet propagating along its wave ray. In the absence of the generation and dissipation of waves, wave energy is conserved along its propagation path, which implies that the net flux of wave energy along this path is conserved (i.e. the divergence of this flux is zero). This is known as *the law of constant energy flux along the wave ray* (Burnside, 1915; Whitham, 1974, pg. 245). This law is essentially the bedrock on which the discretization of the action balance equation has been built. This will be discussed in Section 3.2.1.

It must be noted that the second term in the left hand side of Eq. (2.17) should not be interpreted as the transport of $E$ (being a transported quantity) with a transport velocity $\vec{c}_g$. The underlying reason is that the group velocity is generally not divergence free. Instead, we rewrite Eq. (2.17) as follows

$$\frac{\partial E}{\partial t} + \vec{c}_g \cdot \nabla_{\vec{x}} E + E \nabla_{\vec{x}} \cdot \vec{c}_g = S_{\text{tot}}$$

The second term in the left hand side represents the actual transport of $E$ along the wave ray with velocity $\vec{c}_g$ and the third term can be considered as a source or sink term with respect to energy density $E$; this density can be created (shoaling) or destroyed (de-shoaling) along the wave ray. This is due to the change in the group velocity along this ray. The correct interpretation of the second term of Eq. (2.17) is the divergence of the energy flux $\vec{c}_g E$, i.e. the net energy flux per unit square (it measures the flux source or sink at a point). The space discretization, as will be described in Section 3.2.1, is based on this interpretation.

Equation (2.16) can be recast in Cartesian or spherical co-ordinates. For small scale applications the spectral action balance equation may be expressed in Cartesian co-ordinates as given by

$$\frac{\partial N}{\partial t} + \frac{\partial c_x N}{\partial x} + \frac{\partial c_y N}{\partial y} + \frac{\partial c_\sigma N}{\partial \sigma} + \frac{\partial c_\theta N}{\partial \theta} = \frac{S_{\text{tot}}}{\sigma} \tag{2.18}$$

With respect to applications at shelf sea or oceanic scales the action balance equation may be recast in spherical co-ordinates as follows:

$$\frac{\partial \tilde{N}}{\partial t} + \frac{\partial c_\lambda \tilde{N}}{\partial \lambda} + \frac{\partial c_\varphi \tilde{N}}{\partial \varphi} + \frac{\partial c_\sigma \tilde{N}}{\partial \sigma} + \frac{\partial \tilde{c}_\theta \tilde{N}}{\partial \theta} = \frac{S_{\text{tot}}}{\sigma} \tag{2.19}$$

with action density $\tilde{N}$ with respect to longitude $\lambda$ and latitude $\varphi$. Note that $\theta$ is the wave direction taken counterclockwise from geographic East. The propagation velocities are reformulated as follows. On a sphere, we have

$$dx = R \cos \varphi d\lambda \tag{2.20}$$
$$dy = R d\varphi$$

with $R$ the radius of the earth. The propagation velocities in geographic space are then given by

$$\frac{d\lambda}{dt} = c_\lambda = \frac{1}{R \cos \varphi} \left[ \frac{1}{2} \left( 1 + \frac{2|\vec{k}|d}{\sinh(2|\vec{k}|d)} \right) \frac{\sigma |\vec{k}| \cos \theta}{|\vec{k}|^2} + u_\lambda \right] \tag{2.21}$$

$$\frac{d\varphi}{dt} = c_\varphi = \frac{1}{R} \left[ \frac{1}{2} \left( 1 + \frac{2|\vec{k}|d}{\sinh(2|\vec{k}|d)} \right) \frac{\sigma |\vec{k}| \sin \theta}{|\vec{k}|^2} + u_\varphi \right]$$

with $u_\lambda$ and $u_\varphi$ the ambient currents in longitude and latitude direction, respectively. The propagation velocity in $\sigma-$space remain unchanged. To rewrite the propagation velocity $\tilde{c}_\theta$ in terms of spherical co-ordinates, we use the so-called Clairaut's equation that states that on any geodesic, the following expression holds:

$$R \cos \varphi \cos \theta = \text{constant} \tag{2.22}$$

Differentiation of Eq. (2.22) with respect to a space co-ordinate $s$ in wave direction gives

$$-R \sin \varphi \cos \theta \frac{d\varphi}{ds} - R \cos \varphi \sin \theta \frac{d\theta}{ds} = 0 \tag{2.23}$$

Since, $dy = ds \sin\theta$, we have $d\varphi/ds = \sin\theta/R$. Substitution into Eq. (2.23) and using $ds = (c_x \cos\theta + c_y \sin\theta)dt$ yields

$$\frac{d\theta}{dt} = -\frac{c_x \cos\theta + c_y \sin\theta}{R} \cos\theta \tan\varphi \qquad (2.24)$$

This term (2.24) accounts for the change of propagation direction relative to true North when travelling along a great circle. This holds for deep water and without currents. Hence,

$$\tilde{c}_\theta = c_\theta - \frac{c_x \cos\theta + c_y \sin\theta}{R} \cos\theta \tan\varphi \qquad (2.25)$$

In Eq. (2.19), $\tilde{N}$ is related to the action density $N$ in a local Cartesian frame $(x, y)$ through $\tilde{N}d\sigma d\theta d\varphi d\lambda = Nd\sigma d\theta dxdy$, or $\tilde{N} = NR^2 \cos\varphi$. Substitution into (2.19) yields:

$$\frac{\partial N}{\partial t} + \frac{\partial c_\lambda N}{\partial \lambda} + \cos^{-1}\varphi \frac{\partial c_\varphi \cos\varphi N}{\partial \varphi} + \frac{\partial c_\sigma N}{\partial \sigma} + \frac{\partial \tilde{c}_\theta N}{\partial \theta} = \frac{S_{\text{tot}}}{\sigma} \qquad (2.26)$$

## 2.3 Sources and sinks

First, in Section 2.3.1 general concepts of the physical processes of generation, dissipation and nonlinear wave-wave interactions that are implemented in SWAN are outlined. Next, complete expressions for these physical processes are given in subsequent sections. Finally, for completeness, the first- and second-generation formulations as employed in SWAN are outlined in Section 2.3.5.

### 2.3.1 General concepts

In shallow water, six processes contribute to $S_{\text{tot}}$:

$$S_{\text{tot}} = S_{\text{in}} + S_{\text{nl3}} + S_{\text{nl4}} + S_{\text{ds,w}} + S_{\text{ds,b}} + S_{\text{ds,br}} . \qquad (2.27)$$

These terms denote, respectively, wave growth by the wind, nonlinear transfer of wave energy through three-wave and four-wave interactions and wave decay due to whitecapping, bottom friction and depth-induced wave breaking. First, a brief summary of the formulations is given below. Next, for each term complete expressions are outlined.

Wind input

Transfer of wind energy to the waves is described with a resonance mechanism (Phillips, 1957) and a feed-back mechanism (Miles, 1957).

Resonance with wind-induced pressure fluctations

The pressure distribution induced by wind at the sea surface is random. It propagates more or less a frozen pattern over the surface with wind speed. This can be Fourier transformed

to produce harmonic pressure waves that propagate with wind speed. If this harmonic pressure wave remains in phase with a free harmonic surface wave, then the wind energy is transferred from the pressure wave to the surface wave. The energy input by this mechanism, which contributes to the initial stages of wave growth, varies linearly with time.

Feedback of wave-induced pressure fluctations

When a wave has been generated by the resonance mechanism as explained above, it will distort the wind profile just above the water surface. This distortion results in an 'over pressure' on the wind ward side of the crest of the wave and an 'under pressure' at the lee side of the crest. It means that when the sea surface moves up and down, the pressure also follows the same movements, therefore transfer energy to the wave. This energy transfer is proportional to the energy in the wave itself, so the wave grows more as it gets larger. This effect is found to be exponential in time.

Based on the two wave growth mechanisms, wave growth due to wind commonly described as the sum of linear and exponential growth term of a wave component:

$$S_{\mathrm{in}}(\sigma, \theta) = A + BE(\sigma, \theta) \tag{2.28}$$

in which $A$ and $B$ depend on wave frequency and direction, and wind speed and direction. The effects of currents are accounted for by using the apparent local wind speed and direction. The expression for the term $A$ is due to Cavaleri and Malanotte-Rizzoli (1981) with a filter to avoid growth at frequencies lower than the Pierson-Moskowitz frequency (Tolman, 1992a). Two optional expressions for the coefficient $B$ are used in the SWAN model. The first is taken from an early version of the WAM Cycle 3 model (the WAMDI group, 1988). It is due to Snyder *et al.* (1981), rescaled in terms of friction velocity $U_*$ by Komen *et al.* (1984). The drag coefficient to relate $U_*$ to the driving wind speed at 10 m elevation $U_{10}$ is taken from either Wu (1982) or Zijlema *et al.* (2012). The second expression for $B$ in SWAN is taken from the WAM Cycle 4 model (Komen *et al.*, 1994). It is due to Janssen (1991a) and it accounts explicitly for the interaction between the wind and the waves by considering atmospheric boundary layer effects and the roughness length of the sea surface. The corresponding set of equations is solved (as in the WAM model) with the iterative procedure of Mastenbroek *et al.* (1993).

Dissipation

The dissipation term of wave energy is represented by the summation of three different contributions: whitecapping $S_{\mathrm{ds,w}}$, bottom friction $S_{\mathrm{ds,b}}$ and depth-induced breaking $S_{\mathrm{ds,br}}$.

Whitecapping is primarily controlled by the steepness of the waves. In presently operating third-generation wave models, the whitecapping formulations are based on a pulse-based model (Hasselmann, 1974), as adapted by the WAMDI group (1988):

$$S_{\mathrm{ds,w}}(\sigma, \theta) = -\Gamma \tilde{\sigma} \frac{k}{\tilde{k}} E(\sigma, \theta) \tag{2.29}$$

where $\Gamma$ is a steepness dependent coefficient, $k$ is wave number and $\tilde{\sigma}$ and $\tilde{k}$ denote a mean frequency and a mean wave number, respectively (cf. the WAMDI group, 1988). Komen *et al.* (1984) estimated the value of $\Gamma$ by closing the energy balance of the waves in fully developed conditions. This implies that this value depends on the wind input formulation that is used. Since two expressions are used for the wind input in SWAN, also two values for $\Gamma$ are used. The first is due to Komen *et al.* (1984), as in WAM Cycle 3. The second expression is an adaptation of this expression based on Janssen (1991a), as in WAM Cycle 4 (see Janssen, 1991b; Günther *et al.*, 1992). Young and Banner (1992) and Banner and Young (1994) have shown that the results of closing the energy balance in this manner depend critically on the choice of a high-frequency cut-off frequency above which a diagnostic spectral tail is used. In SWAN, this cut-off frequency is different from the one used in the WAM model. Differences in the growth rates between the WAM model and SWAN are therefore to be expected.

A number of alternative whitecapping expressions have been proposed to improve the accuracy of SWAN. These range from alternative calibrations of the Komen *et al* (1984) expression, e.g. Rogers *et al* (2003), to alternative ways of calculating mean spectral steepness, e.g. Van Vledder and Hurdle (2002). In SWAN, another alternative is presented.

This alternative is proposed by Van der Westhuysen *et al* (2007) and Van der Westhuysen (2007), based on the whitecapping expression of Alves and Banner (2003). This expression is based on experimental findings that whitecapping dissipation appears to be related to the nonlinear hydrodynamics within wave groups. This yields a dissipation term that primarily depends on quantities that are local in the frequency spectrum, as opposed to ones that are distributed over the spectrum, as in the expression of Komen *et al* (1984). However, the final whitecapping expression proposed by Alves and Banner (2003) features additional dependencies on the spectral mean wavenumber and steepness, which is problematic in situations of mixed sea and swell often encountered in the nearshore. Therefore, their whitecapping expression is applied in Van der Westhuysen (2007) without these mean spectral dependencies. This adapted whitecapping expression is used together with a wind input term that is based on that of Yan (1987).

In shallow water the orbital motions of the water particles, induced by surface waves, extend down to the sea floor. This gives rise to an interaction between te surface waves and the bottom. An overview of different wave-bottom interaction mechanisms and of their relative strengths is given by Shemdin *et al.* (1978). They are: scattering on bottom irregularities, motion of a soft bottom, percolation into a porous bottom and friction in the turbulent bottom boundary layer. The first process results in a local redistribution of wave energy by scattering of wave components. The last three are dissipative. Their strength depends on the bottom conditions. For continental shelf seas with sandy bottoms, the dominant mechanism appears to be bottom friction (Bertotti and Cavaleri, 1994) which

can generally be expressed as:

$$S_{\text{ds,b}} = -C_{\text{b}} \frac{\sigma^2}{g^2 \sinh^2 kd} E(\sigma, \theta) \tag{2.30}$$

in which $C_{\text{b}}$ is a bottom friction coefficient. A large number of models has been proposed since the pioneering paper of Putnam and Johnson (1949). Hasselmann *et al.* (1973) suggested to use an empirically obtained constant. It seems to perform well in many different conditions as long as a suitable value is chosen (typically different for swell and wind sea). A nonlinear formulation based on drag has been proposed by Hasselmann and Collins (1968) which was later simplified by Collins (1972). More complicated, eddy viscosity models have been developed by Madsen *et al.* (1988) and by Weber (1989, 1991a, 1991b). Considering the large variations in bottom conditions in coastal areas (bottom material, bottom roughness length, ripple height, etc.), there is no field data evidence to give preference to a particular friction model (Luo and Monbaliu, 1994). For this reason, the simplest of each of these types of friction models has been implemented in SWAN: the empirical JONSWAP model of Hasselmann *et al.* (1973), the drag law model of Collins (1972) and the eddy-viscosity model of Madsen *et al.* (1988). The effect of a mean current on the wave energy dissipation due to bottom friction is not taken into account in SWAN. The reasons for this are given by Tolman (1992b) who argues that state-of-the-art expressions vary too widely in their effects to be acceptable. He found that the error in finding a correct estimate of the bottom roughness length scale has a much larger impact on the energy dissipation rate than the effect of a mean current.

When waves propagate towards shore, shoaling leads to an increase in wave height. When the ratio of wave height over water depth exceeds a certain limit, waves start to break, thereby dissipating energy rapidly. In extreme shallow water (surf zone), this process becomes dominant over all other processes. The process of depth-induced wave breaking is still poorly understood and little is known about its spectral modelling. In contrast to this, the total dissipation (i.e. integrated over the spectral space) due to this type of wave breaking can be well modelled with the dissipation of a bore applied to the breaking waves in a random field (Battjes and Janssen, 1978; Thornton and Guza, 1983). Laboratory observations (e.g., Battjes and Beji, 1992; Vincent *et al.* 1994; Arcilla *et al.*, 1994 and Eldeberky and Battjes, 1996) show that the shape of initially uni-modal spectra propagating across simple (barred) beach profiles, is fairly insensitive to depth-induced breaking. This has led Eldeberky and Battjes (1995) to formulate a spectral version of the bore model of Battjes and Janssen (1978) that conserves the spectral shape. Expanding their expression to include directions, the expression reads:

$$S_{\text{ds,br}}(\sigma, \theta) = \frac{D_{\text{tot}}}{E_{\text{tot}}} E(\sigma, \theta) \tag{2.31}$$

in which $E_{\text{tot}}$ is the total wave energy and $D_{\text{tot}} < 0$ is the rate of dissipation of the total energy due to wave breaking according to Battjes and Janssen (1978). The value of $D_{\text{tot}}$ depends critically on the breaker parameter $\gamma = H_{\text{max}}/d$ (in which $H_{\text{max}}$ is the maximum

possible individual wave height in the local water depth $d$). In SWAN, both a constant value and a variable value are available. Examples of a variable breaker parameter can be found in Nelson (1987) and Ruessink et al. (2003). (Both are implemented in SWAN.) The constant value is $\gamma = 0.73$ found as the mean value of the data set of Battjes and Stive (1985).

<u>Nonlinear wave-wave interactions</u>

The basic properties of wave-wave interactions were discovered during the fundamental research of Phillips (1960) and Hasselmann (1960, 1962, 1963a,b). The physical meaning of the interactions is that resonant sets of wave components exchange energy, redistributing energy over the spectrum. In deep and intermediate water, four-wave interactions (so-called quadruplets) are important, whereas in shallow water three-wave interactions (so-called triads) become important.

In deep water, quadruplet wave-wave interactions dominate the evolution of the spectrum. They transfer wave energy from the spectral peak to lower frequencies (thus moving the peak frequency to lower values) and to higher frequencies (where the energy is dissipated by whitecapping). In very shallow water, triad wave-wave interactions transfer energy from lower frequencies to higher frequencies often resulting in higher harmonics (Beji and Battjes, 1993). Low-frequency energy generation by triad wave-wave interactions is not considered here.

A full computation of the quadruplet wave-wave interactions is extremely time consuming and not convenient in an operational wave model. Nevertheless, SWAN has an option to compute the Boltzmann integral in an exact manner. The approach is the exact method developed by Webb, Tracy and Resio (WRT) (Resio *et al.*, 2001). This algorithm was reprogrammed by Van Vledder, bearing the name XNL (Van Vledder and Bottema, 2003). This method is also enable to capture the frequency shift and the spectral shape changes as water depth decreases.

A number of techniques, based on parametric methods and approximations have been proposed to improve computational speed of computing quadruplets (see Young and Van Vledder (1993) for a review). In SWAN, the computations are carried out with the Discrete Interaction Approximation (DIA) of Hasselmann *et al.* (1985). This DIA has been found to be quite successful in describing the essential features of a developing wave spectrum; see Komen *et al.* (1994). For uni-directional waves, this approximation is not valid. In fact, the quadruplet interaction coefficient for these waves is nearly zero. For finite-depth applications, Hasselmann and Hasselmann (1981) have shown that for a JONSWAP-type spectrum the quadruplet wave-wave interactions can be scaled with a simple expression. In some cases, the DIA technique may not be accurate enough. In Hashimoto *et al.* (2002), it was demonstrated that the accuracy of the DIA may be improved by increasing the number of quadruplet configurations. They proposed a Multiple DIA with up to 6 wave number configurations.

In very shallow water, triad wave interactions become important for steep waves. It transfers energy to higher frequencies, resulting in higher harmonics (Beji and Battjes, 1993). The energy transfer in this process can take place over relatively short distance and can dramatically change single peaked spectra into multiple peaked spectra, which has frequently been observed in the field (Arcilla *et al.*, 1994) and in a number of laboratory experiments with a bar-trough profile (Beji and Battjes, 1993) and a plane beach profile (Nwogu, 1994).

A first attempt to describe triad wave-wave interactions in terms of a spectral energy source term was made by Abreu *et al.* (1992). However, their expression is restricted to non-dispersive shallow water waves and is therefore not suitable in many practical applications of wind waves. The breakthrough in the development came with the work of Eldeberky and Battjes (1995) who transformed the amplitude part of the Boussinesq model of Madsen and Sørensen (1993) into an energy density formulation and who parameterized the biphase of the waves on the basis of laboratory observations (Battjes and Beji, 1992; Arcilla *et al.*, 1994). A discrete triad approximation (DTA) for co-linear waves was subsequently obtained by considering only the dominant self-self interactions. Their model has been verified with flume observations of long-crested, random waves breaking over a submerged bar (Beji and Battjes, 1993) and over a barred beach (Arcilla *et al.*, 1994). The model appeared to be fairly successful in describing the essential features of the energy transfer from the primary peak of the spectrum to the super harmonics. A slightly different version, the so-called Lumped Triad Approximation (LTA) was later derived by Eldeberky (1996). This LTA technique is employed in SWAN.

## 2.3.2   Input by wind ($S_{\mathrm{in}}$)

Wave growth by wind is described by:

$$S_{\mathrm{in}}(\sigma, \theta) = A + BE(\sigma, \theta) \tag{2.32}$$

in which $A$ describes linear growth and $BE$ exponential growth. It should be noted that the SWAN model is driven by the wind speed at 10m elevation $U_{10}$ whereas it uses the friction velocity $U_*$. For the WAM Cycle 3 formulation the transformation from $U_{10}$ to $U_*$ is obtained with

$$U_*^2 = C_D U_{10}^2 \tag{2.33}$$

in which $C_D$ is the drag coefficient from Wu (1982):

$$C_D(U_{10}) = \begin{cases} 1.2875 \times 10^{-3}, & \text{for } U_{10} < 7.5 m/s \\ (0.8 + 0.065 s/m \times U_{10}) \times 10^{-3}, & \text{for } U_{10} \geq 7.5 m/s \end{cases} \tag{2.34}$$

Recent observations indicate that this parameterization overestimate the drag coefficient at high wind speeds ($U_{10} > 20$ m/s, say). Based on many authoritative studies it appears that the drag coefficient increases almost linearly with wind speed up to approximately 20 m/s, then levels off and decreases again at about 35 m/s to rather low values at 60 m/s

wind speed. We fitted a 2nd order polynomial to the data obtained from these studies, and this fit is given by

$$C_D(U_{10}) = (0.55 + 2.97\tilde{U} - 1.49\tilde{U}^2) \times 10^{-3} \tag{2.35}$$

where $\tilde{U} = U_{10}/U_{\text{ref}}$, and the reference wind speed $U_{\text{ref}} = 31.5$ m/s is the speed at which the drag attains its maximum value in this expression. These drag values are lower than in the expression of Wu (1982) by $10\% - 30\%$ for high wind speeds ($15 \leq U_{10} \leq 30$ m/s) and over $30\%$ for hurricane wind speeds ($U_{10} > 30$ m/s). More details can be found in Zijlema *et al.* (2012). Since version 41.01, the SWAN model employs the drag formulation as given by Eq. (2.35).

For the WAM Cycle 4 formulations, the computation of $U_*$ is an integral part of the source term.

Linear growth by wind

For the linear growth term $A$, the expression due to Cavaleri and Malanotte-Rizzoli (1981) is used with a filter to eliminate wave growth at frequencies lower than the Pierson-Moskowitz frequency (Tolman, 1992a)[1]:

$$A = \frac{1.5 \times 10^{-3}}{2\pi g^2}(U_* \max[0, \cos(\theta - \theta_w)])^4 H \,, \quad H = \exp\left\{-(\frac{\sigma}{\sigma_{\text{PM}}^*})^{-4}\right\}, \quad \sigma_{\text{PM}}^* = \frac{0.13g}{28U_*}2\pi \tag{2.36}$$

in which $\theta_w$ is the wind direction, $H$ is the filter and $\sigma_{\text{PM}}^*$ is the peak frequency of the fully developed sea state according to Pierson and Moskowitz (1964) as reformulated in terms of friction velocity.

Exponential growth by wind

Two expressions for exponential growth by wind are optionally available in the SWAN model. The first expression is due to Komen *et al.* (1984). Their expression is a function of $U_*/c_{\text{ph}}$:

$$B = \max[0, 0.25\frac{\rho_a}{\rho_w}(28\frac{U_*}{c_{\text{ph}}}\cos(\theta - \theta_w) - 1)]\sigma \tag{2.37}$$

in which $c_{\text{ph}}$ is the phase speed and $\rho_a$ and $\rho_w$ are the density of air and water, respectively. This expression is also used in WAM Cycle 3 (the WAMDI group, 1988). The second expression is due to Janssen (1989,1991a). It is based on a quasi-linear wind-wave theory and is given by:

$$B = \beta\frac{\rho_a}{\rho_w}\left(\frac{U_*}{c_{\text{ph}}}\right)^2 \max[0, \cos(\theta - \theta_w)]^2\sigma \tag{2.38}$$

---

[1]In Eq. (10) of Tolman (1992a) the power of $10^{-5}$ should be $10^{-3}$; H. Tolman, personal communication, 1995.

where $\beta$ is the Miles constant. In the theory of Janssen (1991a), this constant is estimated from the non-dimensional critical height $\lambda$:

$$\begin{cases} \beta = \frac{1.2}{\kappa^2}\lambda\ln^4\lambda\,, & \lambda \leq 1 \\[2mm] \lambda = \frac{gz_e}{c_{\mathrm{ph}}^2}e^r\,, & r = \kappa c/|U_*\cos(\theta - \theta_w)| \end{cases} \tag{2.39}$$

where $\kappa = 0.41$ is the Von Karman constant and $z_e$ is the effective surface roughness. If the non-dimensional critical height $\lambda > 1$, the Miles constant $\beta$ is set equal 0. Janssen (1991a) assumes that the wind profile is given by:

$$U(z) = \frac{U_*}{\kappa}\ln[\frac{z + z_e - z_0}{z_e}] \tag{2.40}$$

in which $U(z)$ is the wind speed at height $z$ (10m in the SWAN model) above the mean water level, $z_0$ is the roughness length. The effective roughness length $z_e$ depends on the roughness length $z_0$ and the sea state through the wave-induced stress $\vec{\tau_w}$ and the total surface stress $\vec{\tau} = \rho_a|\vec{U_*}|\vec{U_*}$:

$$z_e = \frac{z_0}{\sqrt{1 - \frac{|\vec{\tau_w}|}{|\vec{\tau}|}}}\,, \quad z_0 = \hat{\alpha}\frac{U_*^2}{g} \tag{2.41}$$

The second of these two equations is a Charnock-like relation in which $\hat{\alpha}$ is a constant equal to 0.01. The wave stress $\vec{\tau_w}$ is given by:

$$\vec{\tau_w} = \rho_w\int_0^{2\pi}\int_0^\infty \sigma B E(\sigma,\theta)\frac{\vec{k}}{k}d\sigma d\theta \tag{2.42}$$

The value of $U_*$ can be determined for a given wind speed $U_{10}$ and a given wave spectrum $E(\sigma,\theta)$ from the above set of equations. In the SWAN model, the iterative procedure of Mastenbroek *et al.* (1993) is used. This set of expressions (2.38) through (2.42) is also used in WAM Cycle 4 (Komen *et al.*, 1994).

## 2.3.3  Dissipation of wave energy ($S_{\mathrm{ds}}$)

Whitecapping: Komen *et al* (1984) formulation

The processes of whitecapping in the SWAN model is represented by the pulse-based model of Hasselmann (1974). Reformulated in terms of wave number (rather than frequency) so as to be applicable in finite water depth (cf. the WAMDI group, 1988), this expression is:

$$S_{\mathrm{ds,w}}(\sigma,\theta) = -\Gamma\tilde{\sigma}\frac{k}{\tilde{k}}E(\sigma,\theta) \tag{2.43}$$

where $\tilde{\sigma}$ and $\tilde{k}$ denote the mean frequency and the mean wave number, respectively, and the coefficient $\Gamma$ depends on the overall wave steepness. This steepness dependent coefficient,

as given by the WAMDI group (1988), has been adapted by Günther *et al.* (1992) based on Janssen (1991a) (see also (Janssen, 1991b)):

$$\Gamma = \Gamma_{\mathrm{KJ}} = C_{\mathrm{ds}}((1-\delta) + \delta\frac{k}{\tilde{k}}) \left(\frac{\tilde{s}}{\tilde{s}_{\mathrm{PM}}}\right)^p \tag{2.44}$$

For $\delta = 0$ the expression of $\Gamma$ reduces to the expression as used by the WAMDI group (1988). The coefficients $C_{\mathrm{ds}}$, $\delta$ and $p$ are tunable coefficients, $\tilde{s}$ is the overall wave steepness, $\tilde{s}_{\mathrm{PM}}$ is the value of $\tilde{s}$ for the Pierson-Moskowitz spectrum (1964): $\tilde{s}_{PM} = \sqrt{3.02 \times 10^{-3}}$. The overall wave steepness $\tilde{s}$ is defined as:

$$\tilde{s} = \tilde{k}\sqrt{E_{\mathrm{tot}}} \tag{2.45}$$

The mean frequency $\tilde{\sigma}$, the mean wave number $\tilde{k}$ and the total wave energy $E_{\mathrm{tot}}$ are defined as (cf. the WAMDI group, 1988):

$$\tilde{\sigma} = \left(E_{\mathrm{tot}}^{-1} \int_0^{2\pi} \int_0^\infty \frac{1}{\sigma} E(\sigma, \theta) d\sigma d\theta\right)^{-1} \tag{2.46}$$

$$\tilde{k} = \left(E_{\mathrm{tot}}^{-1} \int_0^{2\pi} \int_0^\infty \frac{1}{\sqrt{k}} E(\sigma, \theta) d\sigma d\theta\right)^{-2} \tag{2.47}$$

$$E_{\mathrm{tot}} = \int_0^{2\pi} \int_0^\infty E(\sigma, \theta) d\sigma d\theta \tag{2.48}$$

The values of the tunable coefficients $C_{\mathrm{ds}}$ and $\delta$ and exponent $p$ in this model have been obtained by Komen *et al.* (1984) and Janssen (1992) by closing the energy balance of the waves in idealized wave growth conditions (both for growing and fully developed wind seas) for deep water. This implies that coefficients in the steepness dependent coefficient $\Gamma$ depend on the wind input formulation that is used. Since two different wind input formulations are used in the SWAN model, two sets of coefficients are used. For the wind input of Komen *et al.* (1984; corresponding to WAM Cycle 3; the WAMDI group, 1988): $C_{\mathrm{ds}} = 2.36 \times 10^{-5}$, $\delta = 0$ and $p = 4$. Janssen (1992) and also Günther *et al.* (1992) obtained (assuming $p = 4$) $C_{\mathrm{ds}} = 4.10 \times 10^{-5}$ and $\delta = 0.5$ (as used in the WAM Cycle 4; Komen *et al.*, 1994).

It is well-known that SWAN underestimates structurally the mean (or peak) wave periods by 10 to 20%. This has also been observed in the SWAN hindcasts as described by Rogers *et al.* (2003). Investigations of Rogers *et al.* (2003) showed that adjusting the parameter $\delta$ from 0 to 1 leads to an improved prediction of the wave energy at lower frequencies. Because of this, $\delta$ is set to 1 as default since version 40.91A. However, it should be mentioned that adapting $\delta$ without retuning $C_{\mathrm{ds}}$ may lead to exceedence of the theoretical limits on wave height proposed by Pierson and Moskowitz (1964).

Whitecapping: saturation-based model; and wind: Yan model

An alternative description for whitecapping in SWAN is given by Van der Westhuysen *et al*

(2007) and Van der Westhuysen (2007), which is an adapted form of the expression of Alves and Banner (2003). The latter is based on the apparent relationship between wave groups and whitecapping dissipation. This adaption is due to the fact that it can also be applied to mixed sea-swell conditions and in shallow water. This was done by removing the dependencies on mean spectral steepness and wavenumber in the original expression, and by applying source term scaling arguments for its calibration (see below). This led to the following expression for whitecapping dissipation

$$S_{\text{ds,break}}(\sigma, \theta) = -C'_{\text{ds}} \left( \frac{B(k)}{B_{\text{r}}} \right)^{p/2} (\tanh(kh))^{(2-p_0)/4} \sqrt{gk} E(\sigma, \theta) \qquad (2.49)$$

in which the density function $B(k)$ is the azimuthal-integrated spectral saturation, which is positively correlated with the probability of wave group-induced breaking. It is calculated from frequency space variables as follows

$$B(k) = \int_0^{2\pi} c_g k^3 E(\sigma, \theta) d\theta \qquad (2.50)$$

and $B_{\text{r}} = 1.75 \times 10^{-3}$ is a threshold saturation level. The proportionality coefficient is set to $C'_{\text{ds}} = 5.0 \times 10^{-5}$. When $B(k) > B_{\text{r}}$, waves break and the exponent $p$ is set equal to a calibration parameter $p_0$. For $B(k) \leq B_{\text{r}}$ there is no breaking, but some residual dissipation proved necessary. This is obtained by setting $p = 0$. A smooth transition between these two situations is achieved by (Alves and Banner, 2003);

$$p = \frac{p_0}{2} + \frac{p_0}{2} \tanh \left[ 10 \left( \sqrt{\frac{B(k)}{B_{\text{r}}}} - 1 \right) \right] \qquad (2.51)$$

In Van der Westhuysen (2007) the dissipation modes of breaking and non-breaking waves are separated, so that they are active over different parts of the spectrum:

$$S_{\text{ds,w}}(\sigma, \theta) = f_{\text{br}}(\sigma) S_{\text{ds,break}} + [1 - f_{\text{br}}(\sigma)] S_{\text{ds,non-break}} \quad , \qquad (2.52)$$

where $S_{\text{ds,break}}$ is the contribution by breaking waves (2.49), and $S_{\text{ds,non-break}}$ dissipation by means other than breaking (e.g. turbulence). The changeover between the two modes is made with a smooth transition function $f_{\text{br}}$ similar to (2.51):

$$f_{\text{br}}(\sigma) = \frac{1}{2} + \frac{1}{2} \tanh \left[ 10 \left( \sqrt{\frac{B(k)}{B_{\text{r}}}} - 1 \right) \right] \qquad (2.53)$$

Since relatively little is known about the dissipation mechanisms of the non-breaking low-frequency waves, their dissipation is not modelled in detail. Instead, the expression (2.43) is used for $S_{\text{ds,non-break}}$, to provide general background dissipation of non-breaking waves. For this component, the parameter settings of Komen *et al.* (1984) are applied.

The wind input expression used in saturation-based model is based on that by Yan (1987).

This expression embodies experimental findings that for strong wind forcing, $u_*/c > 0.1$ say, the wind-induced growth rate of waves depends quadratically on $u_*/c$ (e.g. Plant 1982), whereas for weaker forcing, $u_*/c < 0.1$ say, the growth rate depends linearly on $u_*/c$ (Snyder *et al*, 1981). Yan (1987) proposes an analytical fit through these two ranges of the form:

$$\beta_{\text{fit}} = D\left(\frac{u_*}{c}\right)^2 \cos(\theta - \alpha) + E\left(\frac{u_*}{c}\right)\cos(\theta - \alpha) + F\cos(\theta - \alpha) + H \tag{2.54}$$

where $D,E,F$ and $H$ are coefficients of the fit. Yan imposed two constraints:

$$\beta_{\text{fit}} \approx \beta_{\text{Snyder}} \quad \text{for} \quad \frac{U_5}{c} \approx 1 \ \left(\text{or} \ \frac{u_*}{c} \approx 0.036\right) \tag{2.55}$$

and

$$\lim_{u_*/c \to \infty} \beta_{\text{fit}} = \beta_{\text{Plant}} \tag{2.56}$$

in which $\beta_{\text{Snyder}}$ and $\beta_{\text{Plant}}$ are the growth rates proposed by Snyder *et al* (1981) and Plant (1982), respectively. Application of Eqs. (2.55) and (2.56) led us to parameter values of $D = 4.0 \times 10^{-2}, E = 5.52 \times 10^{-3}, F = 5.2 \times 10^{-5}$ and $H = -3.02 \times 10^{-4}$, which are somewhat different from those proposed by Yan (1987). We found that our parameter values produce better fetch-limited simulation results in the Pierson and Moskowitz (1964) fetch range thant the original values of Yan (1987).

Finally, the choice of the exponent $p_0$ in Eqs. (2.49) and (2.51) is made by requiring that the source terms of whitecapping (Eq. 2.49) and wind input (Eq. 2.54) have equal scaling in frequency, after Resio *et al* (2004). This leads to a value of $p_0 = 4$ for strong wind forcing ($u_*/c > 0.1$) and $p_0 = 2$ for weaker forcing ($u_*/c < 0.1$). A smooth transition between these two limits, centred around $u_*/c = 0.1$, is achieved by the expression

$$p_0(\sigma) = 3 + \tanh\left[w\left(\frac{u_*}{c} - 0.1\right)\right] \tag{2.57}$$

where $w$ is a scaling parameter for which a value of $w = 26$ is used in SWAN. In shallow water, under strong wind forcing ($p_0 = 4$), this scaling condition requires the additional dimensionless factor $\tanh(kh)^{-1/2}$ in Eq. (2.49), where $h$ is the water depth.

### Wind input, whitecapping, and non-breaking dissipation by ST6

The "ST6" source term package was implemented in an unofficial (NRL) version of SWAN starting in 2008 and initial development was documented in Rogers *et al.* (2012). (At the time, it was referred to as "Babanin et al. physics" rather than "ST6".) ST6 was implemented in the official version of WAVEWATCH III®(WW3) starting in 2010, and this implementation was documented in Zieger *et al.* (2015). Since 2010, developments in the two models have largely paralleled each other, insofar as most notable improvements are implemented in both models. As such, the documentation for WW3 (public release versions 4 or 5) is largely adequate documentation of significant changes to the source terms

in SWAN since the publication of Rogers *et al.* (2012), and do not need to be repeated here. We point out three notable exceptions to this.

The first notable difference relates to the `SSWELL ZIEGER` option in SWAN, for representation of non-breaking dissipation. The steepness-dependent coefficient for this term, introduced to WW3 in version 5, has not yet been implemented in SWAN. The non-breaking dissipation instead follows ST6 in WW3 version 4. These two methods are contrasted by Zieger *et al.* (2015) in their equations 23 and 28.

The second notable difference is that ST6 in SWAN permits the use of the non-breaking dissipation of Ardhuin *et al.* (2010), the `SSWELL ARDHUIN` option in SWAN. This option is not available in WW3/ST6, but is instead the non-breaking dissipation used in WW3/ST4.

The third notable difference is that the wind speed scaling which was $U = 28u_\star$, following Komen *et al.* (1984), has been replaced with $U = S_{ws}u_\star$, where $S_{ws}$ is a free parameter. Use of $S_{ws} > 28$ (we use $S_{ws} = 32$) yields significant improvements to the tail level, correcting overprediction mean square slope. This necessitates tuning of the $a_1$ and $a_2$ coefficients. Settings are suggested in the SWAN User Manual. At time of writing, this feature has not yet been ported to WW3.

Other less notable differences include: changes to linear wind input (Cavaleri and Malanotte-Rizzoli 1981) in SWAN/ST6, changes to calculation of viscous stress in SWAN/ST6, and dissipation by viscosity in the water, added to SWAN/ST6.

Bottom friction

The bottom friction models that have been selected for SWAN are the empirical model of JONSWAP (Hasselmann *et al.*, 1973), the drag law model of Collins (1972) and the eddy-viscosity model of Madsen *et al.* (1988). The formulations for these bottom friction models can all be expressed in the following form:

$$S_{\mathrm{ds,b}} = -C_{\mathrm{b}} \frac{\sigma^2}{g^2 \sinh^2 kd} E(\sigma, \theta) \tag{2.58}$$

in which $C_{\mathrm{b}}$ is a bottom friction coefficient that generally depends on the bottom orbital motion represented by $U_{\mathrm{rms}}$:

$$U_{\mathrm{rms}}^2 = \int_0^{2\pi} \int_0^\infty \frac{\sigma^2}{\sinh^2 kd} E(\sigma, \theta) d\sigma d\theta \tag{2.59}$$

Hasselmann *et al.* (1973) found $C_{\mathrm{b}} = C_{\mathrm{JON}} = 0.038\mathrm{m}^2\mathrm{s}^{-3}$ which is in agreement with the JONSWAP result for swell dissipation. However, Bouws and Komen (1983) suggest a value of $C_{\mathrm{JON}} = 0.067\mathrm{m}^2\mathrm{s}^{-3}$ for depth-limited wind-sea conditions in the North Sea. This value is derived from revisiting the energy balance equation employing an alternative deep water dissipation. Recently, in Zijlema *et al.* (2012) it was found that a unified value of $0.038\mathrm{m}^2\mathrm{s}^{-3}$ can be used if the second order polyomial fit for wind drag of Eq. (2.35) is

employed. So, in SWAN 41.01 this is default irrespective of swell and wind-sea conditions.

The expression of Collins (1972) is based on a conventional formulation for periodic waves with the appropriate parameters adapted to suit a random wave field. The dissipation rate is calculated with the conventional bottom friction formulation of Eq. (2.58) in which the bottom friction coefficient is $C_\mathrm{b} = C_f g U_\mathrm{rms}$ with $C_f = 0.015$ (Collins, 1972)[2].

Madsen *et al.* (1988) derived a formulation similar to that of Hasselmann and Collins (1968) but in their model the bottom friction factor is a function of the bottom roughness height and the actual wave conditions. Their bottom friction coefficient is given by:

$$C_\mathrm{b} = f_w \frac{g}{\sqrt{2}} U_\mathrm{rms} \tag{2.60}$$

in which $f_w$ is a non-dimensional friction factor estimated by using the formulation of Jonsson (1966) cf. Madsen *et al.* (1988):

$$\frac{1}{4\sqrt{f_w}} + \log_{10}(\frac{1}{4\sqrt{f_w}}) = m_f + \log_{10}(\frac{a_b}{K_\mathrm{N}}) \tag{2.61}$$

in which $m_f = -0.08$ (Jonsson and Carlsen, 1976) and $a_b$ is a representative near-bottom excursion amplitude:

$$a_b^2 = 2 \int_0^{2\pi} \int_0^\infty \frac{1}{\sinh^2 kd} E(\sigma, \theta) d\sigma d\theta \tag{2.62}$$

and $K_\mathrm{N}$ is the bottom roughness length scale. For values of $a_b/K_\mathrm{N}$ smaller than 1.57 the friction factor $f_w$ is 0.30 (Jonsson, 1980).

Depth-induced wave breaking

To model the energy dissipation in random waves due to depth-induced breaking, the bore-based model of Battjes and Janssen (1978) is used in SWAN. The mean rate of energy dissipation per unit horizontal area due to wave breaking $D_\mathrm{tot}$ is expressed as:

$$D_\mathrm{tot} = -\frac{1}{4} \alpha_\mathrm{BJ} Q_b (\frac{\tilde{\sigma}}{2\pi}) H_\mathrm{max}^2 = -\alpha_\mathrm{BJ} Q_b \tilde{\sigma} \frac{H_\mathrm{max}^2}{8\pi} \tag{2.63}$$

in which $\alpha_\mathrm{BJ} = 1$ in SWAN, $Q_b$ is the fraction of breaking waves determined by:

$$\frac{1 - Q_b}{\ln Q_b} = -8 \frac{E_\mathrm{tot}}{H_\mathrm{max}^2} \tag{2.64}$$

in which $H_\mathrm{max}$ is the maximum wave height that can exist at the given depth and $\tilde{\sigma}$ is a mean frequency defined as:

$$\tilde{\sigma} = E_\mathrm{tot}^{-1} \int_0^{2\pi} \int_0^\infty \sigma E(\sigma, \theta) d\sigma d\theta \tag{2.65}$$

---

[2]Collins (1972) contains an error in the expression due to an erroneous Jacobian transformation. See page A-16 of Tolman (1990).

The fraction of depth-induced breakers ($Q_b$) is determined in SWAN with

$$Q_b = \begin{cases} 0\,, & \text{for } \beta \leq 0.2 \\[2mm] Q_0 - \beta^2 \frac{Q_0 - \exp{(Q_0-1)}/\beta^2}{\beta^2 - \exp{(Q_0-1)}/\beta^2}\,, & \text{for } 0.2 < \beta < 1 \\[2mm] 1\,, & \text{for } \beta \geq 1 \end{cases} \qquad (2.66)$$

where $\beta = H_{\text{rms}}/H_{\text{max}}$. Furthermore, for $\beta \leq 0.5$, $Q_0 = 0$ and for $0.5 < \beta \leq 1$, $Q_0 = (2\beta - 1)^2$.

Extending the expression of Eldeberky and Battjes (1995) to include the spectral directions, the dissipation for a spectral component per unit time is calculated in SWAN with:

$$S_{\text{ds,br}}(\sigma, \theta) = \frac{D_{\text{tot}}}{E_{\text{tot}}} E(\sigma, \theta) = -\frac{\alpha_{\text{BJ}} Q_b \tilde{\sigma}}{\beta^2 \pi} E(\sigma, \theta) \qquad (2.67)$$

The maximum wave height $H_{\text{max}}$ is determined in SWAN with $H_{\text{max}} = \gamma d$, in which $\gamma$ is the breaker parameter and $d$ is the total water depth (including the wave-induced set-up if computed by SWAN). In the literature, this breaker parameter $\gamma$ is often a constant or it is expressed as a function of bottom slope or incident wave steepness (see e.g., Galvin, 1972; Battjes and Janssen, 1978; Battjes and Stive, 1985; Arcilla and Lemos, 1990; Kaminsky and Kraus, 1993; Nelson, 1987, 1994). In the publication of Battjes and Janssen (1978) in which the dissipation model is described, a constant breaker parameter, based on Miche's criterion, of $\gamma = 0.8$ was used. Battjes and Stive (1985) re-analyzed wave data of a number of laboratory and field experiments and found values for the breaker parameter varying between 0.6 and 0.83 for different types of bathymetry (plane, bar-trough and bar) with an average of 0.73. From a compilation of a large number of experiments Kaminsky and Kraus (1993) have found breaker parameters in the range of 0.6 to 1.59 with an average of 0.79.

An alternative to the bore-based model of Battjes and Janssen (1978) is proposed by Thornton and Guza (1983). This model can be regarded as an alteration of Battjes and Janssen with respect to the description of the wave height probability density function. The total dissipation due to depth-induced breaking is formulated as

$$D_{\text{tot}} = -\frac{B^3 \tilde{\sigma}}{8\pi d} \int_0^\infty H^3 p_b(H)\, dH \qquad (2.68)$$

in which $B$ is a proportionality coefficient and $p_b(H)$ is the probability density function of breaking waves times the fraction of breakers, $Q_b$. Based on field observations, the wave heights in the surf zone are assumed to remain Rayleigh distributed, even after breaking. This implies that all waves will break, not only the highest as assumed by Battjes and Janssen (1978). The function $p_b(H)$ is obtained by multiplying the Rayleigh wave height probability density function $p(H)$, given by

$$p(H) = \frac{2H}{H_{\text{rms}}^2} \exp\left(-\left(\frac{H}{H_{\text{rms}}}\right)^2\right) \qquad (2.69)$$

by a weighting function $W(H)$ defined so that $0 \le W(H) \le 1$, to yield

$$p_b(H) = W(H)\,p(H) \tag{2.70}$$

Thornton and Guza (1983) proposed the following weighting function in which the fraction of breaking waves is independent of the wave height:

$$W(H) = Q_b = \left(\frac{H_{\mathrm{rms}}}{\gamma d}\right)^n \tag{2.71}$$

with a calibration parameter $n(=4)$ and a breaker index $\gamma$ (not to be confused with the Battjes and Janssen breaker index!). The integral in expression (2.68) can then be simplified, as follows:

$$\int_0^\infty H^3\,p_b(H)\,dH = Q_b \int_0^\infty H^3\,p(H)\,dH = \frac{3}{4}\sqrt{\pi}\,Q_b\,H_{\mathrm{rms}}^3 \tag{2.72}$$

Hence,

$$D_{\mathrm{tot}} = -\frac{3B^3\tilde{\sigma}}{32\sqrt{\pi}d}\,Q_b\,H_{\mathrm{rms}}^3 \tag{2.73}$$

## 2.3.4 Nonlinear wave-wave interactions ($S_{\mathrm{nl}}$)

**Quadruplets**

In this section two methods are described for the computation of nonlinear interactions at deep water. The first method is called the DIA method and is relatively crude in the approximation of the Boltzmann integral. The second one is called the XNL approach and is implemented in SWAN by G. Ph. van Vledder.

DIA

The quadruplet wave-wave interactions are computed with the Discrete Interaction Approximation (DIA) as proposed by Hasselmann *et al.* (1985). Their source code (slightly adapted by Tolman, personal communication, 1993) has been implemented in the SWAN model. In the DIA two quadruplet wave number configurations are considered, both with frequencies:

$$\sigma_1 = \sigma_2 = \sigma\,, \sigma_3 = \sigma(1+\lambda) = \sigma^+\,, \sigma_4 = \sigma(1-\lambda) = \sigma^- \tag{2.74}$$

where $\lambda$ is a coefficient with a default value of 0.25. To satisfy the resonance conditions for the first quadruplet, the wave number vectors with frequency $\sigma_3$ and $\sigma_4$ lie at an angle of $\theta_3 = -11.48^o$ and $\theta_4 = 33.56^o$ to the angle of the wave number vectors with frequencies $\sigma_1$ and $\sigma_2$. The second quadruplet is the mirror image of the first quadruplet with relative angles of $\theta_3 = \theta^+ = 11.48^o$ and $\theta_4 = \theta^- = -33.56^o$. An example of this wave number configuration is shown in Figure 2.2. See Van Vledder et al. (2000) for further information about wave number configurations for arbitrary values of $\lambda$.
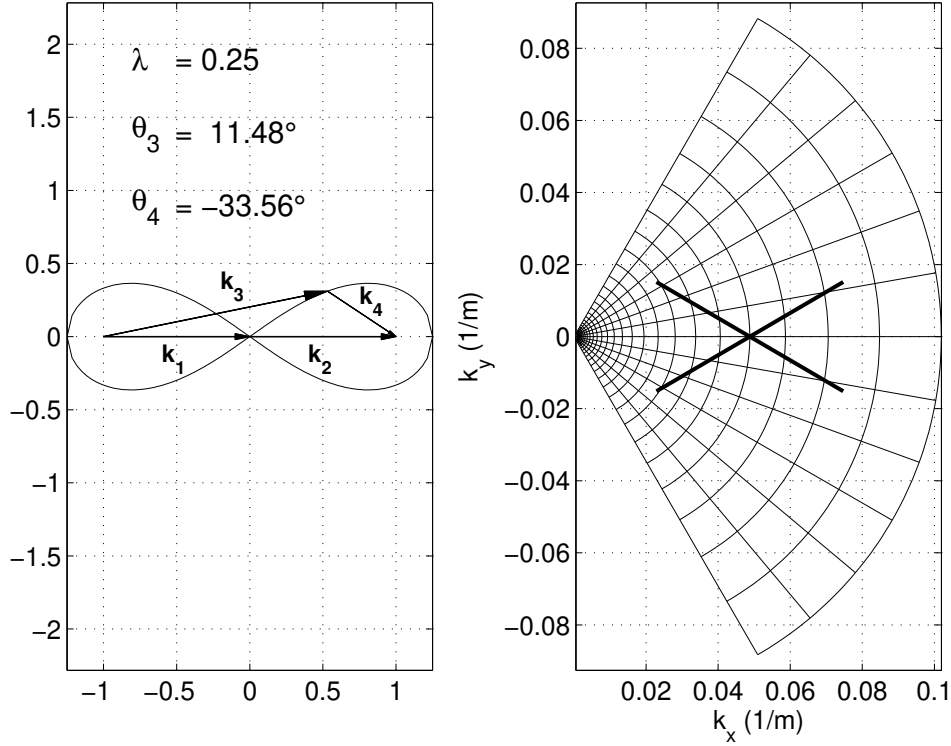
Figure 2.2: Wave number configuration for $\lambda=0.25$ and its position in a discrete frequency-direction spectrum (from Van Vledder et al., 2000).

Within this discrete interaction approximation, the source term $S_{\mathrm{nl4}}(\sigma,\theta)$ for the nonlinear transfer rate is given by:

$$S_{\mathrm{nl4}}(\sigma,\theta) = S_{\mathrm{nl4}}^*(\sigma,\theta) + S_{\mathrm{nl4}}^{**}(\sigma,\theta) \tag{2.75}$$

where $S_{\mathrm{nl4}}^*$ refers to the first quadruplet and $S_{\mathrm{nl4}}^{**}$ to the second quadruplet (the expressions for $S_{\mathrm{nl4}}^{**}$ are identical to those for $S_{\mathrm{nl4}}^*$ for the mirror directions). The DIA exchanges wave variance at all three wave number vectors involved in a quadruplet wave number configuration. The rate of change of wave variance due to the quadruplet interaction at the three frequency-direction bins can be written as:

$$
\begin{pmatrix}
\delta S_{\mathrm{nl4}}^*(\sigma,\theta) \\
\delta S_{\mathrm{nl4}}^*(\sigma^+,\theta^+) \\
\delta S_{\mathrm{nl4}}^*(\sigma^-,\theta^-)
\end{pmatrix}
=
\begin{pmatrix}
2 \\
-1 \\
-1
\end{pmatrix}
C_{\mathrm{nl4}}(2\pi)^2 g^{-4}\left(\frac{\sigma}{2\pi}\right)^{11} \times
$$

$$
\left[ E^2(\sigma,\theta)\left\{\frac{E(\sigma^+,\theta^+)}{(1+\lambda)^4} + \frac{E(\sigma^-,\theta^-)}{(1-\lambda)^4}\right\} \right.
$$

$$
\left. -2\frac{E(\sigma,\theta)E(\sigma^+,\theta^+)E(\sigma^-,\theta^-)}{(1-\lambda^2)^4} \right] \tag{2.76}
$$

where $C_{nl4} = 3\times10^7$ by default. Eq. (2.76) conserves wave variance, momentum and action when the frequencies are geometrically distributed (as is the case in the SWAN model).

The wave variance density at the frequency-direction bins $E(\sigma^+, \theta^+)$ and $E(\sigma^-, \theta^-)$ is obtained by bi-linear interpolation between the four surrounding frequency-direction bins. Similarly, the rate of change of variance density is distributed between the four surrounding bins using the same weights as used for the bi-linear interpolation.

In the DIA algorithm, Eq. (2.76) (and its mirror image) is applied to all spectral bins in a discrete frequency-direction spectrum. Figure 2.2 shows an example of one wave number configuration and its mirror image in a discrete spectrum. An extended spectral grid is applied to compute the interactions in the frequency range affected by the parametric spectral tail.

SWAN has an option to replace bi-linear interpolation of wave variance density using the nearest bin approach using a weight equal to 1.

Following the WAM group (WAMDI, 1988), the quadruplet interaction in shallow water with depth $d$ is obtained by multiplying the deep water nonlinear transfer rate with a scaling factor $R(k_p d)$:

$$S_{\text{nl4}}^{\text{finite depth}} = R(k_p d) S_{\text{nl4}}^{\text{deep water}} \tag{2.77}$$

where $R$ is given by:

$$R(k_p d) = 1 + \frac{C_{sh1}}{k_p d}(1 - C_{sh2} k_p d) e^{C_{sh3} k_p d} \tag{2.78}$$

in which $k_p$ is the peak wave number of the frequency spectrum. WAMDI (1988) proposes the following values of the coefficients: $C_{sh1} = 5.5$, $C_{sh2} = 5/6$ and $C_{sh3} = -5/4$. In the shallow water limit, i.e., $k_p \to 0$ the nonlinear transfer rate tends to infinity. Therefore, a lower limit of $k_p = 0.5$ is applied, resulting in a maximum value of $R(k_p d) = 4.43$. To increase the model robustness in case of arbitrarily shaped spectra, the peak wave number $k_p$ is replaced by $k_p = 0.75\tilde{k}$ (cf. Komen *et al.*, 1994).

<u>XNL</u> (G. Ph. van Vledder)

The second method for calculating the nonlinear interactions in SWAN is the so-called Webb-Resio-Tracy method (WRT), which is based on the original six-dimensional Boltzmann integral formulation of Hasselmann (1962, 1963a,b), and additional considerations by Webb (1978), Tracy and Resio (1982) and Resio and Perrie (1991). A detailed description of the WRT method and its implementation in discrete spectral wave models like SWAN is given in Van Vledder (2006). An overview of computational methods for computing the exact nonlinear transfer rate is given in Benoit (2005).

The Boltzmann integral describes the rate of change of action density of a particular wave number due to resonant interactions between pairs of four wave numbers. To interact these wave numbers must satisfy the following resonance conditions

$$\left.\begin{array}{rcl} \vec{k}_1 + \vec{k}_2 & = & \vec{k}_3 + \vec{k}_4 \\ \sigma_1 + \sigma_2 & = & \sigma_3 + \sigma_4 \end{array}\right\} \ . \tag{2.79}$$

The rate of change of action density $N_1$ at wave number $\vec{k}_1$ due to all quadruplet interactions involving $\vec{k}_1$ is given by

$$\frac{\partial N_1}{\partial t} = \iiint G\left(\vec{k}_1, \vec{k}_2, \vec{k}_3, \vec{k}_4\right) \delta\left(\vec{k}_1 + \vec{k}_2 - \vec{k}_3 - \vec{k}_4\right) \delta\left(\sigma_1 + \sigma_2 - \sigma_3 - \sigma_4\right)$$
$$\times \ \left[N_1 N_3\left(N_4 - N_2\right) + N_2 N_4\left(N_3 - N_1\right)\right] d\vec{k}_2 \, d\vec{k}_3 \, d\vec{k}_4 \ , \tag{2.80}$$

where the action density $N$ is defined in terms of the wave number vector $\vec{k}$, $N = N(\vec{k})$. The term $G$ is a complicated coupling coefficient for which an explicit expression has been given by Herterich and Hasselmann (1980). In the WRT method a number of transformations are made to remove the delta functions. A key element in the WRT method is to consider the integration space for each $(\vec{k}_1, \vec{k}_3)$ combination

$$\frac{\partial N_1}{\partial t} = 2 \int T\left(\vec{k}_1, \vec{k}_3\right) d\vec{k}_3 \ , \tag{2.81}$$

in which the function $T$ is given by

$$T\left(\vec{k}_1, \vec{k}_3\right) = \iint G\left(\vec{k}_1, \vec{k}_2, \vec{k}_3, \vec{k}_4\right) \delta\left(\vec{k}_1 + \vec{k}_2 - \vec{k}_3 - \vec{k}_4\right)$$
$$\times \ \delta\left(\sigma_1 + \sigma_2 - \sigma_3 - \sigma_4\right) \theta\left(\vec{k}_1, \vec{k}_3, \vec{k}_4\right)$$
$$\times \ \left[N_1 N_3\left(N_4 - N_2\right) + N_2 N_4\left(N_3 - N_1\right)\right] d\vec{k}_2 \, d\vec{k}_4 \ , \tag{2.82}$$

in which

$$\theta\left(\vec{k}_1, \vec{k}_3, \vec{k}_4\right) = \begin{cases} 1 & \text{when} \ \left|\vec{k}_1 - \vec{k}_3\right| \leq \left|\vec{k}_1 - \vec{k}_4\right| \\ 0 & \text{when} \ \left|\vec{k}_1 - \vec{k}_3\right| > \left|\vec{k}_1 - \vec{k}_4\right| \end{cases} \tag{2.83}$$

The delta functions in Eq. (2.82) determine a region in wave number space along which the integration should be carried out. The function $\theta$ determines a section of the integral which is not defined due to the assumption that $\vec{k}_1$ is closer to $\vec{k}_3$ than $\vec{k}_2$. The crux of the Webb method consists of using a local co-ordinate system along a so-named locus, that is, the path in $\vec{k}$ space that satisfies the resonance conditions for a given combination of $\vec{k}_1$ and $\vec{k}_3$. To that end the $(k_x, k_y)$ co-ordinate system is replaced by a $(s, n)$ co-ordinate system, where $s$ $(n)$ is the tangential (normal) direction along the locus. After some transformations the transfer integral can then be written as a closed line integral along the closed locus

$$T\left(\vec{k}_1, \vec{k}_3\right) = \oint G \, J \, \theta(\vec{k}_1, \vec{k}_3, \vec{k}_4)$$
$$\times \ \left[N_1 N_3\left(N_4 - N_2\right) + N_2 N_4\left(N_3 - N_1\right)\right] ds \ , \tag{2.84}$$

in which $G$ is the coupling coefficient and $J$ is the Jacobian term of a function representing the resonance conditions. The Jacobian term is a function of the group velocities of interacting wave numbers

$$J = |\vec{c}_{g,2} - \vec{c}_{g,4}|^{-1} \tag{2.85}$$

Numerically, the Boltzmann integral is computed as the finite sum of many line integrals $T$ for all discrete combinations of $\vec{k}_1$ and $\vec{k}_3$. The line integral (2.84) is solved by dividing the locus in typically 40 pieces, such that it's discretized version is given as:

$$T\left(\vec{k}_1, \vec{k}_3\right) \approx \sum_{i=1}^{n_s} G(s_i) J(s_i) P(s_i)\, \Delta s_i \quad, \tag{2.86}$$

in which $P(s_i)$ is the product term for a given point on the locus, $n_s$ is the number of segments, $s_i$ is the discrete co-ordinate along the locus, and $\Delta s_i$ is the stepsize. Finally, the rate of change for a given wave number $\vec{k}_1$ is given by

$$\frac{\partial N(\vec{k}_1)}{\partial t} \approx \sum_{i_{k3}=1}^{n_k} \sum_{i_{\theta3}=1}^{n_\theta} T(\vec{k}_1, \vec{k}_3)\, \Delta k_{i_{k3}}\, \Delta \theta_{i_{\theta3}} \tag{2.87}$$

where $n_k$ and $n_\theta$ are the discrete number of wave numbers and directions in the computational spectral grid, respectively. Note that although the spectrum is defined in terms of the vector wave number $\vec{k}$, the computational grid in a wave model is more conveniently defined in terms of the absolute wave number and wave direction $(k, \theta)$ to assure directional isotropy of the calculations. Taking all wave numbers $\vec{k}_1$ into account produces the complete source term due to nonlinear quadruplet wave-wave interactions. Details of the computation of a locus for a given combination of the wave numbers $\vec{k}_1$ and $\vec{k}_3$ can be found in Van Vledder (2006).

It is noted that these exact interaction calculations are extremely expensive, typically requiring $10^3$ to $10^4$ times more computational effort than the DIA. Presently, these calculations can therefore only be made for highly idealized test cases involving a limited spatial grid.

The nonlinear interactions according to the WRT method have been implemented in SWAN using portable subroutines. In this implementation, the computational grid of the WRT method is based to the discrete spectral grid of SWAN. The WRT method uses a $(\vec{k}, \theta)$ grid which is based on the $(\sigma, \theta)$ grid of SWAN. In addition, the WRT routines inherit the power of the parametric spectral tail as in the DIA. Choosing a higher resolution than the computational grid of SWAN for computing the nonlinear interactions is possible in theory, but this does not improve the results and is therefore not implemented.

Because nonlinear quadruplet wave-wave interactions at high frequencies are important, it is recommended to choose the maximum frequency of the wave model about six times the peak frequency of the spectra that are expected to occur in a wave model run. Note that this is important as the spectral grid determines the range of integration in Eq. (2.87). The recommended number of frequencies is about 40, with a frequency increment factor 1.07. The recommended directional resolution for computing the nonlinear interactions is about 10°. For specific purposes other resolutions may be used, and some testing with other resolutions may be needed.

An important feature of most algorithms for the evaluation of the Boltzmann integral is that the integration space can be pre-computed. In the initialization phase of the wave model the integration space, consisting of the discretized paths of all loci, together with the interaction coefficients and Jacobians, are computed and stored in a binary data file. For each discrete water depth such a data file is generated and stored in the work directory. The names of these data files consist of a keyword, "xnl4v5", followed by the keyword "*xxxxx*", with *xxxxx* the water depth in a certain unit (meters by default), or *99999* for deep water. The extension of the binary data file is "bqf" (of Binary Quadruplet File). If a BQF file exists, the program checks if this BQF file has been generated with the proper spectral grid. If this is not the case, a new BQF file is generated and the existing BQF file is overwritten. During a wave model run with various depths, the optimal BQF is used, by looking at the 'nearest' water depth $d_N$ for which a valid BQF file has been generated. In addition, the result is rescaled using the DIA scaling (2.78) according to

$$S_{\text{nl4}}^d = S_{\text{nl4}}^{d_N} \frac{R(k_p d)}{R(k_p d_N)} \quad . \tag{2.88}$$

**Triads**

The Lumped Triad Approximation (LTA) of Eldeberky (1996), which is a slightly adapted version of the Discrete Triad Approximation (DTA) of Eldeberky and Battjes (1995) is used in SWAN in each spectral direction:

$$S_{\text{nl3}}(\sigma, \theta) = S_{\text{nl3}}^-(\sigma, \theta) + S_{\text{nl3}}^+(\sigma, \theta) \tag{2.89}$$

with

$$S_{\text{nl3}}^+(\sigma, \theta) = \max[0, \alpha_{\text{EB}} 2\pi cc_g J^2 |\sin\beta| \left\{ E^2(\sigma/2, \theta) - 2E(\sigma/2, \theta)E(\sigma, \theta) \right\}] \tag{2.90}$$

and

$$S_{\text{nl3}}^-(\sigma, \theta) = -2S_{\text{nl3}}^+(2\sigma, \theta) \tag{2.91}$$

in which $\alpha_{\text{EB}}$ is a tunable proportionality coefficient. The biphase $\beta$ is approximated with

$$\beta = -\frac{\pi}{2} + \frac{\pi}{2} \tanh(\frac{0.2}{Ur}) \tag{2.92}$$

with Ursell number $Ur$:

$$Ur = \frac{g}{8\sqrt{2}\pi^2} \frac{H_s T_{m01}^2}{d^2} \tag{2.93}$$

The triad wave-wave interactions are calculated only for $0 \leq Ur \leq 1$. The interaction coefficient $J$ is taken from Madsen and Sørensen (1993):

$$J = \frac{k_{\sigma/2}^2(gd + 2c_{\sigma/2}^2)}{k_\sigma d(gd + \frac{2}{15}gd^3 k_\sigma^2 - \frac{2}{5}\sigma^2 d^2)} \tag{2.94}$$

## 2.3.5 First- and second-generation model formulations in SWAN

The source term $S_{\text{tot}}$ for the first- and second-generation formulation (relaxation model) of SWAN is (Holthuijsen and de Boer, 1988):

$$
S_{\text{tot}} = \begin{cases}
S_{\text{in}} = A + BE\,, & \text{if } E < E_{\text{lim}} \quad \text{and } |\theta - \theta_w| < \frac{\pi}{2} \\[2mm]
S_{\text{ds,w}} = \frac{E_{\text{lim}} - E}{\tau}\,, & \text{if } E > E_{\text{lim}} \quad \text{and } |\theta - \theta_w| < \frac{\pi}{2} \\[2mm]
0\,, & \text{if } E > E_{\text{lim}} \quad \text{and } |\theta - \theta_w| > \frac{\pi}{2}
\end{cases}
\tag{2.95}
$$

where $S_{\text{in}}$ and $S_{\text{ds,w}}$ represent input by wind and decay for over-developed sea states, respectively, $A$ and $BE$ are a linear and exponential growth term, respectively, $E$ is the spectral density, $E_{\text{lim}}$ is the saturated spectrum, $\tau$ is a time scale and $\theta$ and $\theta_w$ are the discrete spectral wave direction and the wind direction, respectively. The expressions for the source terms $S_{\text{in}}$ and $S_{\text{ds,w}}$ have been modified for shallow water applications (N. Booij and L.H. Holthuijsen, personal communication, 1996) and are given below.

The distinction between first- and second-generation is only in the formulation of the saturated spectrum $E_{\text{lim}}$ as outlined below.

Linear and exponential growth

The linear growth term $A$ is given by an expression due to Cavaleri and Malanotte-Rizolli (1981) as adapted by Holthuijsen and de Boer (1988) and Holthuijsen et al. (1996):

$$
A = \begin{cases}
\frac{\beta_1}{2\pi} \frac{\pi}{g^2} C_{\text{drag}}^2 \left(\frac{\rho_a}{\rho_w}\right)^2 (U_{10} \max[0, \cos(\theta - \theta_w)])^4\,, & \sigma \geq 0.7\sigma_{\text{PM,d}} \\[2mm]
0\,, & \sigma < 0.7\sigma_{\text{PM,d}}
\end{cases}
\tag{2.96}
$$

where $\beta_1$ is a coefficient that has been tuned to be $\beta_1 = 188$, $C_{\text{drag}}$ is a drag coefficient equal to $C_{\text{drag}} = 0.0012$ and $\sigma_{\text{PM,d}}$ is the fully developed peak frequency including the effect of shallow water and is estimated from the depth dependent relation of the Shore Protection Manual (1973):

$$
\sigma_{\text{PM,d}} = \frac{\sigma_{\text{PM}}}{\tanh(0.833\tilde{d}^{0.375})}
\tag{2.97}
$$

with the dimensionless depth

$$
\tilde{d} = \frac{gd}{U_{10}^2}
\tag{2.98}
$$

The Pierson-Moskowitz (1964) frequency is

$$
\sigma_{\text{PM}} = \frac{0.13g}{U_{10}} 2\pi
\tag{2.99}
$$

The exponential growth term $BE$ is due to Snyder et al. (1981) rescaled in terms of $U_{10}$ as adapted by Holthuijsen and de Boer (1988) and Holthuijsen et al. (1996):

$$B = \max[0, \beta_2 \frac{5}{2\pi} \frac{\rho_a}{\rho_w} (\frac{U_{10}}{\sigma/k} \cos(\theta - \theta_w) - \beta_3)]\sigma \qquad (2.100)$$

in which the coefficients $\beta_2$ and $\beta_3$ have been tuned to be $\beta_2 = 0.59$ and $\beta_3 = 0.12$.

Decay

If the spectral densities are larger than the wind-dependent saturation spectrum $E_{\lim}$, (e.g., when the wind decreases), energy is dissipated with a relaxation model:

$$S_{ds,w}(\sigma, \theta) = \frac{E_{\lim}(\sigma, \theta) - E(\sigma, \theta)}{\tau(\sigma)} \qquad (2.101)$$

where $\tau(\sigma)$ is a time scale given by

$$\tau(\sigma) = \beta_4 \left(\frac{2\pi}{\sigma}\right)^2 \frac{g}{U_{10} \cos(\theta - \theta_w)} \qquad (2.102)$$

in which the coefficient $\beta_4$ has been tuned to be $\beta_4 = 250$.

Saturated spectrum

The saturated spectrum has been formulated in term of wave number with a $\cos^2$−directional distribution centred at the local wind direction $\theta_w$. It is essentially an adapted Pierson-Moskowitz (1964) spectrum:

$$S_{tot} = \begin{cases} \frac{\alpha k^{-3}}{2c_g} \exp\left\{-\frac{5}{4}(\frac{\sigma}{\sigma_{PM,d}})^{-4}\right\} \frac{2}{\pi} \cos^2(\theta - \theta_w), & \text{for } |\theta - \theta_w| < \frac{\pi}{2} \\ 0, & \text{for } |\theta - \theta_w| \geq \frac{\pi}{2} \end{cases} \qquad (2.103)$$

For the first-generation formulation, the scale factor $\alpha$ is a constant and equals

$$\alpha = 0.0081 \qquad (2.104)$$

For the second-generation formulation, the scale factor $\alpha$ depends on the total dimensionless wave energy $\tilde{E}_{tot,sea}$ of the wind sea part of the spectrum and the dimensionless depth $\tilde{d}$:

$$\alpha = \max[(0.0081 + (0.013 - 0.0081)e^{-\tilde{d}}), 0.0023\tilde{E}_{tot,sea}^{-0.223}] \qquad (2.105)$$

where the total dimensionless wind sea wave energy $\tilde{E}_{tot,sea}$ is given by:

$$\tilde{E}_{tot,sea} = \frac{g^2 E_{tot,sea}}{U_{10}^4} \qquad (2.106)$$

with

$$E_{\text{tot,sea}} = \int_{\theta_w - \pi/2}^{\theta_w + \pi/2} \int_{0.7\sigma_{\text{PM,d}}}^{\infty} E(\sigma, \theta) d\sigma d\theta \qquad (2.107)$$

The maximum value of $\alpha$ is taken to be 0.155. This dependency of $\alpha$ on the local dimensionless energy of the wind sea permits an overshoot in the wave spectrum under wave generation conditions. For deep water $\alpha = 0.0081$ as proposed by Pierson and Moskowitz (1964).

## 2.4  Wave damping due to vegetation

Apart from the six processes as outlined in Section 2.3, SWAN has an option to include wave damping over a vegetation field (mangroves, salt marshes, etc.) at variable depths. A popular method of expressing the wave dissipation due to vegetation is the cylinder approach as suggested by Dalrymple *et al.* (1984). Here, energy losses are calculated as actual work carried out by the vegetation due to plant induced forces acting on the fluid, expressed in terms of a Morison type equation. In this method, vegetation motion such as vibration due to vortices and swaying is neglected. For relatively stiff plants the drag force is considered dominant and inertial forces are neglected. Moreover, since the drag due to friction is much smaller than the drag due to pressure differences, only the latter is considered. Based on this approach, the time-averaged rate of energy dissipation per unit area over the entire height of the vegetation is given by:

$$\varepsilon_{\text{v}} = \frac{2}{3\pi} \rho C_{\text{D}} b_{\text{v}} N_{\text{v}} \left( \frac{gk}{2\sigma} \right)^3 \frac{\sinh^3 k\alpha h + 3\sinh k\alpha h}{3k\cosh^3 kh} H^3 \qquad (2.108)$$

where $\rho$ is the water density, $C_{\text{D}}$ is the drag coefficient, $b_{\text{v}}$ is the stem diameter of cylinder (plant), $N_{\text{v}}$ is the number of plants per square meter, $\alpha h$ is the vegetation height, $h$ is the water depth and $H$ is the wave height. This formula was modified by Mendez and Losada (2004) for irregular waves. The mean rate of energy dissipation per unit horizontal area due to wave damping by vegetation is given by:

$$< \varepsilon_{\text{v}} > = \frac{1}{2\sqrt{\pi}} \rho \tilde{C}_{\text{D}} b_{\text{v}} N_{\text{v}} \left( \frac{gk}{2\sigma} \right)^3 \frac{\sinh^3 k\alpha h + 3\sinh k\alpha h}{3k\cosh^3 kh} H_{\text{rms}}^3 \qquad (2.109)$$

with $\tilde{C}_{\text{D}}$ is the bulk drag coefficient that may depend on the wave height. This is the only calibration parameter required for a given plant type.

To include wave damping due to vegetation in SWAN, Eq. (2.27) will be extended with $S_{\text{ds,veg}}$ based on Eq. (2.109). A spectral version of the vegetation dissipation model of Mendez and Losada can be obtained by expanding Eq. (2.109) to include frequencies and directions as follows

$$S_{\text{ds,veg}}(\sigma, \theta) = \frac{D_{\text{tot}}}{E_{\text{tot}}} E(\sigma, \theta) \qquad (2.110)$$

with

$$D_{\text{tot}} = -\frac{1}{2g\sqrt{\pi}}\tilde{C}_{\text{D}}b_{\text{v}}N_{\text{v}}\left(\frac{g\tilde{k}}{2\tilde{\sigma}}\right)^3\frac{\sinh^3 \tilde{k}\alpha h + 3\sinh \tilde{k}\alpha h}{3k\cosh^3 \tilde{k}h}H_{\text{rms}}^3 \tag{2.111}$$

where the mean frequency $\tilde{\sigma}$, the mean wave number $\tilde{k}$ are given by Eqs. (2.46) and (2.47), respectively. With $H_{\text{rms}}^2 = 8E_{\text{tot}}$, the final expression reads

$$S_{\text{ds,veg}} = -\sqrt{\frac{2}{\pi}}g^2\tilde{C}_{\text{D}}b_{\text{v}}N_{\text{v}}\left(\frac{\tilde{k}}{\tilde{\sigma}}\right)^3\frac{\sinh^3 \tilde{k}\alpha h + 3\sinh \tilde{k}\alpha h}{3k\cosh^3 \tilde{k}h}\sqrt{E_{\text{tot}}}E(\sigma,\theta) \tag{2.112}$$

Apart from extending the Mendez and Losada's formulation to a full spectrum, the possibility to vary the vegetation vertically is included. The contribution of each vertical segment is calculated individually with the total energy dissipation equal to the sum of the dissipation in each layer up till the still water level. With this implementation of the differences in characteristics of each layer, plants such as mangrove trees may be conveniently input into the SWAN model. The layer-wise segmentation is implemented by integration of the energy dissipation over height as follows:

$$S_{\text{ds,veg}} = \sum_{i=1}^{I} S_{\text{ds,veg},i} \tag{2.113}$$

where $I$ the number of vegetation layers and $i$ the layer under consideration with the energy dissipation for layer $i$. First, a check is performed to establish whether the vegetation is emergent or submergent relative to the water depth. In case of submergent vegetation the energy contributions of each layer are added up for the entire vegetation height. In case of emergent vegetation only the contributions of the layers below the still water level are taken into account. The implementation of vertical variation is illustrated in Figure 2.3. The energy dissipation term for a given layer $i$ therefore becomes

$$S_{\text{ds,veg},i} = -\sqrt{\frac{2}{\pi}}g^2\tilde{C}_{\text{D},i}b_{\text{v},i}N_{\text{v},i}\left(\frac{\tilde{k}}{\tilde{\sigma}}\right)^3\sqrt{E_{\text{tot}}}$$
$$\frac{\left(\sinh^3 \tilde{k}\alpha_i h - \sinh^3 \tilde{k}\alpha_{i-1} h\right) + 3\left(\sinh \tilde{k}\alpha_i h - \sinh \tilde{k}\alpha_{i-1} h\right)}{3k\cosh^3 \tilde{k}h}E(\sigma,\theta) \tag{2.114}$$

The corresponding terms for each layer can then be added and the total integrated as described earlier to obtain the energy dissipation over the entire spectrum. Here $h$ is the total water depth and $\alpha_i$ the ratio of the depth of the layer under consideration to the total water depth up to the still water level, such that

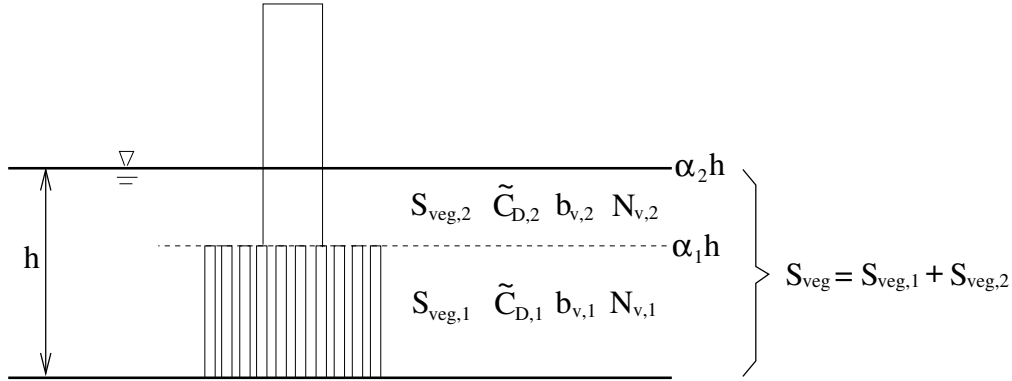$$\sum_{i=1}^{I} \alpha_i \leq 1 \tag{2.115}$$

Figure 2.3: Layer schematization for vegetation.

Finally, in addition to the vertical variation, the possibility of horizontal variation of the vegetation characteristics is included as well. This inclusion enables the vegetation in a given region to be varied so as to reflect real density variations in the field. Since, the parameters $\tilde{C}_D$, $b_v$ and $N_v$ are used in a linear way, we can use $N_v$ as a control parameter to vary the vegetation factor $V_f = \tilde{C}_D b_v N_v$ spatially, by setting $\tilde{C}_D = 1$ and $b_v = 1$, so that $V_f = N_v$.

An alternative vegatation model is due to Jacobsen et al. (2019) for waves propagating over a canopy, with which the associated energy dissipation is frequency dependent. The spectral distribution of the dissipation is given by

$$\delta_v = 2\Gamma S_u \sqrt{\frac{2m_{u,0}}{\pi}}$$

where $S_u$ is the velocity spectrum

$$S_u = \left( \frac{\sigma \cosh k(z+h)}{\sinh kh} \right)^2 S_\eta$$

with $S_\eta$ the energy density spectrum, i.e. $E(\sigma)$. The zeroth moment of the velocity spectrum is computed as

$$m_{u,0} = \int_0^\infty S_u \, df$$

Furthermore,

$$\Gamma = \frac{1}{2} \rho C_D b_v N_v \, \alpha_u^3$$

with $\alpha_u$ a velocity reduction factor.

The depth-integrated frequency-dependent dissipation is then found to be

$$S_{\text{ds,veg}} = -\frac{1}{\rho g} \int_{-h}^{-h+h_v} \delta_v \, dz$$

with $h_v$ the canopy height. The vertical integration is approximated using the Simpson's rule.

## 2.5   Wave damping due to sea ice

SWAN has an option to include wave dissipation by sea ice. Sea ice has two effects, direct and indirect. A direct dissipation of wave energy occurs due to the presence of sea ice. This dissipation is represented in SWAN using empirical formula. The temporal exponential decay rate of energy is

$$D_{\text{ice}} = S_{\text{ice}}/E = -2\,c_g\,k_i$$

where $S_{\text{ice}}$ is the sea ice sink term, and $E$ is the wave energy spectrum. Here, $k_i$ (in 1/m) is the linear exponential attenuation rate of wave amplitude in space, $a(x) = H_0 \exp(-k_i\,x)$. The factor 2 above provides a conversion from amplitude decay to energy decay. The group velocity $c_g$ provides conversion from spatial decay to temporal decay. $S_{\text{ice}}$ and $E$ vary with frequency and direction.

R19

In SWAN version 41.31, one option for this dissipation was available. This is a parameterization described in Collins and Rogers (2017) and is similar to the 'IC4M2' method implemented in the WAVEWATCH III model. That method, in turn, is a generalization of the formula proposed by Meylan et al. (2014). This implementation in SWAN is described in Rogers (2019), and so in the present version of SWAN, it is denoted as the 'R19'. With it, the model $k_i$ may vary with frequency according to

$$k_i\,(f) = c_0 + c_1\,f + c_2\,f^2 + c_3\,f^3 + c_4\,f^4 + c_5\,f^5 + c_6\,f^6$$

with $c_0$ to $c_6$ the user-defined polynomial coefficients. These coefficients are dimensional; e.g. $c_2$ has units of $\text{s}^2/\text{m}$.

The default R19 setting is the case of $c_2 = 1.06 \times 10^{-3}\ \text{s}^2/\text{m}$ and $c_4 = 2.3 \times 10^{-2}\ \text{s}^4/\text{m}$. This recovers the polynomial of Meylan et al. (2014), calibrated for a case of ice floes, mostly 10 to 25 m in diameter, in the marginal ice zone near Antarctica. Another calibration, for a case that is similar except with relatively thinner ice, from Rogers et al. (2021a) is $c_2 = 0.208 \times 10^{-3}\ \text{s}^2/\text{m}$ and $c_4 = 5.18 \times 10^{-2}\ \text{s}^4/\text{m}$. Other polynomials are provided in Rogers et al. (2018). An example is for a case of pancake and frazil ice: $c_2 = 0.284 \times 10^{-3}\ \text{s}^2/\text{m}$ and $c_4 = 1.53 \times 10^{-2}\ \text{s}^4/\text{m}$.

This 'R19' method does not depend on ice thickness. In version 41.31AB, three new methods are introduced which depend on ice thickness, denoted as 'D15', 'M18', and 'R21B'.

D15

The 'D15' method is a purely empirical formula from Doble et al. (2015), $k_i = C_{hf,D} f^{2.13} h_{ice}$, with default $C_{hf,D} = 0.1$ based on the same study, for pancake ice in the marginal ice zone (MIZ) of the Weddell Sea (Antarctica).

M18

The 'M18' method is the "Model with Order 3 Power Law" proposed by Meylan et al. (2018). This is a simple viscous model of the form $k_i = C_{hf,M} h_{ice}^1 f^3$, where $C_{hf,M}$ includes a viscosity parameter. Our implementation here has a default $C_{hf,M} = 0.059$ based on calibration to the Rogers et al. (2021a) dataset (broken floes in the Antarctic MIZ) by Rogers et al. (2021b). Two earlier calibrations were performed by Liu et al. (2020): $C_{hf,M} = 0.00751$ for a case of broken floes in the Antarctic MIZ and $C_{hf,M} = 0.0351$ for a case of pancake and frazil ice near the Beaufort Sea.

R21B

The 'R21B' method combines the Reynolds number non-dimensionalization proposed by Yu et al. (2019) with a simple monomial power fitting. This is documented in Rogers et al. (2021b). The resulting dimensional formula is $k_i = C_{hf} h_{ice}^{n/2-1} f^n$. Those authors calibrate it to the dataset of Rogers et al. (2021a), giving $n = 4.5$ and $C_{hf} = 2.9$.

Source term scaling

An indirect effect of sea ice is a reduction of wind input (scaling). The areal fraction of sea ice is given as $0 \leq a_{\text{ice}} \leq 1$. The effect on wind input is a scaling of the wind input source functions by open water fraction $1 - a_{\text{ice}}$,

$$S_{\text{in}} \leftarrow (1 - a_{\text{ice}}) \, S_{\text{in}}$$

with $S_{\text{in}}$ the wind input term; see Eq. (2.32). This effect can be reduced or disabled (see command `SET [icewind]`.)

Also, the ice source function is scaled with areal ice fraction, as follows

$$S_{\text{ice}} \leftarrow a_{\text{ice}} \, S_{\text{ice}}$$

The impact of sea ice on source terms in the real ocean is not known with any certainty, and instead is primarily based on intuition and guesswork; see discussion in Rogers et al. (2016). Nonlinear interactions are not scaled.

The sea ice treatment here has the following limitations:

- reflection and scattering by sea ice is not represented, and

- floe size distribution is not represented.

## 2.6 The influence of ambient current on waves

Waves are subject to the influence of ambient current, when they propagate on it. The ambient current can be tidal current, ocean current, local wind generated current, river current and wave generated current. It has been observed that current affects the growth

and decay of waves (Yu, 1952; Hedges *et al.*, 1985; Lia *et al.*, 1989). The observations have shown that in a strong opposite current the wave steepness and wave height increase significantly. These changes take place rapidly where the waves are blocked by the current, often accompanied with current-induced whitecapping and wave reflections. Moreover, at the blocking frequency action is also partially transferred away from the blocking frequency to higher and lower frequencies by nonlinear wave-wave interactions (Ris, 1997).

It was Longuet-Higgins and Stewart (1960, 1961, 1962) who founded the theoretical description of wave-current interactions. Since then, many additional results of wave-current interactions have been published. If waves propagate in the presence of ambient current, action density is conserved whereas energy density is not. Therefore, in SWAN the action balance equation has been adopted.

## 2.7   Modelling of obstacles

SWAN can estimate wave transmission through a (line-)structure such as a breakwater (dam). It is assumed that the obstacle is narrow compared to the grid size, i.e. a subgrid approach is applied. If in reality the width is large compared with grid size, the feature preferably is to be modeled as a bathymetric feature. The following text refers to narrow obstacles.

Such an obstacle will affect the wave field in three ways:

- it will reduce the wave height of waves propagating through or over the obstacle all along its length,

- it will cause waves to be reflected, and

- it will cause diffraction around its end(s).

In irregular, short-crested wave fields, however, it seems that the effect of diffraction is small, except in a region less than one or two wavelengths away from the tip of the obstacle (Booij *et al.*, 1993). Therefore the model can reasonably account for waves around an obstacle if the directional spectrum of incoming waves is not too narrow, unless one is interested in the wave field deep into the shadow zone.

Since obstacles usually have a transversal area that is too small to be resolved by the bottom grid in SWAN, an obstacle is modelled as a line in the computational area. See Section 3.11 for the numerical implementation of obstacles in SWAN.

### 2.7.1   Transmission

There are several mechanisms for transmission of waves. In SWAN, the user may compute transmission of waves passing over a dam with a closed surface or may choose a constant

transmission coefficient.

If the crest of the breakwater is at a level where (at least part of the) waves can pass over, the transmission coefficient $K_t$ (defined as the ratio of the (significant) wave height at the downwave side of the dam over the (significant) wave height at the upwave side) is a function of wave height and the difference in crest level and water level. It must be noted that the transmission coefficient can never be smaller than 0 or larger than 1. In SWAN, two expressions can be employed. The first is taken from Goda *et al.* (1967):

$$K_t = \begin{cases} 1 \,, & \frac{F}{H_i} < -\beta - \alpha \\ 0.5(1 - \sin(\frac{\pi}{2\alpha}(\frac{F}{H_i} + \beta))) \,, & -\beta - \alpha \le \frac{F}{H_i} \le \alpha - \beta \\ 0 \,, & \frac{F}{H_i} > \alpha - \beta \end{cases} \tag{2.116}$$

where $F = h - d$ is the freeboard of the dam and where $H_i$ is the incident (significant) wave height at the upwave side of the obstacle (dam), $h$ is the crest level of the dam above the reference level (same as reference level of the bottom), $d$ the mean water level relative to the reference level, and the coefficients $\alpha$, $\beta$ depend on the shape of the dam (Seelig, 1979) as given in Table 2.1. It should be noted that this formula is only valid for slopes more gentle than 1:0.7 (1.4:1 or 55 degrees). Expression (2.116) is based on experiments in a

Table 2.1: Parameters for transmission according to Goda *et al.* (1967).

| case | $\alpha$ | $\beta$ |
|---|---|---|
| vertical thin wall | 1.8 | 0.1 |
| caisson | 2.2 | 0.4 |
| dam with slope 1:3/2 | 2.6 | 0.15 |

wave flume, so strictly speaking it is only valid for normal incidence waves. Since there are no data available on oblique waves, it is assumed that the transmission coefficient does not depend on direction. Furthermore, it is assumed that the frequencies remain unchanged over an obstacle (only the energy scale of the spectrum is affected and not the spectral shape).

For an impermeable rough low-crested dam, the following expression of d'Angremond *et al* (1996) is chosen:

$$K_t = -0.4\frac{F}{H_i} + 0.64(\frac{B_k}{H_i})^{-0.31}(1 - e^{-0.5\xi_p}) \tag{2.117}$$

with $B_k$ the crest width and $\xi_p \equiv \tan\alpha/\sqrt{H_i/L_{0p}}$ the breaker parameter. For this, the slope of the breakwater $\alpha$ must be given and $L_{0p} = gT_p^2/2\pi$ is the deep water wave length. The restriction to eq. (2.117) is as follows:

$$0.075 \le K_t \le 0.9 \tag{2.118}$$

In most cases, the crest width is such that $B_k < 10H_i$. However, if this is not the case, the following expression should be used instead of (2.117):

$$K_t = -0.35\frac{F}{H_i} + 0.51(\frac{B_k}{H_i})^{-0.65}(1 - e^{-0.41\xi_p}) \tag{2.119}$$

with the restriction:

$$0.05 \le K_t \le -0.006\frac{B_k}{H_i} + 0.93 \tag{2.120}$$

The formula's (2.117) and (2.119) give a discontinuity at $B_k = 10H_i$. Following Van der Meer *et al* (2005), for practical application, Eq. (2.117) is applied if $B_k < 8H_i$, Eq. (2.119) if $B_k > 12H_i$ and in between ($8H_i \le B_k \le 12H_i$), a linear interpolation is carried out.

## 2.7.2   Reflection

Often there is reflection against quays or breakwaters. Depending on the nature of the obstacle (a smooth surface or a rubble-mound breakwater) the reflected wave field can be more or less scattered. SWAN is able to diffuse the reflection over wave components in different directions.

## 2.7.3   Freeboard dependent reflection and transmission

In case an obstacle becomes flooded, its reflection and transmission properties change as a function of the relative freeboard, defined as the ratio of the difference in dam height and the water level by the (incident) significant wave height, i.e. $F/H_s$. For transmission this dependence can be schematized as described in Section 2.7.1, where transmission increases with increasing freeboard. Another method is to scale the fixed reflection and fixed transmission coefficients as a function of the relative freeboard. This dependence is expressed using a `tanh` function in which a parameter $\gamma$ is employed to define the range (in terms of the relative freeboard) over which the fixed reflection and/or transmission coefficients varies between their minimum and maximum values. This dependency is given by

$$R = \left[1 + \tanh\left(\frac{2}{\gamma_{\mathrm{R}}}\frac{F}{H_s}\right)\right]\frac{R_0}{2}$$

in case of reflection with a fixed value $R_0$, and

$$T = \left[1 + \tanh\left(-\frac{2}{\gamma_{\mathrm{T}}}\frac{F}{H_s}\right)\right]\frac{T_0}{2}$$

in case of transmission with a fixed value $T_0$.

This parameterization has two gamma parameters, one for the reflection and one for the transmission. The parameterization is shown schematically in Figure 2.4. In this figure it is assumed that the fixed reflection coefficient $R_0$ has a value of 0.6, and that the maximum

or fixed transmission coefficient is equal to $T_0 = 0.9$. In this example the significant wave height has a value of 2 m. The structure of above equations is such that the parameters $\gamma_R$ and $\gamma_T$ coincide with the positions where the reflection and transmission coefficient have their minimum or maximum value.
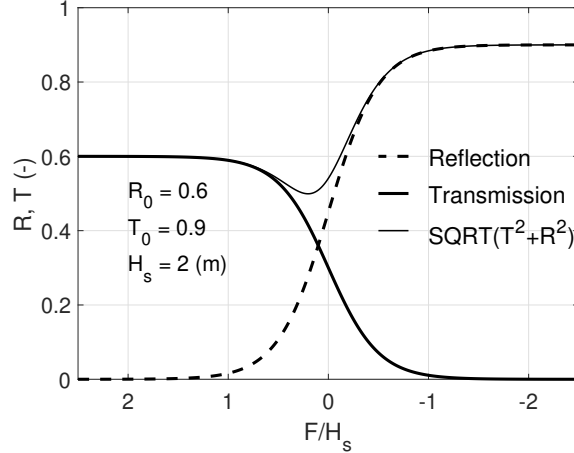


Figure 2.4: Parameterization of the reflection coefficient $R$ and transmission coefficient $T$ as a function of the relative freeboard $F/H_s$.

**Quay option**

The above parameterization works for an obstacle in water of a certain depth, irrespective from which side the waves are propagating. For handling this method for a quay, it is assumed that the water depth on each side of the obstacle line are different, where the quay area is less deep than the deeper area in front of the quay. This requires special attention of the model setup to ensure that the depths are different on the grid points at each side of the obstacle representing the edge of a quay. When waves propagate from the deeper side to the shallower (quay) side of the obstacle, the same method is used as above. When waves travel from the shallower part to the deeper part, it is assumed that the reflection coefficient $R = 0$ and the transmission coefficient $T = 1$.

## 2.7.4 Diffraction

To accommodate diffraction in SWAN simulations, a phase-decoupled refraction-diffraction approximation is suggested (Holthuijsen *et al.*, 2003). It is expressed in terms of the directional turning rate of the individual wave components in the 2D wave spectrum. The approximation is based on the mild-slope equation for refraction and diffraction, omitting phase information. It does therefore not permit coherent wave fields in the computational domain.

In a simplest case, we assume there are no currents. This means that $c_\sigma = 0$. Let denotes

the propagation velocities in geographic and spectral spaces for the situation without diffraction as: $c_{x,0}$, $c_{y,0}$ and $c_{\theta,0}$. These are given by:

$$c_{x,0} = \frac{\partial \omega}{\partial k} \cos \theta \,, c_{y,0} = \frac{\partial \omega}{\partial k} \sin \theta \,, c_{\theta,0} = -\frac{1}{k} \frac{\partial \omega}{\partial h} \frac{\partial h}{\partial n} \qquad (2.121)$$

where $k$ is the wave number and $n$ is perpendicular to the wave ray. We consider the following eikonal equation

$$K^2 = k^2(1 + \delta) \qquad (2.122)$$

with $\delta$ denoting the diffraction parameter as given by:

$$\delta = \frac{\nabla(cc_g \nabla \sqrt{E})}{cc_g \sqrt{E}} \qquad (2.123)$$

where $E(x, y)$ is the total energy of the wave field ($\sim H_s^2$). Due to diffraction, the propagation velocities are given by:

$$c_x = c_{x,0}\overline{\delta} \,, c_y = c_{y,0}\overline{\delta} \,, c_\theta = c_{\theta,0}\overline{\delta} - \frac{\partial \overline{\delta}}{\partial x}c_{y,0} + \frac{\partial \overline{\delta}}{\partial y}c_{x,0} \qquad (2.124)$$

where

$$\overline{\delta} = \sqrt{1 + \delta} \qquad (2.125)$$

In early computations, the wave fields often showed slight oscillations in geographic space with a wavelength of about $2\Delta x$ in $x-$direction. These unduly affected the estimations of the gradients that were needed to compute the diffraction parameter $\delta$. The wave field was therefore smoothed with the following convolution filter:

$$E_{i,j}^n = E_{i,j}^{n-1} - 0.2[E_{i-1,j} + E_{i,j-1} - 4E_{i,j} + E_{i+1,j} + E_{i,j+1}]^{n-1} \qquad (2.126)$$

where $i, j$ is a grid point and the superscript $n$ indicates iteration number of the convolution cycle. The width of this filter (standard deviation) in $x-$direction $\varepsilon_x$, when applied $n$ times is

$$\varepsilon_x \approx \frac{1}{2}\sqrt{3n}\Delta x \qquad (2.127)$$

By means of computations, $n = 6$ is found to be an optimum value (corresponding to spatial resolution of 1/5 to 1/10 of the wavelength), so that $\varepsilon_x \approx 2\Delta x$. For the $y-$direction, the expressions are identical, with $y$ replacing $x$. Note that this smoothing is only applied to compute the diffraction parameter $\delta$. For all other computations the wave field is not smoothed.

Diffraction in SWAN should <u>not</u> be used if,

- an obstacle or coastline covers a significant part of the down-wave view, <u>and</u>

- the distance to that obstacle or coastline is small (less than a few wavelengths), <u>and</u>

- the reflection off that obstacle or coastline is coherent, <u>and</u>

- the reflection coefficient is significant.

This implies that the SWAN diffraction approximation can be used in most situations near absorbing or reflecting coastlines of oceans, seas, bays, lagoons and fjords with an occasional obstacle such as islinds, breakwaters, or headlands but <u>NOT</u> in harbours or in front of reflecting breakwaters or near wall-defined cliff walls. Behind breakwaters (which may be reflecting), the SWAN results seem reasonable if the above conditions are met.

## 2.8  Wave-induced set-up

In a (geographic) 1D case the computation of the wave-induced set-up is based on the vertically integrated momentum balance equation which is a balance between the wave force (gradient of the wave radiation stress normal to the coast) and the hydrostatic pressure gradient (note that the component parallel to the coast causes wave-induced currents but no set-up).

$$\frac{dS_{xx}}{dx} + \rho g H \frac{d\overline{\eta}}{dx} = 0 \tag{2.128}$$

where $d$ is the total water depth (including the wave-induced set-up) and $\eta$ is the mean surface elevation (including the wave-induced set-up) and

$$S_{xx} = \rho g \int [n \cos^2 \theta + n - \frac{1}{2}] E d\sigma d\theta \tag{2.129}$$

is the radiation stress tensor.

Observation and computations based on the vertically integrated momentum balance equation of Dingemans *et al.* (1987) show that the wave-induced currents are mainly driven by the divergence-free part of the wave forces whereas the set-up is mainly due to the rotation-free part of these forces. To compute the set-up in 2D, it would then be sufficient to consider the divergence of the momentum balance equation. If the divergence of the acceleration in the resulting equation is ignored, the result is:

$$\frac{\partial F_x}{\partial x} + \frac{\partial F_y}{\partial y} - \frac{\partial}{\partial x}(\rho g H \frac{\partial \overline{\eta}}{\partial x}) - \frac{\partial}{\partial y}(\rho g H \frac{\partial \overline{\eta}}{\partial y}) = 0 \tag{2.130}$$

This approximation can <u>only</u> be applied to open coast (unlimited supply of water from outside the domain, e.g. nearshore coasts and estuaries) in contrast to closed basin, e.g. lakes, where this approach should not be used.

# Chapter 3

# Numerical approaches

## 3.1 Introduction

To design a spectral wave model many choices and assumptions need to be made. With the development of the SWAN model, initiated by Leo Holthuijsen, Nico Booij and Roeland Ris in 1993 and published in Booij et al. (1999), a number of principles and the scope have been established. These are as follows.

- SWAN must be suitable for both nearshore and oceanic applications. This model properly accounts for deep and shallow water wave processes (e.g. wind input, white capping, quadruplets, surf breaking and triads, as discussed in Section 2.3), and employs flexible meshes (curvilinear and triangular grids) to accommodate both small- and large-scale simulations. Typically, grid sizes can vary between 20 m (to resolve small-scale features in the seabed topography) and 100 km (to resolve large-scale features in the (hurricane) wind field). The action balance equation is formulated in Cartesian coordinates, and optionally in spherical coordinates.

- The discretization of the action balance equation must be simple, robust, accurate and economical for applications in coastal waters. Therefore a finite difference approach is employed based on the so-called method of lines. This means that the choice for time integration is independent of the choice for spatial discretization. In addition, time integration is fully implicit, which implies that the employed finite difference schemes are stable (in the Von Neumann sense) for an arbitrarily large time step irrespective of grid size. These schemes need only to be accurate enough for a time step and a grid size solely determined by physical accuracy for the scale of the phenomena to be simulated.

- The finite difference schemes for propagation of wave action in both geographic and spectral spaces must comply the causality principle, which is an essential property of the hyperbolic equation. Preservation of causality ensures that wave energy propagates in the right direction and at the right speed. Causality requires that wave energy being propagated from one point to another point further downstream must pass

through all the grid points on its path between them. As a consequence, propagation schemes must look for wave energy by following wave characteristics in an upwind fashion at the right speed, while satisfying a CFL criterion. In addition, a sweeping algorithm in compliance with the causality rule has been adopted.

- Moreover, the finite difference schemes must also obey the law of constant energy flux along the wave ray, which is necessary for correct wave shoaling, especially in case of rapidly varying bathymetry (e.g. seamounts, shelf breaks, main channels in estuaries, and floodplain areas in rivers).

- Finally, some measures have been employed to guarantee numerical stability at large time steps. These are the action density limiter, the frequency-dependent under relaxation in the iterative procedure, the conservative elimination of negative energy densities, the refraction limiter and the Patankar rules for linearization of the nonlinear source terms.

The numerical approaches outlining the abovementioned concepts, assumptions and principles will be discussed in the following sections.

## 3.2   Discretization

Discretization of Eq. (2.18) is carried out using the finite difference method. The homogeneous part of Eq. (2.18) is given by

$$\frac{\partial N}{\partial t} + \frac{\partial c_x N}{\partial x} + \frac{\partial c_y N}{\partial y} + \frac{\partial c_\sigma N}{\partial \sigma} + \frac{\partial c_\theta N}{\partial \theta} \ . \tag{3.1}$$

We choose a rectangular grid with constant mesh sizes $\Delta x$ and $\Delta y$ in $x-$ and $y-$direction, respectively. The spectral space is divided into elementary bins with a constant directional resolution $\Delta \theta$ and a constant relative frequency resolution $\Delta \sigma / \sigma$ (resulting in a logarithmic frequency distribution). We denote the grid counters as $1 \leq i \leq M_x$, $1 \leq j \leq M_y$, $1 \leq l \leq M_\sigma$ and $1 \leq m \leq M_\theta$ in $x-$, $y-$, $\sigma-$ and $\theta-$spaces, respectively. All variables, including e.g. wave number, group velocity, ambient current and propagation velocities, are located at points $(i, j, l, m)$. Time discretization takes place with the implicit Euler technique. We obtain the following approximation of Eq. (3.1):

$$\frac{N^n - N^{n-1}}{\Delta t}\Big|_{i,j,l,m} \quad + \quad \frac{[c_x N]_{i+1/2} - [c_x N]_{i-1/2}}{\Delta x}\Big|^n_{j,l,m} +$$

$$\frac{[c_y N]_{j+1/2} - [c_y N]_{j-1/2}}{\Delta y}\Big|^n_{i,l,m} +$$

$$\frac{[c_\sigma N]_{l+1/2} - [c_\sigma N]_{l-1/2}}{\Delta \sigma}\Big|^n_{i,j,m} +$$

$$\frac{[c_\theta N]_{m+1/2} - [c_\theta N]_{m-1/2}}{\Delta \theta}\Big|^n_{i,j,l} \ , \tag{3.2}$$

where $n$ is a time-level with $\Delta t$ a time step. In case of a stationary computation, the first term of Eq. (3.2) is removed and $n$ denotes an iteration level. Note that locations in between consecutive counters are reflected with the half-indices.

## 3.2.1 Discretization in geographical space

Since the unknown $N$ and the propagation velocities are only given in points $(i, j, l, m)$, further approximation is needed. A first order upwind scheme in geographical space may be employed, since it is fully monotone, i.e. it can not to give rise to spurious oscillations. A disadvantage of this scheme is that it is numerically diffusive, which naturally degrades the accuracy of the model. This numerical diffusion is caused by gradients of wave action across geographic space, e.g. due to refraction by bathymetry or currents, which is often small in coastal areas. So the wave energy field can be considered as smooth. However, in the current SWAN version, two alternatives to this scheme are implemented, namely the second order SORDUP and Stelling/Leendertse schemes. These schemes produce far less numerical diffusion and are appropriate for ocean and shelf sea (regional) applications.

First order upwind scheme; BSBT

The fluxes $c_x N$ at $(i + 1/2, j, l, m)$ and $c_y N$ at $(i, j + 1/2, l, m)$ are approximated with an upwind scheme as follows:

$$c_x N|_{i+1/2,j,l,m} = \begin{cases} c_x N|_{i,j,l,m}, & c_x|_{i,j,l,m} > 0 \\ c_x N|_{i+1,j,l,m}, & c_x|_{i,j,l,m} < 0 \end{cases} \tag{3.3}$$

and

$$c_y N|_{i,j+1/2,l,m} = \begin{cases} c_y N|_{i,j,l,m}, & c_y|_{i,j,l,m} > 0 \\ c_y N|_{i,j+1,l,m}, & c_y|_{i,j,l,m} < 0 \end{cases}. \tag{3.4}$$

The fluxes at $(i - 1/2, j, l, m)$ and $(i, j - 1/2, l, m)$ are obtained from (3.3) and (3.4), respectively, by decreasing the indices by 1 in appropriate manner. According to the solution algorithm, to be explained later in Section 3.3, both fluxes at $(i + 1/2, j, l, m)$ and $(i - 1/2, j, l, m)$ acts together with the same sign of $c_x$ (either positive or negative). Note that the flux $c_x N$ is considered as a whole quantity, and the propgation velocity $c_x$ is taken in its points of definition[1]. The same holds for the fluxes at $(i, j + 1/2, l, m)$ and $(i, j - 1/2, l, m)$ operating together with the same sign of $c_y$. These updates take place by ordering the grid points such that points solved later have no influence on the previous grid points. This ordering and the associated updates are carried out, for instance, during the first sweep if $c_x > 0$ and $c_y > 0$, and the resulting schemes read

$$\left( \frac{(c_x N)_i - (c_x N)_{i-1}}{\Delta x} \right)^n_{j,l,m} \tag{3.5}$$

---

[1]In the present context, we consider the discretization of the divergence operator applied to the energy flux. See Zijlema (2021) for details.

and

$$\left(\frac{(c_yN)_j - (c_yN)_{j-1}}{\Delta y}\right)^n_{i,l,m} \tag{3.6}$$

In this way the solution at a grid point is determined solely by its upstream points, and causality is preserved. In addition, the above schemes represent the divergence of energy flux, $\nabla_{\vec{x}} \cdot (\vec{c}_g N)$, at the discrete level. If there is no net flux change in the corresponding grid point, the divergence must be zero, which is obviously the case. For further details on this solution update, see Section 3.3.

The combination of the time and geographic space discretizations in Eqs. (3.2), (3.3) and (3.4) is known as a first order, backward space, backward time (BSBT) scheme. This scheme can be applied both in stationary and nonstationary simulations. This dimensionally split scheme is unconditionally stable, monotone and compact, but not optimal in terms of numerical cross-diffusion. (An example of a genuine multidimensional BSBT scheme with a reduced amount of cross-diffusion is considered for unstructured grids as discussed in Section 8.3.) The BSBT scheme can also be derived from the method of characteristics and therefore, it can be considered as a semi-Lagrangian scheme. This scheme is therefore consistent with local wave characteristics. This view is the basic philosophy of the numerical approach used in SWAN and is related to the fact that the energy flux must remain constant along a wave characteristic (see, e.g., Whitham (1974), pg. 245 and Eq. (11.61), and Holthuijsen (2007), pg. 200). This makes sure that the scheme is *flux conservative* which is necessary for wave shoaling over rapidly varying sea beds.

### SORDUP

For the SORDUP scheme, which is the default scheme for stationary computations, the second and third terms of Eq. (3.2) representing $x-$ and $y-$derivatives, respectively, are replaced by

$$\left(\frac{3(c_xN)_i - 4(c_xN)_{i-1} + (c_xN)_{i-2}}{2\Delta x}\right)^n_{j,l,m} \tag{3.7}$$

and

$$\left(\frac{3(c_yN)_j - 4(c_yN)_{j-1} + (c_yN)_{j-2}}{2\Delta y}\right)^n_{i,l,m} \tag{3.8}$$

in case of the first sweep, i.e. $c_x > 0$ and $c_y > 0$ (cf. Section 3.3). See also Rogers *et al.* (2002). This scheme, also known as a BDF scheme (Gear, 1971), is second accurate in space, but first order in time (not relevant), and is flux conservative (empirical evidence), but not monotone. In addition, this scheme preserves causality and produces less amount of numerical diffusion and is not significantly more expensive than the BSBT scheme.

In the neighboorhood of open boundaries, land boundaries and obstacles (i.e., the last two grids adjoining such grid points for the SORDUP scheme), SWAN will revert to the first order upwind BSBT scheme. This scheme has a larger numerical diffusion but that is usually acceptable over the small distances involved.

Stelling and Leendertse scheme

For the so-called cyclic scheme of Stelling and Leendertse (1992), which is the default scheme for <u>nonstationary</u> computations, the second and third terms of Eq. (3.2) representing $x-$ and $y-$derivatives, respectively, are replaced by

$$\left(\frac{10(c_xN)_i - 15(c_xN)_{i-1} + 6(c_xN)_{i-2} - (c_xN)_{i-3}}{12\Delta x}\right)^n_{j,l,m} + \left(\frac{(c_xN)_{i+1} - (c_xN)_{i-1}}{4\Delta x}\right)^{n-1}_{j,l,m} \tag{3.9}$$

and

$$\left(\frac{10(c_yN)_j - 15(c_yN)_{j-1} + 6(c_yN)_{j-2} - (c_yN)_{j-3}}{12\Delta y}\right)^n_{i,l,m} + \left(\frac{(c_yN)_{j+1} - (c_yN)_{j-1}}{4\Delta y}\right)^{n-1}_{i,l,m} \tag{3.10}$$

in case of the first sweep, i.e. $c_x > 0$ and $c_y > 0$ (cf. Section 3.3). See also Rogers *et al.* (2002). This scheme is second accurate in time and space, unconditionally stable, preserves causality, and is flux conservative (empirical evidence). Moreover, the amount of numerical diffusion generated by this scheme is significantly much smaller than both BSBT and SORDUP schemes.

In the neighboorhood of open boundaries, land boundaries and obstacles (i.e., the last three grids adjoining such grid points for the Stelling and Leendertse scheme), SWAN will revert to the first order upwind BSBT scheme.

Although the Stelling and Leendertse scheme is unconditionally stable, i.e. there is no restriction on the chosen time step, there is, however, a practical limitation to this time step because of the spurious oscillations produced by this scheme. These so-called wiggles can appear much more strongly in the numerical solution if the associated Courant number is much larger than 1. Contrary to the BSBT scheme, this low-diffusion scheme is not able to suppress the wiggles sufficiently. The largest acceptable Courant number is 10 (based on the fastest wave) which is, however, a subjective criterion (Rogers *et al.*, 2002).

Usually, the numerical diffusion of the Stelling and Leendertse scheme is so small that the so-called *garden-sprinkler effect* (GSE) may show up if propagation over very large distances is considered. This effect is due to the (coarse) spectral resolution (see Booij and Holthuijsen, 1987). It can be counteracted by anisotropic diffusion terms that have been explicitly added to the numerical scheme. Their values depend on the spectral resolution and the propagation time of the waves.

The diffusion applied <u>in the propagation direction</u> (locally along the wave ray) is

$$D_{ss} = \frac{\Delta c_g^2 T}{12}$$

where $\Delta c_g$ is the difference in the group velocities of successive frequencies, and $T$ is the so-called wave age, i.e. the time elapsed since the propagated swell was generated by the

storm. The diffusion <u>normal to the propagation direction</u> (locally along the wave crest) is

$$D_{nn} = \frac{c_g^2 \Delta\theta^2 T}{12}$$

From these, diffusion coefficients in Cartesian coordinates are calculated as

$$D_{xx} = D_{ss}\cos^2\theta + D_{nn}\sin^2\theta \,,$$
$$D_{yy} = D_{ss}\sin^2\theta + D_{nn}\cos^2\theta \,,$$
$$D_{xy} = (D_{ss} - D_{nn})\cos\theta\sin\theta$$

The diffusion terms to be added to Eq. (3.1) are given by

$$-D_{xx}\frac{\partial^2 N}{\partial x^2} - 2D_{xy}\frac{\partial^2 N}{\partial x \partial y} - D_{yy}\frac{\partial^2 N}{\partial y^2}$$

Each of these second derivative terms is approximated in space using second order central differences, at time level $n-1$, as follows

$$D_{xx}\left(\frac{N_{i+1} - 2N_i + N_{i-1}}{\Delta x^2}\right)^{n-1}_{j,l,m}$$

$$D_{yy}\left(\frac{N_{j+1} - 2N_j + N_{j-1}}{\Delta y^2}\right)^{n-1}_{i,l,m}$$

$$D_{xy}\left(\frac{N_{i,j} - N_{i-1,j} - N_{i,j-1} + N_{i-1,j-1}}{\Delta x \Delta y}\right)^{n-1}_{l,m}$$

This explicit scheme is fast (having little impact on computation time) but only conditionally stable. Through mathematical analysis (not shown) it can be shown that a likely stability condition is (Rogers *et al*, 2002)

$$Q = \frac{\max(D_{xx}, D_{yy}, D_{xy})\Delta t}{\min(\Delta x, \Delta y)^2} \le \frac{1}{2} \qquad (3.11)$$

Thus, it is credible that Eq. (3.11) holds true for the two-dimensional Stelling and Leendertse scheme with this GSE correction. In short, by adding the GSE correction, the unconditionally stable advection scheme of SWAN becomes a conditionally stable advection-diffusion scheme. This restriction appears not to be severe as is commonly believed for a typical advection-diffusion equation. In experiments, it was found that with $Q \le 0.48$, no instability was observed (Rogers *et al*, 2002). It is readily shown that for typical ocean applications $D_{nn}$ dominates the diffusion and $Q$ can be written as

$$Q = \frac{c_g^2 T \Delta t \Delta\theta^2}{12\Delta x^2} \qquad (3.12)$$

The variable wave age $T$ could be computed during the computations of SWAN but it requires the same order of magnitude of computer memory as integrating the action balance equation. Instead a constant wave age $\overline{T}$ can be used as an approximation, so that Eq. (3.12) becomes

$$Q = \frac{\overline{L}\mu\Delta\theta^2}{12\Delta x} \tag{3.13}$$

where the characteristic travel distance of the waves is $\overline{L} = c_g\overline{T}$ (e.g., the dimension of the ocean basin) and $\mu = c_g\Delta t/\Delta x$ is the Courant number. For oceanic applications, the Courant number is typically $\mu \approx \frac{1}{2}$ so that $Q \leq \frac{1}{4}$ for typical values of $\Delta\theta \sim 10^o$ and $\overline{L}/\Delta x \sim 200$ (the number of grid points in one direction of the grid). This implies that the Stelling and Leendertse scheme with the GSE correction is stable for typical ocean cases. For shelf sea (regional) applications, the value of $\mu = \mathcal{O}(1)$ but the garden-sprinkler effect tends to be small on these scales and the diffusion can and should not be used to avoid the stability problem. For small-scale (local) applications, typically $\mu = \mathcal{O}(10 - 100)$. But such cases are usually treated as stationary and the SORDUP scheme (no GSE correction is included in this scheme), or preferably the BSBT scheme, should be used. See also Rogers *et al.* (2002) for further details.

## 3.2.2   Note on the choice of geographic propagation schemes

The main interest of the SWAN users is in simulating wind-generated waves and combined swell-sea cases in *coastal ocean waters*, and it is particularly with the view to such computations that a simple and compact, but first order BSBT scheme was implemented in SWAN. A substantial body of experience gathered over the past 20 years on the performance of both lower and higher upwind schemes in SWAN suggests that in many circumstances, the discretization of the propagation terms in geographical space is not a crucial issue. Many nearshore simulations have shown the solution for action density to be on the whole rather insensitive to the accuracy with which geographic propagation terms are approximated. This reflects the tendency for the level of wave action to be dictated by source terms, while the local changes of the energy field across geographical space is relatively weak. This is consonant with the established view that a certain amount of numerical diffusion can be safely tolerated in the numerical scheme for geographic propagation, as its impact on wave parameters is negligible (Rogers *et al.*, 2002; WISE Group, 2007). Also, broad wave spectra will tend make numerical diffusion far less noticeable in a wave field.

This would appear to suggest, however, that the use of higher order upwind schemes serves no useful purpose. This is probably not so since there might be some cases that are prone to diffusion, where the benefit of such schemes is obvious. One can think of a case of swell propagation over very long distances. While low-diffusive, higher order schemes did permit long-distance swell cases to be validated, the reduced diffusion was found to pose a serious difficulty as the garden sprinkler effect becomes more visible, see e.g. WISE Group (2007).

### 3.2.3   Discretization in spectral space

The fluxes in the spectral space $(\sigma, \theta)$, as given in Eq. (3.2), should not be approximated with the first order upwind scheme since, it turns out to be very diffusive for frequencies near the blocking frequency[2]. Central differences should be used because of second order accuracy. However, such schemes tend to produce unphysical oscillations due to relatively large gradients in action density near the blocking frequency. Instead, a hybrid central/upwind scheme is employed:

$$c_\sigma N|_{i,j,l+1/2,m} = \begin{cases} (1-0.5\mu)c_\sigma N|_{i,j,l,m} + 0.5\mu c_\sigma N|_{i,j,l+1,m}, & \text{if shifting to higher frequencies} \\[2mm] (1-0.5\mu)c_\sigma N|_{i,j,l+1,m} + 0.5\mu c_\sigma N|_{i,j,l,m}, & \text{if shifting to lower frequencies} \end{cases}$$
$$(3.14)$$

and

$$c_\theta N|_{i,j,l,m+1/2} = \begin{cases} (1-0.5\nu)c_\theta N|_{i,j,l,m} + 0.5\nu c_\theta N|_{i,j,l,m+1}, & \text{if counter-clockwise} \\[2mm] (1-0.5\nu)c_\theta N|_{i,j,l,m+1} + 0.5\nu c_\theta N|_{i,j,l,m}, & \text{if clockwise} \end{cases} , \quad (3.15)$$

where the parameters $\mu$ and $\nu$ are still to be chosen. For all values $\mu \in [0,1]$ and $\nu \in [0,1]$, a blended form arises between first order upwind differencing ($\mu = \nu = 0$) and central differencing ($\mu = \nu = 1$). Like the fluxes in the geographical space, both fluxes at $(i,j,l+1/2,m)$ and $(i,j,l-1/2,m)$ acts together with the same sign of $c_\sigma$. The same holds for fluxes at $(i,j,l,m+1/2)$ and $(i,j,l,m-1/2)$ acting together with the same sign of $c_\theta$. Note that the above scheme is flux conservative and thus suitable for cases with rapidly varying bathymetry.

Let us consider a few examples for the purpose of the last term of Eq. (3.1), i.e. the refraction term. We substitute approximation (3.15) in the last term of Eq. (3.2), and central differences ($\nu = 1$) yields (keep in mind that bin $m$ is the bin of consideration for the approximation of this refraction term)

$$\left( \frac{(c_\theta N)_{m+1} - (c_\theta N)_{m-1}}{2\Delta\theta} \right)^n_{i,j,l}$$

whereas for the counter-clockwise case $c_\theta|_m > 0$ and $c_\theta|_{m-1} > 0$, first order upwinding ($\nu = 0$) returns

$$\left( \frac{(c_\theta N)_m - (c_\theta N)_{m-1}}{\Delta\theta} \right)^n_{i,j,l}$$

and for the clockwise case $c_\theta|_{m+1} < 0$ and $c_\theta|_m < 0$, we have

$$\left( \frac{(c_\theta N)_{m+1} - (c_\theta N)_m}{\Delta\theta} \right)^n_{i,j,l}$$

---

[2]Waves can be blocked by the current at a relative high frequency.

It is important to note that we consider the flux $c_\theta N$ as one single quantity defined in directional bins only. Suppose that the divergence of this flux is zero. Applying the above upwind approximations implies that the wave action flux is constant in every directional bin. Hence, this upwind scheme ($\nu = 0$) preserves exactly the constancy of this flux. This is called *pointwise conservation*. Note that this scheme also preserves causality. Although the central difference scheme ($\nu = 1$) is flux conservative, it is not pointwise conservative. Furthermore, due to the nature of this approximation a checkerboard problem may arise. Therefore, in practice, we always choose $0 \leq \nu < 1$ in SWAN.

The usual choice in SWAN is $\nu = \frac{1}{2}$. This approximation contains three consecutive transport velocities which can either be positive or negative. In other cases, they are negligibly small (zero crossing), for which central differences ($\nu = 0$) will then be applied (no clear wave direction). We first consider the counter-clockwise case $c_\theta|_{m+1} > 0$, $c_\theta|_m > 0$ and $c_\theta|_{m-1} > 0$, and the associated approximation then reads

$$\left( \frac{(c_\theta N)_{m+1} + 2(c_\theta N)_m - 3(c_\theta N)_{m-1}}{4\Delta\theta} \right)^n_{i,j,l}$$

This choice has a smaller amount of numerical diffusion than the upwind scheme, but may create wiggles, albeit small. This asymmetric approximation, containing three distinctive fluxes, indicates that the waves are turning counter-clockwise where both bins $m$ and $m+1$ are receiving energy from the bin $m - 1$. However, bin $m + 1$ receives less energy than bin $m$. Hence, it slows down the turning of the waves. Since the downstream bin $m + 1$ receives some energy, this scheme violates causality. Furthermore, although this scheme is flux conservative, it is not pointwise conservative, i.e. the energy flux may not remain constant in each directional bin. The other case is the clockwise one, i.e. $c_\theta|_{m+1} < 0$, $c_\theta|_m < 0$ and $c_\theta|_{m-1} < 0$. For this case, the approximation is given by

$$\left( \frac{3(c_\theta N)_{m+1} - 2(c_\theta N)_m - (c_\theta N)_{m-1}}{4\Delta\theta} \right)^n_{i,j,l}$$

Note that changes in wave action from one spectral bin to another are usually small, at least away from blocking frequency and considering broad wave spectra, so that both the numerical dispersion and diffusion produced by the hybrid scheme and its lack of causality preservation is likely to be much less significant.

## 3.2.4   Conservative elimination of negative energy densities

The numerical solution obtained with the hybrid central/upwind scheme Eqs. (3.14) and (3.15) is, in principle, not free from spurious oscillations or wiggles, unless $\mu = \nu = 0$. However, these wiggles will not result in negative densities in the energy-containing part of the two-dimensional wave spectrum, as they occur against a background level of energy. On the other hand, the flanks of the spectrum are immediately adjacent to bins of zero energy.

Hence, negative energy prevails especially in these flanks, either at very low frequencies ($\sim 0.03$ Hz) or in the edges of spread waves, which is likely to be generated by the hybrid scheme exhibiting numerical dispersion. Since broad banded wave energy field is relatively smooth away from blocking frequency (low gradients), these negative energy densities tend to be rather small. They can be effectively removed through the so-called *conservative elimination* (Tolman, 1991). In short, all negative energy density for each frequency within a sweep is removed, and the energy densities for all directions within this directional sector at a given frequency are multiplied by a constant factor to conserve energy.

The conservative elimination algorithm is outlined as follows. For a given frequency $f$ and a given directional range $[\theta_1, \theta_2]$ of one of the four sweeps, we differentiate between positive and negative contributions of the energy density, as follows

$$E(f, \theta) = E^+(f, \theta) + E^-(f, \theta)$$

with $E^+ > 0$ and $E^- < 0$. Next, we compute the total energy within the sweep at frequency $f$

$$E_{\text{tot}}(f) = \int_{\theta_1}^{\theta_2} E(f, \theta)\, d\theta$$

and we integrate the positive densities over the considered directions

$$E_{\text{tot}}^p(f) = \int_{\theta_1}^{\theta_2} E^+(f, \theta)\, d\theta$$

Based on these two quantities, we compute the following factor

$$\alpha(f) = \frac{E_{\text{tot}}(f)}{E_{\text{tot}}^p(f)} \leq 1$$

Finally, we remove the negative contributions by setting $E^-(f, \theta) = 0$, while the positive densities are multiplied by factor $\alpha(f)$ to preserve the total energy at given frequency $f$.

The effectiveness of this conservative elimination algorithm can, however, be poor for a number of reasons. One of the reasons is that the directional resolution is too coarse for the scale of directional spreading, so that energy is spread over a few directional bins. For instance, a wave spectrum with small directional spreading ($< 10^o$) distributed over a number of directional bins of each $10^o$ within a sweep. As a result, within this directional sector the total amount of negative densities can be larger than the amount of positive ones. This implies $\alpha < 0$. In such a case, conserving energy within this sweep makes no sense, and we will then eliminate the negative energy densities and to leave the positive densities as they are. This is called *strict elimination*. It must be noted that in that case the hybrid scheme Eq. (3.15) is inaccurate anyway, and strict elimination will most likely not worsen this case.

Another reason is the frequent occurrence in the exchange of wave energy between directional sweep sectors (see Section 3.4 for details), which may enhance the gradient in

the energy density locally and thereby generates more negative energy densities. This is particular the case if the directional discretization is too coarse for the scale of spreading. Finally, a relatively strong turning rate tends to provoke strict elimination.

As a rule, for a typical field case over 95% of the number of occurrences of elimination of negative energy densities concerns conservative elimination. Hence, less than 5% of this number is related to (non-conserved) strict elimination, which is acceptable.

## 3.3   Solution algorithm

The implicit discretization of the action balance equation (2.18) as described in Section 3.2 yields a system of linear equations that need to be solved. The corresponding matrix structure can take different forms, mainly depending on the propagation of wave energy in the geographic space. For instance, suppose that $c_x > 0$ and $c_y > 0$, everywhere. Then, the matrix structure has the following form:

$$
\begin{bmatrix}
\begin{pmatrix} .x.xxx.x.. \\ ..x.xxx.x. \\ ...x.xxx.x \end{pmatrix} & & \\[2em]
\begin{pmatrix} ....x....... \\ ......x..... \\ ........x... \end{pmatrix} & \begin{pmatrix} .x.xxx.x.. \\ ..x.xxx.x. \\ ...x.xxx.x \end{pmatrix} & \\[2em]
\begin{pmatrix} ....x....... \\ ......x..... \\ ........x... \end{pmatrix} & \begin{pmatrix} ....x....... \\ ......x..... \\ ........x... \end{pmatrix} & \begin{pmatrix} .x.xxx.x.. \\ ..x.xxx.x. \\ ...x.xxx.x \end{pmatrix}
\end{bmatrix} . \tag{3.16}
$$

One recognizes that the subblocks on the main diagonal express coupling among the unknowns in the $(\sigma, \theta)-$space for each geographic grid point, whereas the off-diagonal subblocks represent coupling across geographical grid points. The ordering of grid points is determined by the direction of wave propagation. This system can be solved with a Gauss-Seidel technique in one step, if the wave characteristic is a straight line and constant everywhere (Wesseling, 1992). In addition, this number is independent of grid size. Hence, the complexity of this algorithm is $\mathcal{O}(M)$ for a total of $M$ grid points.

After each propagation update at geographic grid point, an update in the spectral space must be made. We divide all wave directions into a number of groups according to their directions, and order the grid points accordingly for the update. This is called a sweep. Since every internal grid point has the same number of edges with fixed directions, same division can be made within the $(\sigma, \theta)$-space, resulting in four quadrants of each $90^o$, as illustrated in Figure 3.1. In this case we have four sweeps and the selected wave directions in each sweep form the domain of dependence appropriate for update. This immediately

satisfies the CFL criterion. This criterion is related to the causality principle. In general, a numerical scheme must look for information by following characteristics in an upwind fashion. Causality can be preserved in the iteration process by means of ordering grid points according to the propagation direction, which guarantees convergence in a finite number of iterations. We will come back to that later in Section 3.4.
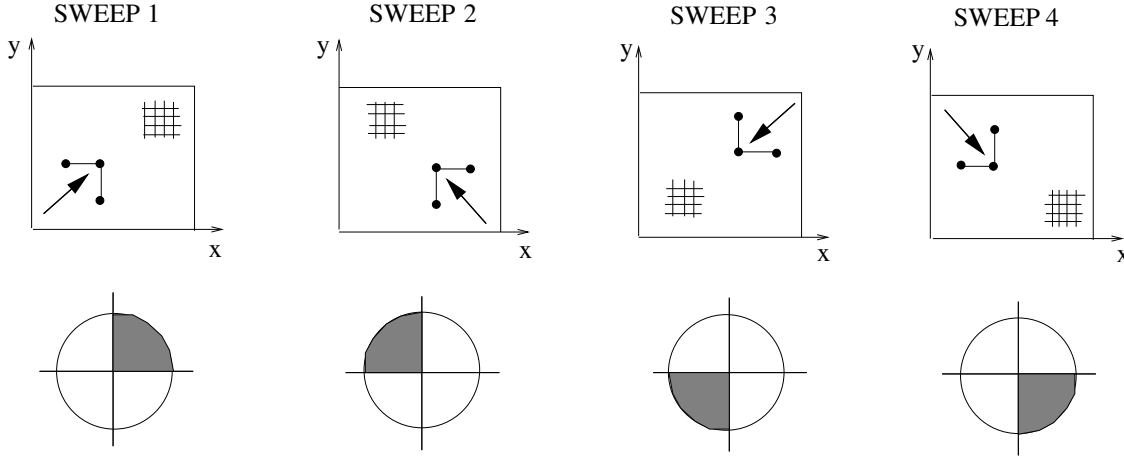


Figure 3.1: The solution procedure for wave energy propagation in geographical space with the appropriate directional quadrant (indicated by shaded area) for each of four sweeps.

The Gauss-Seidel iteration process is done as follows. For each iteration, sweeping through grid rows and columns in geographical domain are carried out, starting from each of the four corners of the computational grid. After four sweeps, wave energy has been propagated over the entire geographical domain. During each sweep, only a subset of the unknown values of $N$ are updated depending on the sign of $c_x$ and $c_y$. For instance, the first sweep starts at the lower left hand corner and all grid points with $c_x > 0$ and $c_y > 0$ are updated. Because of the causality principle these transport velocities must be positive in those ordered grid points along the wave ray, in order to make a stable iterative update. Moreover, adapting the ordering of updates of the unknowns $N$ in geographical space to the propagation direction improves the rate of convergence of the Gauss-Seidel iterative procedure (Wesseling, 1992). For an illustrative explanation of this technique, see Section 3.5.

Due to the implicit nature of the spectral propagation terms in Eq. (3.2), a system of equations must be formed (i.e. one of the main diagonal of the matrix Eq. (3.16)). Furthermore, due to the fact that the source term $S_{\text{tot}}$ in Eq. (3.2) is nonlinear in $N$, linearization is required in order to find a solution. Generally, the term $S_{\text{tot}}$ in each bin $(l, m)$ is treated by distinguishing between positive and negative contributions and arranging these in the linear form (Ferziger and Perić, 1999):

$$S_{\text{tot}} = S_{\text{tot}}^p + S_{\text{tot}}^n N \,, \tag{3.17}$$

where $S_{\text{tot}}^p$ consists of positive contributions and $S_{\text{tot}}^n$ of negative ones. Both contributions are independent of the solution $N$ at the corresponding bin $(l, m)$. Any negative term that does not contain $N$ as a multiplier is first divided by $N$ obtained from the previous iteration level and then added to $S_{\text{tot}}^n$. This stabilizes the iteration process. Details on the application of this principle to each source term in SWAN can be found in Booij *et al.* (1999).

The strongly nonlinear source term of depth-induced wave breaking is linearized by means of the Newton-Raphson iteration, as follows:

$$S^n \approx \phi^{n-1}E^n + \left(\frac{\partial S}{\partial E}\right)^{n-1}(E^n - E^{n-1}) \tag{3.18}$$

Since this process of depth-induced wave breaking has been formulated such that $S = aS_{\text{tot}}$ and $E = aE_{\text{tot}}$, the derivative $\partial S/\partial E$ is analytically determined as $\partial S_{\text{tot}}/\partial E_{\text{tot}}$. Here, $a$ is identical in both expressions and the total energy $E_{\text{tot}}$ and total source $S_{\text{tot}}$ are the integrals over all frequencies and directions of $E(\sigma, \theta)$ and $S_{\text{ds,br}}(\sigma, \theta)$, respectively.

As such, each difference equation (3.2) using expressions (3.14), (3.15) and (3.17) provides an algebraic relation between $N$ at the corresponding bin and its nearest neighbours:

$$a_P N_P = a_L N_L + a_R N_R + a_B N_B + a_T N_T + b_P, \tag{3.19}$$

where P corresponds to central bin $(l, m)$ and L(eft), R(ight), B(ottom) and T(op) correspond to $(l-1, m)$, $(l+1, m)$, $(l, m-1)$ and $(l, m+1)$, respectively. Furthermore, the coefficients $a_k$, $k \in \{P, L, R, B, T\}$ arise from the discretizations of the fluxes $c_\sigma N$ and $c_\theta N$ and $b_P$ contains the positive contributions of the source term $S_{\text{tot}}^p$ in (3.17) and the updated fluxes $c_x N$ (3.3) and $c_y N$ (3.4). Note that coefficient $a_P$ includes $-S_{\text{tot}}^n$.

The linear system of equations (3.19) for all bins within a directional quadrant at a particular geographical point is denoted by

$$A\vec{N} = \vec{b}, \tag{3.20}$$

where $A \in \mathbb{R}^{K \times K}$ contains the coefficients $a_k$, $k \in \{P, L, R, B, T\}$ (and corresponds to a subblock on the main diagonal of (3.16)), $\vec{b} \in \mathbb{R}^K$ contains the coefficient $b_P$ and boundary values and $\vec{N} \in \mathbb{R}^K$ denotes an algebraic vector containing the unknown action density values. Matrix $A$ is non-symmetric. The dimension $K$ of a directional quadrant equals $N_\sigma \times 1/4 N_\theta$. Note that linearization of the source term (3.17) enhances diagonal dominance of $A$, thereby improving numerical stability. Also note that neither $A$ nor $\vec{b}$ depends on the unknowns. Each row in the matrix $A$ corresponds to a bin $(l, m)$. The main diagonal contains the coefficients $a_P$ and directly to the left and right are the coefficients $-a_B$ and $-a_T$, respectively. The coefficients $-a_L$ and $-a_R$ are on the diagonals that are $N_\theta$ positions to the left and right of the main diagonal, respectively.

The solution $\vec{N}$ is given by $A^{-1}\vec{b}$. Since, the only non-zero matrix elements are situated in

five diagonals, iterative solution methods that utilize the sparsity of $A$ optimally are very attractive. In SWAN, the solution of Eq. (3.20) is found by means of an incomplete lower-upper decomposition method followed by an iteration process called the Strongly Implicit Procedure (SIP) (Ferziger and Perić, 1999). This procedure is specifically designed for (non-symmetric) penta-diagonal systems and is relatively fast. Note that in the absence of mean current there are no shifts in the frequency, and consequently the structure of $A$ reduces to a tri-diagonal one, i.e. $a_{\mathrm{L}} = a_{\mathrm{R}} = 0$, which can be inverted efficiently with the Thomas algorithm (Press *et al.*, 1993; Ferziger and Perić, 1999).

## 3.4   Iteration process and stopping criteria

Generally, the velocities $c_x$ and $c_y$ have different signs in the geographical domain and hence, more steps are needed. Energy propagates along a wave ray and this cannot be done in 1 iteration as soon as this ray is curved. Wave rays can be curved in coastal waters due to depth changes and ambient current. This enhances the number of iterations as it must cover the propagation of energy density along the whole characteristic curve. The key issue is the maximum number of iterations needed to cover energy propagation across the model domain.

Any wave ray can be divided into a finite number of pieces so that each piece can be covered effectively by one of the four sweeps. This number is related to the directional change of the wave ray. Since these pieces have to be captured sequentially the total number of iterations needed is proportional to the number of pieces. In turn, this number depends on the size of the model domain and the way the waves propagate through the domain.

If the source terms are included then in every wet grid point a balance between refraction, wind input, white capping, wave breaking, etc. within the spectral space is evaluated. On top of this various wave components are marching in the model domain from the open boundaries. It depends on the strength of the source terms on the one hand and propagation throughout the domain and the domain size on the other hand how many iterations are actually needed. As a matter of fact, the total number of iterations depends rather on the local change in wave propagation e.g. in shallow waters, tidal inlets, and around shoals, irrespective of the ordering and sweeping.

Due to refraction and nonlinear wave energy transfer, interactions occur between the directional quadrants. To properly take these interactions into account and the fact that we employ the Gauss-Seidel technique and linearization of the source term (3.17), the quadrant sweeping and the solution of system (3.20) need to be repeated until some convergence criteria are met. The iteration process runs from $s = 1$ to $s = S$ and is terminated if the maximum number of iterations $S$ (usually 50) is reached or the following criteria for the significant wave height $H_{m0}$ and mean relative wave period $T_{m01}$, as given by

$$H_{m0} = 4\sqrt{m_0}\,, \quad T_{m01} = 2\pi \frac{m_0}{m_1}\,, \quad m_j = \int_0^\infty \int_0^{2\pi} \sigma^j E(\sigma, \theta) d\sigma d\theta\,, \qquad (3.21)$$

are both satisfied in at least 98% of all wet grid points $(i, j)$:

$$\frac{|\Delta H_{m0}^s(i,j)|}{H_{m0}^{s-1}(i,j)} < \varepsilon_{\mathrm{H}}^{\mathrm{r}} \quad \text{or} \quad |\Delta H_{m0}^s(i,j)| < \varepsilon_{\mathrm{H}}^{\mathrm{a}} \tag{3.22}$$

and

$$\frac{|\Delta T_{m01}^s(i,j)|}{T_{m01}^{s-1}(i,j)} < \varepsilon_{\mathrm{T}}^{\mathrm{r}} \quad \text{or} \quad |\Delta T_{m01}^s(i,j)| < \varepsilon_{\mathrm{T}}^{\mathrm{a}} . \tag{3.23}$$

Here, $\Delta Q^s \equiv Q^s - Q^{s-1}$, with $Q$ some quantity. The default values of this limiting criteria are: $\varepsilon_{\mathrm{H}}^{\mathrm{r}} = \varepsilon_{\mathrm{T}}^{\mathrm{r}} = 0.02$, $\varepsilon_{\mathrm{H}}^{\mathrm{a}} = 0.02$ m and $\varepsilon_{\mathrm{T}}^{\mathrm{a}} = 0.2$ s. The rationale behind the use of the integral wave parameters $H_{m0}$ and $T_{m01}$ in the stopping criteria is that these are the output variables typically of interest. The iterative solution procedure is accelerated by calculating a reasonable first guess of the wave field based on second-generation source terms of Holthuijsen and De Boer (1988).

In general, the iterative method should be stopped if the approximate solution is accurate enough. A good termination criterion is very important, because if the criterion is too weak the solution obtained may be useless, whereas if the criterion is too severe the iteration process may never stop or may cost too much work. Experiences with SWAN have shown that the above criteria (3.22) and (3.23) are often not strict enough to obtain accurate results after termination of the iterative procedure. It was found that the iteration process can converge so slowly that at a certain iteration $s$ the difference between the successive iterates, $H_{m0}^s - H_{m0}^{s-1}$, can be small enough to meet the convergence criteria, causing the iteration process to stop, even though the converged solution has not yet been found. In particular, this happens when convergence is non-monotonic such that the process is terminated at local maxima or minima that may not coincide with the converged solution.

Furthermore, it became apparent that, unlike $H_{m0}$, the quantity $T_{m01}$ is not an effective measure of convergence. It was found that the relative error in $T_{m01}$, i.e. $|T_{m01}^s - T_{m01}^{s-1}|/T_{m01}^{s-1}$, does not monotonically decrease near convergence, but keeps oscillating during the iteration process. This behaviour is due to small variations in the spectrum at high frequencies, to which $T_{m01}$ is sensitive. This behaviour is problematic when any form of stricter stopping criterion is developed based on $T_{m01}$. Therefore, in the improved termination criterion proposed, $T_{m01}$ has been abandoned as a convergence measure and only $H_{m0}$, which displays more monotonic behaviour near convergence, is retained.

Stiffness and nonlinearity of the action balance equation are found to yield less rapid and less monotone convergence. Ferziger and Perić (1999) explain the slow convergence in terms of the eigenvalue or spectral radius of the iteration process generating the sequence $\{\phi^0, \phi^1, \phi^2, ...\}$. They show that the actual solution error is given by

$$\phi^\infty - \phi^s \approx \frac{\phi^{s+1} - \phi^s}{1 - \rho} , \tag{3.24}$$

where $\phi^\infty$ denotes the steady-state solution and $\rho$ is the spectral radius indicating the rate of convergence. The smaller $\rho$, the faster convergence. This result shows that the solution

error is larger than the difference between successive iterates. Furthermore, the closer $\rho$ is to 1, the larger the ratio of solution error to the difference between successive iterates. In other words, the lower the rate of convergence of the iteration process, the smaller this difference from one iteration to the next must be to guarantee convergence. The stopping criterion of SWAN could be improved by making the maximum allowable relative increment in $H_{m0}$ a function of its spectral radius instead of imposing a fixed allowable increment. By decreasing the allowable relative increment as convergence is neared, it would be possible to delay run termination until a more advanced stage of convergence. Such a stopping criterion was used by, e.g. Zijlema and Wesseling (1998). This criterion is adequate if the iteration process converges in a well-behaved manner and $\rho < 1$ for all iterations. However, due to nonlinear energy transfer in spectral space SWAN typically does not display such smooth behaviour. Therefore, this criterion may be less suited for SWAN.

An alternative way to evaluate the level of convergence is to consider the second derivative or curvature of the curve traced by the series of iterates (iteration curve). Since the curvature of the iteration curve must tend towards zero as convergence is reached, terminating the iteration process when a certain minimum curvature has been reached would be a robust break-off procedure. The curvature of the iteration curve of $H_{m0}$ may be expressed in the discrete sense as

$$\Delta(\Delta\tilde{H}_{m0}^s)^s = \tilde{H}_{m0}^s - 2\tilde{H}_{m0}^{s-1} + \tilde{H}_{m0}^{s-2}\,, \tag{3.25}$$

where $\tilde{H}_{m0}^s$ is some measure of the significant wave height at iteration level $s$. To eliminate the effect of small amplitude oscillations on the curvature measure, we define $\tilde{H}_{m0}^s \equiv (H_{m0}^s + H_{m0}^{s-1})/2$. The resulting curvature-based termination criterion at grid point $(i,j)$ is then

$$\frac{|H_{m0}^s(i,j) - (H_{m0}^{s-1}(i,j) + H_{m0}^{s-2}(i,j)) + H_{m0}^{s-3}(i,j)|}{2H_{m0}^s(i,j)} < \varepsilon_{\mathrm{C}}\,, \quad s = 3, 4, ...\,, \tag{3.26}$$

where $\varepsilon_{\mathrm{C}}$ is a given maximum allowable curvature. The curvature measure is made non-dimensional through normalization with $H_{m0}^s$. Condition (3.26) must be satisfied in at least 99% of all wet grid points before the iterative process stops. This curvature requirement is considered to be the primary criterion. However, the curvature passes through zero between local maxima and minima and, at convergence, the solution may oscillate between two constant levels due to the action density limiter (see Section 3.7.2), whereas the average curvature is zero. As safeguard against such a situation, the weaker criterion (3.22) is retained in addition to the stricter criterion (3.26).

Since version 41.01, the curvature-based stopping criteria, Eqs. (3.26) and (3.22) are the default, whereas the previous employed stopping criteria, Eqs. (3.22) and (3.23), are obsolete.

## 3.5 An illustrative explanation of the sweeping approach

In the absence of a current, the direction of propagation of the wave crest is equal to that of the wave energy. For this case, the propagation velocity of energy $(c_x, c_y)$ is equal to the group velocity $(c_{g,x}, c_{g,y})$. In presence of a current this is not the case, since the propagation velocities $c_x$ and $c_y$ of energy are changed by the current. Considering the applied numerical procedure in SWAN, it is initially more convenient to explain the basic principles of the numerical procedure in the absence of a current than in the situation where a current is present. So, first, we shall focus on the sweeping technique in the absence of a current. After this, we shall discuss the numerical procedure in case a current is present.

The computational region is a rectangle covered with a rectangular grid. One of the axes (say the $x-$axis) is chosen arbitrary, for instance perpendicular to the coast. The state in a grid point $(x_i, y_j)$ in an upwind stencil is determined by its up-wave grid points $(x_{i-1}, y_j)$ and $(x_i, y_{j-1})$. This stencil covers the propagation of action density within a sector of $0^o-90^o$, in the entire geographic space; see Figure 3.2. Hence, this procedure is called
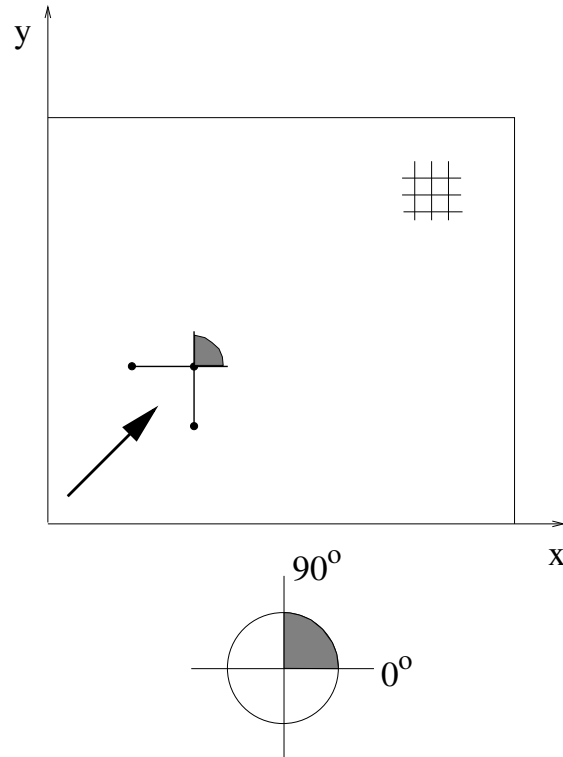
Figure 3.2: Numerical scheme for wave propagation in geographic space with below the first quadrant for which the waves are propagated.

sweep 1 and encloses all wave energy propagation over the first quadrant in spectral space.

This quandrant is the corresponding domain of dependence in the directional space. By rotating the stencil over $90^o$, the next quadrant $90^o - 180^o$ is propagated. Rotating the stencil twice more ensures propagation over all four quadrants (see Figure 3.1). This allows waves to propagate from all directions. Hence, the method is characterized as a four-sweep technique.

The gain of such a stencil is that the propagation is unconditionally stable because the wave characteristics lie within the concerning quadrant. Thus, propagation is not subjected to a CFL criterion. In addition, the principle of causality requires that the numerical domains of dependence of both geographic and spectral spaces must be identical.

In cases with bottom refraction or current refraction, action density can shift from one quadrant to another. This is taken into account in the model by repeating the computations with converging results (iterative four-sweep technique). Typically, we choose a change of less then 1% or so in significant wave height and mean wave period in all geographic grid points to terminate the iteration (see Section 3.4).

Note, however, we may even choose more sweeps than the proposed 4 ones[3]. The number of sweeps is denoted as $M$ and the directional interval of each sweep equals $360^o/M$. It is expected that the number of iterations may reduced, since the solution is guaranteed to be updated for all wave directions at all grid points in one series of sweeps, provided the directional interval is sufficiently small (e.g. 8 sweeps with an interval of $45^o$ each, or 12 sweeps of each $30^o$). This is certainly the case at deep water where wave rays are just straight lines. However, at shallow water, this becomes less obvious because of the presence of refraction. In this case the wave energy may jump multiple directional bins in one (large) time or distance step. It may leave a sweep sector too early or it may even skip this sweep, especially when the sweep interval is relatively small ($< 30^o$) and depth changes per grid cell are relatively large. The result is that wave rays erroneously cross and that a number of wave components in one sweep within one time/distance step overtakes some other bins in another sweep ahead, which implies that causality is violated, resulting in a possible model instability. See also Section 3.8.3. Hence, for such shallow water cases, choosing a relative large number of sweeps, $M > 4$, is more likely to prove counter-productive.

The numerical procedure as described above remains in principle the same when a current $(U_x, U_y)$ is present. The main difference is that the propagation velocities of energy are no longer equal to the group velocity of the waves but become equal to $c_x = c_{g,x} + U_x$ and $c_y = c_{g,y} + U_y$. To ensure an unconditionally stable propagation of action in geographical space in the presence of any current, it is first determined which spectral wave components of the spectrum can be propagated in one sweep. This implies that all wave components with $c_x > 0$ and $c_y > 0$ are propagated in the first sweep, components with $c_x < 0$ and $c_y > 0$ in the second sweep, components with $c_x < 0$ and $c_y < 0$ in the third sweep, and finally, components $c_x > 0$ and $c_y < 0$ in the fourth sweep. Since the group velocity of

---

[3]Although in SWAN the number of sweeps equals 4 and is hard-coded.

the waves decreases with increasing frequency, the higher frequencies are more influenced by the current. As a result, the sector boundaries in directional space for these higher frequencies change more compared to the sector boundaries for the lower frequencies. In general, four possible configurations do occur (see Figure 3.3). Consider, for instance, one fixed frequency propagating on a uniform current. The current propagates at an angle of $45^o$ with the $x-$axis. The sign of the current vector and strength of the current are arbitrary. The shaded sectors in Figure 3.3 indicate that all the wave components that are propagating in the direction within the shaded sector, are propagated in the first sweep ($c_x > 0$, $c_y > 0$).
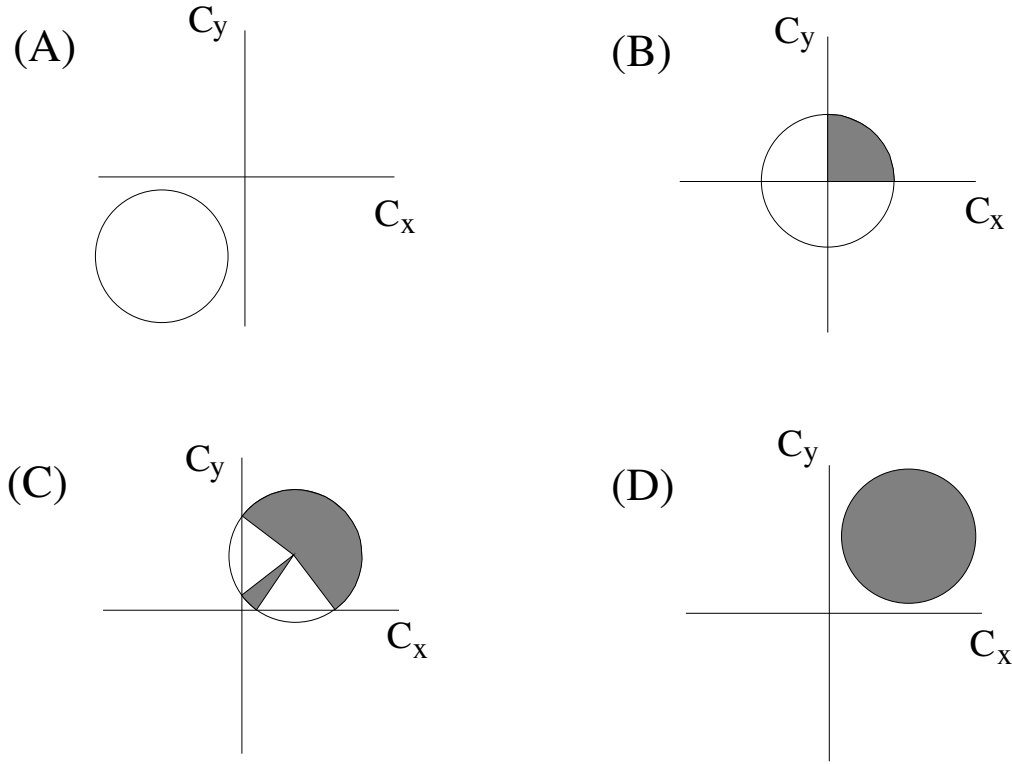


Figure 3.3: Four possible configurations and propagation velocities $c_x$, $c_y$ for a fixed frequency in the presence of a current propagating at an angle of $45^o$ with the $x-$axis.

The top-left panel (A) represents a situation in which both $c_x$ and $c_y$ are negative due to a strong opposing current, i.e. wave blocking occurs. None of the wave components is propagated within the first sweep. The top-right panel (B) represents a situation in which the current velocity is rather small. The sector boundaries in directional space are hardly changed by the current such that the sector boundaries are approximately the same as in the absence of a current. The bottom-left panel (C) reflects a following current that causes the propagation velocities of the wave components in two sectors to be larger than zero. In this specific case, all the waves of the shaded sectors are propagated within the first sweep. The bottom-right panel (D) represents a case with a strong following current for which all

the action is take along with the current. For this case the fully $360^o$ sector is propagated in the first sweep.

After it has been determined which wave components are propagated in one sweep, i.e., the sector boundaries in directional space have been determined for each frequency, the integration in frequency and directional space can be carried out for those wave components.

# 3.6   Implementation of DIA within the four-sweep technique

In SWAN, the quadruplets are integrated using the DIA, see Section 2.3.4. As a consequence of the four-sweep technique, two different types of methods can be used to calculate the four wave-wave interactions.

1. The first method implies that the interactions are calculated in every iteration prior to the first sweep. This method ensures conservation of energy density, but has the disadvantage that the spectral source term $S_{\mathrm{nl4}}(\sigma, \theta)$ for every grid point in geographical space has to be stored in internal memory. Such an integration method increases the amount of required memory with a factor about 2. The source term is stored in memory and is then explicitly integrated for a particular sweep. This method is particularly useful when ambient current is included.

2. The second method is slightly different, in which the interactions are calculated and integrated for every sweep separately. The calculation of the energy transfer for a specific quadrant requires also the calculation of the transfer within a sector of about $33^o$ in the adjacent two quadrants. Calculating the interactions for one sweep increases the computation time for the quadruplets with a factor of about 1.66 (2 adjacent sectors of $33^o$ times 4 sweeps divided by $360^o$). Contrary to the first method, the total rate of this energy shift is not stored in memory so that energy density is not conserved per sweep (and per iteration). However, this does not influence the converging results. Within this second method, two different numerical schemes are available, namely, a semi-implicit scheme and a fully explicit scheme. The use of a fully explicit scheme is recommended because of the computational efficiency. A semi-implicit scheme increases the computation time of the quadruplets with a factor of about 2. Note that this method does not work when ambient current is included in the model. The reason is that the bounds of the directional sector within a sweep may not be the same for every frequency bin. So there may be some overlap of frequency bins between the quadrants, and so this method does not conserve energy anymore. To prevent this the user is advised to choose the first method.

# 3.7 Action density limiter and under-relaxation

## 3.7.1 Introduction

The accuracy with which physical processes for wave growth are approximated numerically is of crucial importance in assessing the predictive realism of spectral wave models. There is a need to separate these numerical errors from errors due to physical modelling. Third-generation wave models pose a numerical difficulty caused by the presence of multiple time scales. This is a reflection of the physical nature of wind waves, which consist of a wide range of frequencies. The ratio of the largest to the smallest time scale of spectral components is often substantially larger than one. When this is the case, the action balance equation is called stiff (Press *et al.*, 1993)[4]. Taking proper account of these time scales is a necessary condition for numerical accuracy. This would require the use of a very small time step in a numerical algorithm, which may be impractical. Moreover, the action balance equation is usually so stiff that its numerical implementation combined with economically large time steps often prevent a stable solution. In this respect, nonlinear four-wave interaction usually poses the biggest problem, since this process is associated with high sensitivity to spectral change.

In a number of papers concerning spectral wave computation, numerical measures are proposed to achieve stable model results economically. WAMDI Group (1988) suggest to use a semi-implicit time integration scheme with a time step that matches the time scale of low-frequency waves. However, numerically stable solution of the resulting sytem of equations can not be guaranteed (Hargreaves and Annan, 2001). The ratio of the largest eigenvalue to the smallest eigenvalue of the stiff system of equations, called the condition number, can be so large that even a fully-implicit method combined with large time steps precludes a stable solution. For counterexamples, see Hargreaves and Annan (2001). The only remedy is time step reduction or under-relaxation so that the modified system of equations has a spectrum of eigenvalues with a more favourable condition number.

To guarantee numerical stability at relatively large time steps, the so-called action density limiter has been introduced in WAM in the early 1980's (Hersbach and Janssen, 1999). This limiter restricts the rate of change of the energy spectrum at each time step. Because low-frequency waves carry the most energy, it is desirable to solve the balance equation in this part of the spectrum accurately without intervention by the limiter, whereas for high-frequency waves using an equilibrium level is sufficient. Although this approach lacks a rigorous foundation and is not generally applicable or valid, it appears to guarantee numerical stability at relatively large time steps even when these do not match the time scales of wave growth. Moreover, it is believed that the limiter will not affect the stationary solution when convergence is reached. This assumption is widely employed as a justification for the use of limiters. For an overview, we refer to Hersbach and Janssen (1999) and Tolman (2002) and the references quoted therein. Tolman (1992) proposes an alternative to the

---

[4]The equivalent situation for such an equation is to have eigenvalues of very different magnitudes.

action density limiter in which the time step is dynamically adjusted where necessary to ensure accurate wave evolution. The calculation of this optimal time step is related to the action density limiter. Further details can be found in Tolman (1992, 2002). .

The steady-state solution in the SWAN model is obtained in an iterative manner, which can be regarded as a time marching method with a pseudo time step. This pseudo time step generally does not match the relatively small time scale in frequency space and consequently, divergence will occur. Therefore, SWAN makes use of the action density limiter to stabilize the iteration process (Booij *et al.*, 1999). However, experience with SWAN has revealed that the limiter acts not only in the equilibrium space, but also in the energy-containing part of the wave spectrum. This finding is also confirmed by Tolman (2002). Furthermore, the limiter appears to be active over almost all spectra in the geographical domain and during the entire iteration process. This activity has been associated with poor convergence behaviour, such as small-amplitude oscillation in frequency space. Ris (1999) demonstrated that stationary SWAN results are influenced by the settings of the action limiter while De Waal (2001) suspects that the limiter acts as a hidden sink in the source term balance under equilibrium conditions. The question to what extent this limiter adversely affects the stationary solution of SWAN has not been addressed previously, and is considered here.

An alternative way to restrict the high rate of change at higher frequencies is under-relaxation, i.e. making smaller updates by means of a much smaller (pseudo) time step (Ferziger and Perić, 1999). Consequently, a limiter may no longer be needed. Although this approach may be suitable to SWAN, it slows down convergence significantly. Here, we propose a new method that finds a compromise between fast convergence on the one hand and minimizing the role of the limiter in the energetic part of the spectrum on the other. The key idea to achieve this is to link the extent of updating to the wave frequency - the larger the frequency, the smaller the update. This approach is therefore called frequency-dependent under-relaxation.

## 3.7.2   Convergence-enhancing measures

As explained in Section 3.7.1, many time scales are involved in the evolution of wind waves. The high-frequency waves have much shorter time scales than the low-frequency waves, rendering the system of equations (3.20) stiff. If no special measures are taken, the need to resolve high-frequency waves at very short time scales would result in extreme computational time. For economy, it is desirable that a numerical technique can be used with a large, fixed time step. Moreover, we are mainly interested in the evolution of slowly changing low-frequency waves. For stationary problems, we are interested in obtaining the steady-state solution. Unfortunately, the convergence to the steady state is dominated by the smallest time scale and, in the absence of remedial measures, destabilizing over- and undershoots will prevent solution from converging monotonically during the iteration process. These oscillations arise because of the off-diagonal terms in matrix $A$, which can

be dominant over the main diagonal, particularly when the ratio $\sigma_{\max}/\sigma_{\min}$ is substantially larger than one. As a consequence, convergence is slowed down and divergence often occurs. To accelerate the iteration process without generating instabilities, appropriately small updates must be made to the level of action density.

With the development of the WAM model, a so-called action density limiter was introduced as a remedy to the abovementioned problem. This action limiter restricts the net growth or decay of action density to a maximum change at each geographic grid point and spectral bin per time step. This maximum change corresponds to a fraction of the omni-directional Phillips equilibrium level (Hersbach and Janssen, 1999). In the context of SWAN (Booij *et al.*, 1999), this is

$$\Delta N \equiv \gamma \, \frac{\alpha_{\mathrm{PM}}}{2\sigma k^3 c_g} \,, \tag{3.27}$$

where $\gamma \geq 0$ denotes the limitation factor, $k$ is the wave number and $\alpha_{\mathrm{PM}} = 8.1 \times 10^{-3}$ is the Phillips constant for a Pierson-Moskowitz spectrum (Komen *et al.*, 1994). Usually, $\gamma = 0.1$ (Tolman, 1992)[5]. Note that when the physical wind formulation of Janssen (1989,1991a) is applied in SWAN, the original limiter of Hersbach and Janssen (1999) is employed. Denoting the total change in $N_{i,j,l,m}$ from one iteration to the next after Eq. (3.2) by $\Delta N_{i,j,l,m}$, the action density at the new iteration level is given by

$$N_{i,j,l,m}^s = N_{i,j,l,m}^{s-1} + \frac{\Delta N_{i,j,l,m}}{|\Delta N_{i,j,l,m}|} \, \min\{|\Delta N_{i,j,l,m}|, \Delta N\} \,. \tag{3.28}$$

For wave components at relatively low frequencies, Eq. (3.28) yields the pre-limitation outcome of Eq. (3.2), because, for these components, the pseudo time step matches the time scale of their evolution. For high-frequency waves, however, Eq. (3.28) gives the upper limit for the spectrum to change per iteration due to the limiter, Eq. (3.27). For typical coastal engineering applications, it is sufficient to compute the energy-containing part of the wave spectrum accurately. In other words, action densities near and below the spectral peak should not be imposed by the limiter (3.27). However, our experiences with SWAN have shown that the limiter is active even close to the peak. Furthermore, during the entire iteration process, the limiter is typically active at almost every geographic grid point.

The alternative measure to enhance the convergence of the stable iteration process considered here is so-called false time stepping (Ferziger and Perić, 1999). Under-relaxation terms representing the rate of change are introduced to enhance the main diagonal of $A$ and thus stabilize the iteration process. The system of equations (3.20) is replaced by the following, iteration-dependent system

$$\frac{\vec{N}^s - \vec{N}^{s-1}}{\tau} + A\,\vec{N}^s = \vec{b} \tag{3.29}$$

---

[5]It is noted here that the effective $\gamma$ used in SWAN is not equivalent to that of WAM: the former is a factor $2\pi$ larger.

with $\tau$ a pseudo time step. The first term of Eq. (3.29) controls the rate of convergence of the iteration process in the sense that smaller updates are made due to decreasing $\tau$, usually at the cost of increased computational time. To deal with decreasing time scales at increasing wave frequency, the amount of under-relaxation is enlarged in proportion to frequency. This allows a decrease in the computational cost of under-relaxation, because at lower frequencies larger updates are made. This frequency-dependent under-relaxation can be achieved by setting $\tau^{-1} = \alpha\sigma$, where $\alpha$ is a dimensionless parameter. The parameter $\alpha$ will play an important role in determining the convergence rate and stability of the iteration process. Substitution in Eq. (3.29) gives

$$(A + \alpha\sigma I)\,\vec{N}^s = \vec{b} + \alpha\sigma\vec{N}^{s-1}\,. \tag{3.30}$$

When the steady state is reached (i.e. $s \to \infty$), system (3.30) solves $A\,\vec{N}^\infty = \vec{b}$ since, $\vec{N}^\infty$ is a fixed point of (3.30).

Suitable values for $\alpha$ must be determined empirically and thus robustness is impaired. For increasing values of $\alpha$, the change in action density per iteration will decrease in the whole spectrum. The consequence of this is twofold. Firstly, it allows a much broader frequency range in which the action balance equation (3.2) is actually solved without distorting convergence properties. Secondly, the use of the limiter will be reduced because more density changes will not exceed the maximum change due to Eq. (3.27). Clearly, this effect may be augmented by increasing the value of $\gamma$ in Eq. (3.27).

To allow proper calculation of the second-generation first guess of the wave field (see Section 3.3), under-relaxation is temporarily disabled ($\alpha = 0$) during the first iteration. Whereas this measure is important in achieving fast convergence, it does not affect stability, since the second-generation formulations do not require stabilization.

## 3.8   On the approximation of refraction in large-scale SWAN applications

### 3.8.1   Introduction

In some large-scale applications SWAN is known to produce seemingly unstable results. One of the causes is the coarseness of the grid − usually the unstructured one. This issue will be dealt with in Section 3.8.5. Another cause is the fully implicit treatment of the refraction term when dealing with non-stationary runs. Implicit schemes allow propagation of wave energy using a large time step. In this treatment the value of $c_\theta$ is determined at the point where the action density is to be updated. If this value does vary too much over one time step, causality may not be preserved. Usually, this is not the case in small scale coastal applications.

In large scale oceanic applications, however, the depth may vary from one grid point to

the next by a factor of over 10 (e.g. in presence of seamounts). Then the value of $c_\theta$ at the shallowest grid point is not representative anymore of the interval between the two grid points, and it is justified to limit the value to one that is representative. The problem now is to find a limitation which on the one hand guarantees smooth behaviour in large-scale applications and which has no influence on small-scale applications. This will be elaborated in Section 3.8.3.

Related to the aforementioned problems we first elaborate the consequences of *the law of constant energy flux along the wave ray* (Whitham, 1974) in the next section.

## 3.8.2    Energy transport along wave rays

In this section we focus on the following transport processes: shoaling and refraction. Calculating the wave shoaling and refraction effects is necessary to predict accurately *shallow water* wave conditions, either in the surf zone, across the main channels in estuaries, or across the seamounts. Throughout this section we assume the absence of the non-conservative source/sink terms, such as wind input, nonlinear wave-wave interactions and energy dissipation. The governing equation is the following wave energy balance (ambient current is not included)

$$\frac{\partial E}{\partial t} + \nabla_{\vec{x}} \cdot (\vec{c}_g E) + \frac{\partial c_\theta E}{\partial \theta} = 0 \tag{3.31}$$

Eq. (3.31) is linear and strict hyperbolic with nonlinear coefficients, whereas its characteristics (trajectories) in the $(\vec{x}, \theta)-$space are generally not straight lines due to a varying seabed topography. Along the characteristics the wave energy fluxes $\vec{c}_g E$ and $c_\theta E$ are constant (Whitham, 1974).

We may rewrite Eq. (3.31) in a characteristic form, as follows

$$\frac{dE}{dt} = -\left(\nabla_{\vec{x}} \cdot \vec{c}_g + \frac{\partial c_\theta}{\partial \theta}\right) E \tag{3.32}$$

with the total derivative of $E$ defined as

$$\frac{dE}{dt} \equiv \frac{\partial E}{\partial t} + \vec{c}_g \cdot \nabla_{\vec{x}} E + c_\theta \frac{\partial E}{\partial \theta} \tag{3.33}$$

along a trajectory of energy propagation with slopes

$$\frac{d\vec{x}}{dt} = \vec{c}_g = (c_{g,x}, c_{g,y}), \quad \frac{d\theta}{dt} = c_\theta$$

Let us consider a stationary wave characteristic with slope

$$\frac{d\vec{x}}{d\theta} = \frac{\vec{c}_g}{c_\theta} \tag{3.34}$$

If there is no change in the seabed along the wave ray, the group velocity is constant. In addition, if there is no depth variation along the wave crest, then the turning rate is zero. Hence, the characteristic (3.34) in the $(\vec{x}, \theta)-$space is in this case the direction of propagation (with group velocity). By virtue of Eq. (3.32), the total energy $E$ is thus constant along the same characteristic. However, due to depth variations, wave energy will either increase or decrease along its curved characteristic.

The right hand side of Eq. (3.32) can be considered either as a source term or a sink term. This depends on the gradients of the group velocity and turning rate along the wave ray and wave crest, respectively. The rate at which the energy in- or decreases is related to the relaxation time $\tau$, which is the typical time scale for wave energy transport to reach steady state after being disturbed. It is given by

$$\tau^{-1} = \left| \nabla_{\vec{x}} \cdot \vec{c}_g + \frac{\partial c_\theta}{\partial \theta} \right|$$

The importance of this relaxation time relates to the choice of discretization steps for the purpose of *accurate* integration of Eq. (3.32). In this respect, the numerical accuracy with respect to the change in wave energy from one step to the next along the characteristic, viz. Eq (3.33), is determined by the time step, grid size, and directional bin size (see Section 3.8.3). The associated step size is denoted as $\Delta T$. Causality requires that wave energy propagates in the right direction along its characteristic, and at the right speed. For example, causality problem can be present in an implicit scheme that propagates wave energy across a large distance using a large time step. In other words, if this time step is too large, some wave components getting ahead of themselves and leaving behind some other components ahead. To prevent this, temporal, spatial and directional changes in the numerical and exact solutions must go hand in hand. This implies that $\Delta T < \tau$. Hence, a sufficient condition for accurate integration reads

$$\left| \nabla_{\vec{x}} \cdot \vec{c}_g + \frac{\partial c_\theta}{\partial \theta} \right| \Delta T < 1 \tag{3.35}$$

This condition resembles the Lipschitz criterion[6] and is generally less severe than the traditional CFL criterion for numerical stability. We may rewrite Eq. (3.35) in Cartesian coordinates as

$$\left| \frac{\partial c_{g,x}}{\partial x} + \frac{\partial c_{g,y}}{\partial y} - \frac{|\vec{c}_g|}{k} \left( \frac{\partial k}{\partial x} \cos\theta + \frac{\partial k}{\partial y} \sin\theta \right) \right| \Delta T < 1$$

with $k = |\vec{k}|$ the length of the wave number vector (cf. Eq. (2.14)). This criterion implies that at locations with relatively large bottom slopes, the step size $\Delta T$ must reduce locally to prevent inaccuracies. This step size is determined by the temporal, spatial and directional

---

[6]The Lipschitz criterion is well known in the field of semi-Lagrangian schemes and its interpretation is that trajectories do not cross each other during one Lagrangian time step. See e.g. Smolarkiewicz and Pudykiewicz (1992) and Lin and Rood (1996).

resolutions. In this regard, the interpretation of the Lipschitz criterion (3.35) is that the *maximum* step size is determined by the numerical accuracy rather than by the numerical stability. This accuracy aspect is related to the curvature of the wave propagation field (due to change in wave direction over a certain distance) at the grid and time resolutions applied.

In shallower water, medium variations can be significant, i.e. changes in seabed and mean current can be large within a few wave lengths, whereas ocean waves feature coherent structures such as refraction over topography and currents. Therefore, one must choose a geographical grid size proportional to the resolution of the bathymetry capturing its local features. For instance, near the coast and in the surf zone, a typical grid size of $20 - 50$ m is not uncommon in SWAN applications. An important assumption made in this consideration is that the transport velocities $\vec{c}_g$ and $c_\theta$ do not much vary over a grid size, so that Lipschitz criterion (3.35) is most likely met. This is reasonable as the wave characteristics are more or less non-curved lines (during the elapsed time step), because the propagation in the $(\vec{x}, \theta)-$space is slowly time varying. This is generally true in coastal applications.

In the open ocean, it is assumed that seabed topography is slowly varying in space so that the directionally spread wave field is rather spatially homogeneous. As such, refraction effects can be regarded as weak. The grid resolution is usually determined by the resolution for the wind field that generates the waves locally, which is often much coarser than the bottom resolution. For example, for oceanic waters, the employed grid size is typically $10 - 50$ km. However, there are exceptions. An example are the seamounts in the deeper parts of the open ocean. At such locations, the depth may vary from one grid point to the next by a factor of 10 or so or even more. In such a case, the value of the turning rate $c_\theta$ at the shallowest grid point is not representative anymore with respect to the distance between the two considered grid points. Hence, criterion (3.35) is violated, and computed spectral wave components will simply turn too much and jump multiple directional bins in one distance step. The result is that a number of wave components in one sweep within one distance step overtakes some other bins in another sweep ahead, which implies that causality is violated, resulting in a possible model instability. To circumvent this we must refine the computational grid locally to resolve the local bathymetric features, and the Lipschitz criterion (3.35) can be helpful in this. The consequences will be discussed in the following section.

### 3.8.3   The problem with refraction in non-stationary applications

In this section we discuss how refraction affects the accuracy of the discretization of the total derivative of wave energy along a non-curved wave ray. Initially, the energy is uniformly distributed over the wave directions. Under these conditions, we reconsider Eq. (3.32),

$$\frac{dE}{dt} = -\frac{\partial c_\theta}{\partial \theta} E$$

and we examine the discretization of the following total derivative of the energy density

$$\frac{dE}{dt} = \frac{\partial E}{\partial t} + c_x \frac{\partial E}{\partial x} + c_y \frac{\partial E}{\partial y} \tag{3.36}$$

with $(c_x, c_y) = \vec{c}_g$ the propagation velocity vector in the geographical space. This total derivative indicates that the time rate of change in energy is computed along the wave characteristics defined by the following ODEs

$$\frac{dx}{dt} = c_x, \quad \frac{dy}{dt} = c_y.$$

For the purpose of illustration the spatial derivatives are replaced by first order upwind differences. If we assume $c_x$ and $c_y$ positive during the first sweep, see Figure 3.4, then the
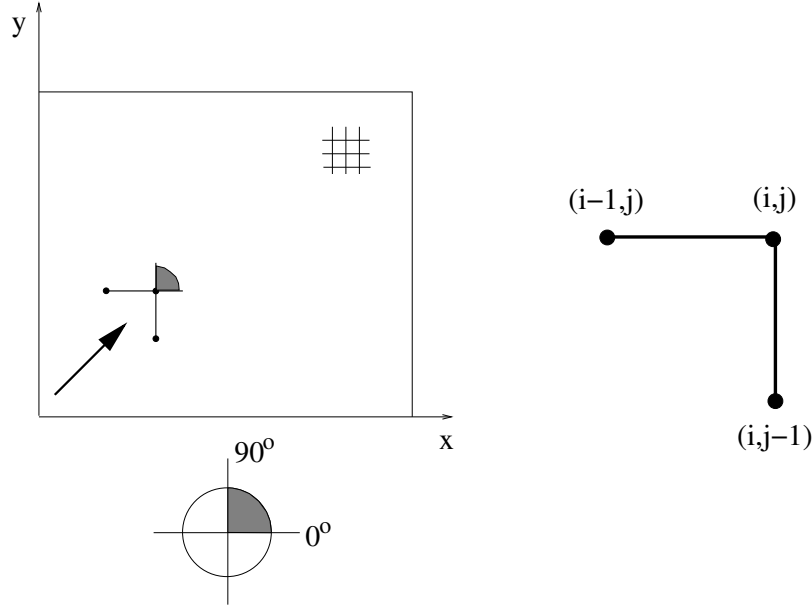


Figure 3.4: Numerical scheme for wave propagation in geographic space with below the first quadrant for which the waves are propagated, and right the stencil.

approximation of Eq. (3.36) is as follows

$$\frac{E_{i,j}^n - E_{i,j}^{n-1}}{\Delta t} + c_x \frac{E_{i,j}^n - E_{i-1,j}^n}{\Delta x} + c_y \frac{E_{i,j}^n - E_{i,j-1}^n}{\Delta y}.$$

Note that the time integration is based on the first order implicit Euler scheme. Furthermore, $\Delta t$ is the time step, and $\Delta x$ and $\Delta y$ are the mesh spaces. This approximation can be viewed as the well-known semi-Lagrangian approximation, which is rewritten as

$$\left( \frac{1}{\Delta t} + \frac{c_x}{\Delta x} + \frac{c_y}{\Delta y} \right) E_{i,j}^n - \frac{1}{\Delta t} E_{i,j}^{n-1} - \frac{c_x}{\Delta x} E_{i-1,j}^n - \frac{c_y}{\Delta y} E_{i,j-1}^n$$

which is, in turn, interpreted as an approximation of the total derivative, Eq. (3.36), as follows

$$\frac{E_{i,j}^n - E_{i^*,j^*}^{n-1}}{\Delta T} \tag{3.37}$$

with

$$i^* = i - p, \quad j^* = j - q, \quad p = \frac{c_x \Delta T}{\Delta x}, \quad q = \frac{c_y \Delta T}{\Delta y}.$$

Note that $p$ and $q$ are the Courant numbers. They are not integers, and therefore $(i^*, j^*)$ is not a grid point. This point, however, lies on the wave characteristic. The quantity $E_{i^*,j^*}^{n-1}$ can be interpreted as the value of $E$ at time $t^{n-1}$ in $(i^*, j^*)$ which is being convected in $(i, j)$ in a lapsed time $\Delta T$. This value is simply obtained from the interpolation of the surrounding values $E_{i,j}^{n-1}$, $E_{i,j}^n$, $E_{i-1,j}^n$ and $E_{i,j-1}^n$ in the $(t, x, y)-$plane. In this case, there is no restriction on time step $\Delta t$ as the characteristic lies inside the computational stencil. Note that the lapsed time $\Delta T$ is a function of time step $\Delta t$ and grid sizes $\Delta x$ and $\Delta y$, and is called the Lagrangian time step, which should not be confused with the Eulerian time step $\Delta t$. Generally, $\Delta T < \Delta t$.

Causality requires that wave energy being refracted from one directional bin to another further down must pass through all the bins along a wave crest between them. Hence, for an accurate time integration along the wave characteristic, viz. Eq. (3.37), we must employ the Lipschitz criterion (3.35). In the present context, this criterion reads

$$|\frac{\partial c_\theta}{\partial \theta}| \Delta T < 1$$

which ensures that wave energy propagate from a bin to the adjacent one during one time step $\Delta T$. Thus, for physical consistency, a restriction on the time step must be imposed in order for the wave directions not to cross each other and the boundaries of a quadrant in the spectral space. Specifically, the Courant number based on $\Delta T$ and $\Delta \theta$ (i.e. directional bin) must be less than unity, that is,

$$\text{Cr} \equiv \frac{|c_\theta| \Delta T}{\Delta \theta} < 1 \tag{3.38}$$

with $c_\theta$ the turning rate[7]. This condition is a sufficient one and implies the Lipschitz criterion.

A violation of this criterion implies that the energy can travel in one time or distance step over a number of directional bins or more than the length of one sweep (which in the absence of a current is $90^o$, see Figure 3.4). For example, consider the first sweep, see Figure 3.4, the boundaries of the first quadrant are the lines $0^o$ and $90^o$. Next, we consider the directional sector in the spectral space associated with the considered sweep, see Figure 3.5. We shall show that condition, Eq. (3.38), is sufficient to assure that

---

[7]The spatial turning rate is the change in wave direction per unit forward distance $\ell$ that is travelled by the wave energy in a time interval $\ell/c_g$, and thus represents the curvature of the wave ray. This is equivalent to $c_\theta$, which is the turning rate of the wave direction per unit time.
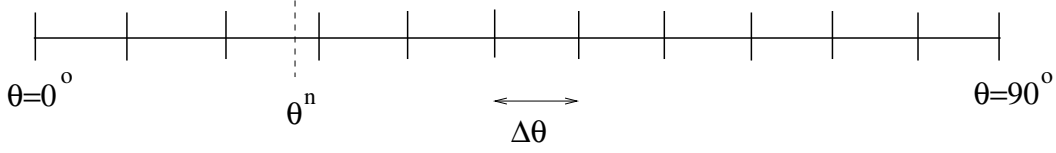
Chapter 3



Figure 3.5: Directional sector associated with the first sweep.

1) during $\Delta T$ the distance travelled in $\theta-$direction is at most $\Delta\theta$ and 2) wave energy propagating in any bin in $\theta-$direction will not cross the boundaries of the directional sector, except for the first and last bins. Hence, this prevents wave rays from intersecting each other. Note that we implicitly assume that the net change in mean wave direction within the distance covered during $\Delta T$ is less than the directional resolution. Since, by definition,

$$\frac{d\theta}{dt} = c_\theta \,,$$

we may approximate this, as follows,

$$\theta^n \approx \theta^{n-1} + c_\theta \Delta T \,. \tag{3.39}$$

For a given $n-1$, we choose an arbitrary point, $\theta^{n-1}$, inside the directional sector; see Figure 3.5. If $\theta^{n-1} > \Delta\theta$ then, Eqs. (3.39) and (3.38) imply $|\theta^n - \theta^{n-1}| < \Delta\theta$, and hence the chosen point at next time step, $\theta^n$, still lies inside the directional sector. If $\theta^{n-1} < \Delta\theta$, i.e. in the first bin, then one obtains

$$\theta^n = \theta^{n-1} + \frac{\Delta T}{\Delta\theta}\left[(1-\theta^{n-1})c_\theta(\theta=0^o) + \theta^{n-1}c_\theta(\theta=\Delta\theta)\right]$$

or

$$\theta^n = \theta^{n-1}\left(1 - \frac{\Delta T}{\Delta\theta}c_\theta(\theta=0^o)\right) + \frac{\Delta T}{\Delta\theta}c_\theta(\theta=0^o) + \frac{\Delta T}{\Delta\theta}\theta^{n-1}c_\theta(\theta=\Delta\theta)\,.$$

If $c_\theta(\theta=0^o) > 0$ and $c_\theta(\theta=\Delta\theta) > 0$ then, the point at next step will be keep inside the directional sector, if Eq. (3.38) holds. In other cases the energy is leaving through boundary $\theta = 0^o$, though the change in direction is limited to the adjacent directional bin of the other quadrant. This holds also for the last bin and the corresponding right boundary $\theta = 90^o$.

Note that Eq. (3.38) is not required for the stability of the method but contributes to improve its physical accuracy, so that the principle of causality is obeyed. For instance, in a large-scale application, one often applies coarse (nested) grids with a desired time step. Both the mesh width and the time step might be too large to represent wave refraction appropriately. This is readily seen as follows. We consider stationary, long-crested waves in $(x,\theta)-$space, propagating at an angle with the positive $x-$axis. There is a bottom gradient along this axis so that refraction is present. There are no currents. The associated characteristic or wave ray is given by $d\theta/dx = c_\theta/c_g$. This is the *spatial* turning rate, i.e.

the change in wave direction per unit forward distance. Hence, the directional turn of the wave crest over a distance $\Delta x$ is given by

$$\frac{c_\theta}{c_g}\,\Delta x$$

and the Courant number becomes (cf. Eq. (3.38))

$$\mathrm{Cr} = \frac{|c_\theta|}{c_g}\frac{\Delta x}{\Delta\theta}$$

which must be smaller than unity to prevent crossing of wave rays. The turning rate of the wave direction per unit time is given by

$$c_\theta = -\frac{1}{k}\frac{\partial\sigma}{\partial h}\frac{\partial h}{\partial m}\,, \tag{3.40}$$

where $k$ is the wave number, $\sigma$ is the frequency, $h$ is the water depth and $m$ is the coordinate along the wave crest (i.e. orthogonal to the propagation direction). On a coarse grid, the depth difference in two adjacent grid points $\Delta h$, and thereby $c_\theta$, can be very large, especially for low-frequency components in very shallow water (see also Section 3.8.5). This implies that the Lipschitz condition may be violated, i.e. $\mathrm{Cr} \geq 1$.

Complying with the Lipschitz criterion (3.38) simply prevents wave energy to jump over a number of directional bins, where this energy would go way beyond some other bins ahead. This was demonstrated to be a useful criterion with respect to the behavior of refraction when the bathymetry is poorly resolved by the model. As the refraction becomes excessive in a region with steep bottom gradients, it is possible that the wave rays falsely cross and that the wave energy focus toward a single grid point, creating unrealistically large wave heights and long periods; see Dietrich et al. (2013).

Yet the value of $c_\theta$ in the shallowest grid point can be simply too large due to a large difference in bottom levels over one mesh width, so that wave energy will change direction over more than some directional bins or even the directional sector, so that wave rays falsely intersect each other. To prevent this artefact a limitation on $c_\theta$ seems to be justified. Recalling Eq. (3.38), a limitation would be

$$|c_\theta| < \frac{\Delta\theta}{\Delta T}\,.$$

We estimate the reciprocal of the elapsed time $\Delta T$ as a fraction of

$$\frac{1}{\Delta t} + \frac{c_x}{\Delta x} + \frac{c_y}{\Delta y}$$

and so,

$$|c_\theta| \leq \alpha_\theta\Delta\theta\left(\frac{1}{\Delta t} + \frac{|c_x|}{\Delta x} + \frac{|c_y|}{\Delta y}\right)$$

with $\alpha_\theta$ a user-defined maximum Courant number, which is generally smaller than 1. (In SWAN, the default value is $\alpha_\theta = 0.9$.) Often the desired time step $\Delta t$ is such that the first term between brackets can be safely neglected. This implies a slightly more restriction on the turning rate and, in turn, a safety margin in the CFL condition, as follows

$$|c_\theta| \leq \alpha_\theta \Delta \theta \left( \frac{|c_x|}{\Delta x} + \frac{|c_y|}{\Delta y} \right) . \tag{3.41}$$

It must be stressed that this limitation may affect the solution locally depending on $\alpha_\theta$. In fact, we need to find a good estimate for $c_\theta$ which solely depends on $\alpha_\theta$. However, it is unlikely that this measure affects the solution nearshore or on fine grids, since the turning rate will not too much vary over one (spatial) step. This is an *effective* survival measure in the sense that it prevents the excessive refraction without deteriorating the solution elsewhere.

### 3.8.4   A historical overview of limitation on $c_\theta$

The problem with refraction showing some inaccurate results has been known for a long time. This issue had received some attention by Nico Booij for the first time in November 1998. His basic idea to fix this problem is as follows. We consider a case with parallel depth contours within one sector, see Figure 3.6. We assume that grid point $(i, j)$ is in
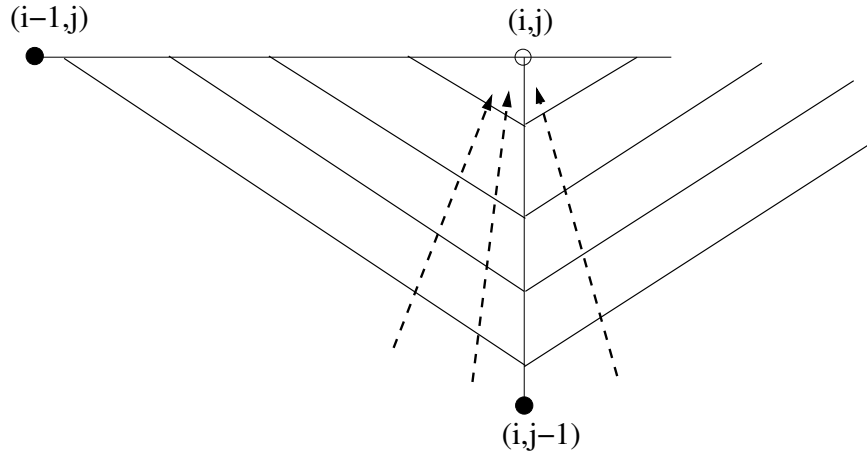


Figure 3.6: Geographic grid with parallel depth contours.

shallow water. The other two grid points $(i - 1, j)$ and $(i, j - 1)$ are in deeper water. Let $n$ be the coordinate along the wave rays. Then according to Snel's law (Holthuijsen, 2007, NOTE 7A, pg. 207), we have

$$\frac{d\theta}{dn} = \frac{1}{c} \frac{dc}{dn} \tan \theta .$$

Here $\theta$ will be of the order of $45^o$. So, we get

$$\frac{d\theta}{dn} = \frac{1}{c} \frac{dc}{dn} .$$

The slope at grid point $(i, j)$ determines the value of $d\theta/dn$. In shallow water, $c = \sqrt{gh}$, so

$$\frac{d\theta}{dn} = \frac{1}{2h}\frac{dh}{dn} \, .$$

This may be approximated as follows

$$\frac{d\theta}{dn} \approx \frac{1}{2h_{i,j}}\frac{h_* - h_{i,j}}{\Delta n}$$

with $h_*$ the water depth in one of the neighbouring grid points $(i-1, j)$ and $(i, j-1)$. In the numerical procedure $d\theta/dn$ is constant over a spatial step, so the change in direction over a step is

$$\frac{d\theta}{dn}\Delta n = \frac{h_* - h_{i,j}}{2h_{i,j}} \, .$$

In order to maintain stability the change of direction must remain below $90^o$. Consequently, we obtain

$$h_* - h_{i,j} \leq \pi h_{i,j} \, .$$

In the program the factor $\pi$ is replaced by a user-determined factor $\beta$. Hence, the depths in surrounding grid points are reduced to $\beta h_{i,j}$, if they are larger than this value. It should be noted that this approach was outlined in an unpublished note. Our experience with this approach is that it seems not effective enough.

## 3.8.5 The problem with refraction on coarse grids

Another issue is the accuracy with which the turning rate is computed on coarse grids. In SWAN this turning rate is computed as follows (see also Eq. (3.40))

$$c_\theta = \frac{\sigma}{\sinh 2kh}\left(\frac{\partial h}{\partial x}\sin\theta - \frac{\partial h}{\partial y}\cos\theta\right) \tag{3.42}$$

Here, wave refraction can only be caused by depth variation. As an alternative, the turning rate can be formulated in terms of phase velocity as follows (see Holthuijsen, 2007, pg. 210)

$$c_\theta = -\frac{c_g}{c}\frac{\partial c}{\partial m}$$

or

$$c_\theta = \frac{c_g}{c}\left(\frac{\partial c}{\partial x}\sin\theta - \frac{\partial c}{\partial y}\cos\theta\right) \tag{3.43}$$

An advantage of this formula is that refraction due to mud (non-rigid seafloor) can be included, which is implemented in SWAN version 41.01. Although these formulas are identical, they differ in result due to numerics. The first one, Eq. (3.42), seems to be rather inaccurate at relative coarse grids with steep bottom slopes. Experiments suggested that Eq. (3.43) with coarse resolution yields results that are similar to those using Eq.

(3.43) or Eq. (3.42) with high resolution. By contrast, approximation based on Eq. (3.42) with coarse resolution yields considerably different − often inaccurate − result. Therefore, Eq. (3.42) is replaced by Eq. (3.43) since version 41.01AB.

Till version 41.01A, the derivative $\partial h/\partial x$ or $\partial c/\partial x$ has been approximated using a first order backward difference scheme, for both structured and unstructured grids,

$$\frac{\partial c}{\partial x} \approx \frac{c_{i,j} - c_{i-1,j}}{\Delta x}$$

see Figure 3.4 for the used stencil. Note that grid point $(i,j)$ is the shallowest one. This approximation appeared to be rather inaccurate at coarse grids as well. Moreover, it can also lead to non-physical asymmetry in turning rate, and therefore wave energy. Therefore, since version 41.01AB, second order central differences are applied as follows

$$\frac{\partial c}{\partial x} \approx \frac{c_{i+1,j} - c_{i-1,j}}{2\Delta x}$$

Hence, the refraction velocity, Eq. (3.43), is approximated in SWAN, using structured grids, as follows

$$c_{\theta i,j} = \frac{c_{g i,j}}{c_{i,j}} \left( \frac{c_{i+1,j} - c_{i-1,j}}{2\Delta x} \sin\theta - \frac{c_{i,j+1} - c_{i,j-1}}{2\Delta y} \cos\theta \right)$$

Note that grid point $(i,j)$ is the shallowest one and that the division by $c_{i,j}$ is not correct, i.e. it is not consistent with the Snel's law! It will overestimate the rate of turning. This error becomes rather large when bottom slopes are exceptionally large so that wave energy may turn over more than one directional bin. This justifies again the use of the refraction limiter, Eq. (3.41). An appropriate upper bound is obtained with $\alpha_\theta = 0.9$ that particularly holds for relative long waves[8]. For shorter waves, a smaller upper bound may be chosen (e.g. $\alpha_\theta = 0.5$). However, one may choose a larger CFL upper bound. For instance, referring to Figure 3.6, i.e. parallel depth contours within $90^o$, waves can not turn more than $90^o$ (in line with the Snel's law), which implies $\alpha_\theta = 9$, if $\Delta\theta = 10^o$.

In case of unstructured grids, first order approximations for the gradient of depth or phase velocity have been replaced by a more accurate formula based on the Green-Gauss formula like Eq. (8.36).

## 3.9   Governing equations in curvilinear co-ordinates

A curvilinear grid is characterized by the co-ordinates of the grid points, i.e.

$$x_{i,j} , \qquad i = 1, ..., M , j = 1, ..., N \tag{3.44}$$

---

[8]According to the Snel's law a wave direction with respect to the normal of a coastline within a directional bin $\Delta\theta$ can not turn more than $\Delta\theta$.

$$y_{i,j}, \qquad i = 1, ..., M, j = 1, ..., N \tag{3.45}$$

The four-sweep method is unchanged, so in the first sweep action densities in the points $(i-1, j)$ and $(i, j-1)$ are used to compute the action densities in the point $(i, j)$. Numerical approximations are obtained by a 2-dimensional Taylor expansion with respect to the point $(x_{i,j}, y_{i,j})$.

The differences in quantities between neighbouring grid points in the curvilinear grid are denoted as follows:

$$\Delta x_1 = x_{i,j} - x_{i-1,j}, \qquad \Delta y_1 = y_{i,j} - y_{i-1,j}, \qquad \Delta F_1 = F_{i,j} - F_{i-1,j} \tag{3.46}$$

and

$$\Delta x_2 = x_{i,j} - x_{i,j-1}, \qquad \Delta y_2 = y_{i,j} - y_{i,j-1}, \qquad \Delta F_2 = F_{i,j} - F_{i,j-1} \tag{3.47}$$

The partial derivatives can be found from the 2-dimensional Taylor expansions:

$$\Delta F_1 = \frac{\partial F}{\partial x} \Delta x_1 + \frac{\partial F}{\partial y} \Delta y_1 \tag{3.48}$$

and

$$\Delta F_2 = \frac{\partial F}{\partial x} \Delta x_2 + \frac{\partial F}{\partial y} \Delta y_2 \tag{3.49}$$

It follows that the partial derivatives can be approximated by

$$\frac{\partial F}{\partial x} \approx \frac{\Delta y_2 \Delta F_1 - \Delta y_1 \Delta F_2}{[D]} \tag{3.50}$$

and

$$\frac{\partial F}{\partial y} \approx \frac{\Delta x_1 \Delta F_2 - \Delta x_2 \Delta F_1}{[D]} \tag{3.51}$$

where

$$[D] = \Delta y_2 \Delta x_1 - \Delta y_1 \Delta x_2 \tag{3.52}$$

Thus, in curvilinear co-ordinates the complete propagation terms (including time-derivative, but ignoring dependence on $\sigma$ and $\theta$ temporarily) read:

$$\left( \frac{1}{\Delta t} + (D_{x,1} + D_{x,2})c_{x,i,j}^+ + (D_{y,1} + D_{y,2})c_{y,i,j}^+ \right) N_{i,j}^+$$
$$- \frac{N_{i,j}^-}{\Delta t} - D_{x,1}(c_x N)_{i-1,j}^+ - D_{y,1}(c_y N)_{i-1,j}^+$$
$$- D_{x,2}(c_x N)_{i,j-1}^+ - D_{y,2}(c_y N)_{i,j-1}^+ = S_{i,j}^+ \tag{3.53}$$

where

$$D_{x,1} = \frac{\Delta y_2}{[D]}, \quad D_{y,1} = -\frac{\Delta x_2}{[D]}, \quad D_{x,2} = -\frac{\Delta y_1}{[D]}, \quad D_{y,2} = \frac{\Delta x_1}{[D]} \tag{3.54}$$

Here, the superscript $+$ denotes the new time level $t$, and $-$ the old time level $t - \Delta t$. The equation for a stationary computation is found by putting $1/\Delta t$ to 0.

Again, the marching method is stable as long as the propagation direction towards the point $(i, j)$ is enclosed between the lines connecting this point with its neighbours $(i-1, j)$ and $(i, j-1)$. It can be shown that this is the case if

$$D_{x,1}c_x + D_{y,1}c_y \geq 0 \quad \text{and} \quad D_{x,2}c_x + D_{y,2}c_y \geq 0 \tag{3.55}$$

This set of criterions enables the SWAN program to decide whether a certain spectral direction does belong in the sweep which is being processed (in this the first sweep).

In the second sweep, $\Delta x_1 = x_{i,j} - x_{i,j-1}$, etc. and $\Delta x_2 = x_{i,j} - x_{i+1,j}$, etc. In the third sweep, $\Delta x_1 = x_{i,j} - x_{i+1,j}$, etc. and $\Delta x_2 = x_{i,j} - x_{i,j+1}$, etc. In the fourth sweep, $\Delta x_1 = x_{i,j} - x_{i,j+1}$, etc. and $\Delta x_2 = x_{i,j} - x_{i-1,j}$, etc. Otherwise, all of the above equations and conditions remain the same.

Conservation of action in the numerical approximation can be demonstrated for the triangle of which the corners are the three points $(i, j)$, $(i-1, j)$ and $(i, j-1)$. If for each side of this triangle the energy flux is computed as the inner product of the average of $cN$ and an inward-pointing normal of the side itself, then the three energy fluxes are exactly in balance assuming that the situation is stationary, and the source term is zero. In this case it is found that:

$$[c_x N]^+_{i,j} (\Delta y_2 - \Delta y_1) + [c_x N]^+_{i-1,j} (-\Delta y_2) + [c_x N]^+_{i,j-1} (\Delta y_1) +$$
$$[c_y N]^+_{i,j} (\Delta x_1 - \Delta x_2) + [c_y N]^+_{i-1,j} (\Delta x_2) + [c_y N]^+_{i,j-1} (-\Delta x_1) = 0 \tag{3.56}$$

## 3.10   Computation of force in curvilinear co-ordinates

FORCE is the wave-driven stress, i.e. the force per unit surface driving the wave-driven current, expressed in N/m$^2$, is defined as the derivative of the radiation stresses:

$$S_{xx} = \rho g \int \lfloor n \cos^2 \theta + n - \frac{1}{2} \rfloor E d\sigma d\theta \tag{3.57}$$

$$S_{xy} = S_{yx} = \rho g \int n \sin \theta \cos \theta E d\sigma d\theta \tag{3.58}$$

$$S_{yy} = \rho g \int \lfloor n \sin^2 \theta + n - \frac{1}{2} \rfloor E d\sigma d\theta \tag{3.59}$$

Here, $n$ is the ratio of group velocity and phase velocity, i.e.

$$n = \frac{c_g k}{\omega} \tag{3.60}$$

The force is then

$$F_x = -\frac{\partial S_{xx}}{\partial x} - \frac{\partial S_{xy}}{\partial y} \tag{3.61}$$

and

$$F_y = -\frac{\partial S_{yx}}{\partial x} - \frac{\partial S_{yy}}{\partial y} \tag{3.62}$$

In order to compute the force, the derivative of the radiation stress tensor has to be taken. Let $f$ be one of the components of the tensor. We have to derive expressions for $\partial f/\partial x$ and $\partial f/\partial y$. Derivatives with respect to the computational grid co-ordinates $\xi$ and $\eta$ can easily be found. The transformation is based on:

$$\frac{\partial f}{\partial \xi} = \frac{\partial f}{\partial x}\frac{\partial x}{\partial \xi} + \frac{\partial f}{\partial y}\frac{\partial y}{\partial \xi} \tag{3.63}$$

and

$$\frac{\partial f}{\partial \eta} = \frac{\partial f}{\partial x}\frac{\partial x}{\partial \eta} + \frac{\partial f}{\partial y}\frac{\partial y}{\partial \eta} \tag{3.64}$$

Hence,

$$\frac{\partial f}{\partial x} = \frac{\frac{\partial f}{\partial \xi}\frac{\partial y}{\partial \eta} - \frac{\partial f}{\partial \eta}\frac{\partial y}{\partial \xi}}{\frac{\partial x}{\partial \xi}\frac{\partial y}{\partial \eta} - \frac{\partial x}{\partial \eta}\frac{\partial y}{\partial \xi}} = \frac{\partial f}{\partial \xi}\frac{\partial \xi}{\partial x} + \frac{\partial f}{\partial \eta}\frac{\partial \eta}{\partial x} \tag{3.65}$$

and

$$\frac{\partial f}{\partial y} = \frac{\frac{\partial f}{\partial \xi}\frac{\partial x}{\partial \eta} - \frac{\partial f}{\partial \eta}\frac{\partial x}{\partial \xi}}{\frac{\partial y}{\partial \xi}\frac{\partial x}{\partial \eta} - \frac{\partial y}{\partial \eta}\frac{\partial x}{\partial \xi}} = \frac{\partial f}{\partial \xi}\frac{\partial \xi}{\partial y} + \frac{\partial f}{\partial \eta}\frac{\partial \eta}{\partial y} \tag{3.66}$$

Numerical approximations are quite simple:

$$\frac{\partial f}{\partial \xi} \approx \frac{f_{\xi+1,\eta} - f_{\xi-1,\eta}}{2} \, , \qquad \frac{\partial f}{\partial \eta} \approx \frac{f_{\xi,\eta+1} - f_{\xi,\eta-1}}{2} \tag{3.67}$$

These expressions are also used for derivatives of $x$ and $y$. On the boundaries of the computational region a one-sided approximation can be used.

## 3.11   Numerical treatment of obstacles

An obstacle is treated in SWAN as a line running through the computational grid, see Figure 3.7. When treating one grid point SWAN will first determine whether one of the grid lines of the stencil crosses an obstacle; see Section 3.12 for the procedure to determine whether or not there is a crossing point. If there is a crossing it will fall back to the first order upwind scheme.

In computing the action densities for the target grid point (point 0 in Figure 3.8), the contribution of a neighbouring grid point (point 1 in this case) is reduced by $K_t^2$, if the connection between the two grid points crosses the obstacle. (Note that the power 2 comes from the definition of the transmission coefficient which is in terms of wave height). The contribution from point 2 in the computation of point 0 is not reduced because there is no
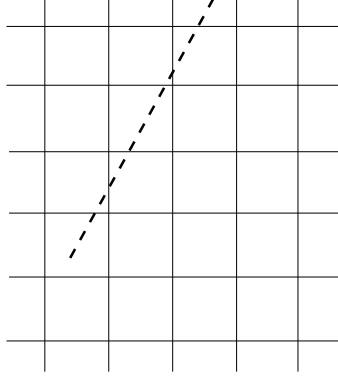
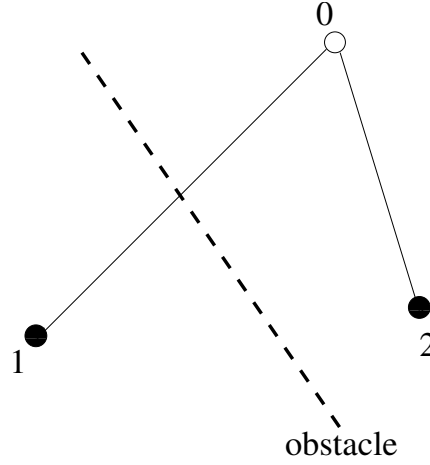Figure 3.7: An obstacle as a line in computational grid.



Figure 3.8: Schematic sketch of transmission in SWAN.

obstacle crossing in between; the program takes $K_t = 1$ for this point.

A consequence of the above procedure is that the results are the same as long as the obstacle crosses the same grid lines. Thus the results for the situation shown would be the same if the obstacle would be longer as long as the end would be in the same mesh. Another consequence is that an obstacle has to cross at least a few grid lines in order to have a noticeable effect, see Figure 3.7.

After the transmission coefficient has been calculated, it is used in the propagation terms of the action balance equation. In curvilinear coordinates, the propagation terms (including time-derivative, but ignoring dependence on $\sigma$ and $\theta$ temporarily) read:

$$\left( \frac{1}{\Delta t} + (D_{x,1} + D_{x,2})c_{x,i,j}^+ + (D_{y,1} + D_{y,2})c_{y,i,j}^+ \right) N_{i,j}^+$$
$$- \frac{N_{i,j}^-}{\Delta t} - D_{x,1}(c_x K_{t,1}^2 N)_{i-1,j}^+ - D_{y,1}(c_y K_{t,1}^2 N)_{i-1,j}^+$$

$$-D_{x,2}(c_x K_{t,2}^2 N)_{i,j-1}^+ - D_{y,2}(c_y K_{t,2}^2 N)_{i,j-1}^+ = S_{i,j}^+ \tag{3.68}$$

In order to simplify the procedure, a reflected wave in a grid point is calculated from the incident wave components in the same grid point. This introduces numerical inaccuracies, but that is not uncommon in numerical models. A basic condition in numerical models is that the approximation approaches the correct limit as smaller and smaller step sizes are used.

A reflected wave component in the target grid point 0, as illustrated by the arrow pointing away from the obstacle in Figure 3.9, would get contributions from grid points 1 and 2 if
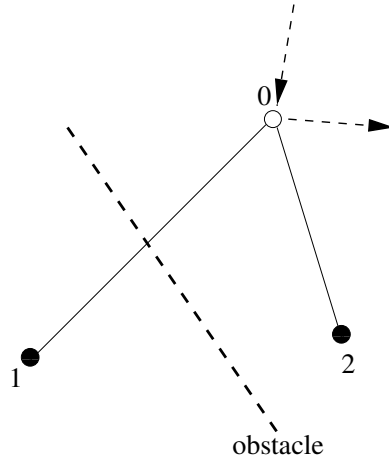


Figure 3.9: Schematic sketch of reflection in SWAN.

there would not be an obstacle. If the obstacle is there in the way shown, the contribution from point 2 is unchanged, but the contribution from point 1 is

- reduced by a transmission coefficient and

- partially replaced by the reflection of an incoming component in point 0.

Reflection only works when both grid points 0 and 1, as shown in Figure 3.9, are wet points. This implies that obstacle lines are only effective when bordered by wet points on both sides of the obstacle.

## 3.12  Crossing of obstacle and grid line

In the procedure for obstacles it is necessary to determine the crossing point of the obstacle and a grid line in the computational grid. The obstacle is composed of straight sides. Let one side have the end points $\vec{x}_3 = (x_3, y_3)$ and $\vec{x}_4 = (x_4, y_4)$. The end points of the grid line (both computational grid points) are $\vec{x}_1 = (x_1, y_1)$ and $\vec{x}_2 = (x_2, y_2)$. The crossing point must obey the following equation

$$\vec{x}_1 + \lambda(\vec{x}_2 - \vec{x}_1) = \vec{x}_3 + \mu(\vec{x}_4 - \vec{x}_3) \tag{3.69}$$

where both $\lambda$ and $\mu$ must be between 0 and 1. It follows that

$$\lambda = \frac{(x_1 - x_3)(y_2 - y_1) - (y_1 - y_3)(x_2 - x_1)}{(x_4 - x_3)(y_2 - y_1) - (y_4 - y_3)(x_2 - x_1)} \tag{3.70}$$

and

$$\mu = \frac{(x_1 - x_3)(y_4 - y_3) - (y_1 - y_3)(x_4 - x_3)}{(x_4 - x_3)(y_2 - y_1) - (y_4 - y_3)(x_2 - x_1)} \tag{3.71}$$

If the denominator in both expressions is zero, the two lines are parallel and it is assumed that there is no crossing.

## 3.13   Integration over $\sigma$

Two methods are considered in SWAN for integration over frequency space. The first method is the common trapezoidal rule. We consider the following integration

$$I = \int_0^{\sigma_m} f\, E(\sigma) d\sigma \tag{3.72}$$

where $\sigma_m$ is the highest spectral frequency and $f$ is an arbitrary function. Usually, this function may be $\sigma^p$, $\omega^p$ or $k^p$ with $p$ a power. We assume a discrete (logarithmic) distribution of frequencies: $\sigma_i$, $i = 1, ..., m$. The approximation of (3.72) is as follows:

$$I \approx \sum_2^m \frac{1}{2}(f_{i-1}\sigma_{i-1}N_{i-1} + f_i\sigma_i N_i)(\sigma_i - \sigma_{i-1}) \tag{3.73}$$

The contribution by the tail needs to be added as well, as follows. The tail of the energy density is proportional to $\sigma^{-P^*}$. We have,

$$\int_{\sigma_m}^{\infty} R\sigma^{-P^*} d\sigma = \sigma_m \frac{R\sigma_m^{-P^*}}{P^* - 1} \tag{3.74}$$

Assuming that a function $f$ has a tail with power $P^*$, so that $R\sigma_m^{-P^*} = f(\sigma_m)$. Hence,

$$\int_{\sigma_m}^{\infty} f(\sigma) d\sigma = \frac{\sigma_m}{P^* - 1} f(\sigma_m) \tag{3.75}$$

This integration is only valid if $P^* > 1$.

The second technique for integration over $\sigma$ makes use of the logarithmic discrete distribution of frequencies. We introduced two variables in SWAN: `FRINTF` and `FRINTH`. The first is equal to $\ln(\sigma_{i+1}/\sigma_i)$, the latter to $\sqrt{\sigma_{i+1}/\sigma_i}$. Hence, $\sigma_i = e^{\mu i}$ with $\mu = \ln(\sigma_{i+1}/\sigma_i)$ and can be approximated as $\mu = \Delta\sigma/\sigma$.

The integral over a function of $\sigma$, i.e. $f(\sigma)$ is transformed as follows:

$$\int f(\sigma) d\sigma = \int f(\sigma)\mu e^{\mu i} di = \mu \int f(\sigma)\sigma di \tag{3.76}$$

Thus, the integral can be approximated as

$$\int f(\sigma)d\sigma \approx \mu \sum f_i \sigma_i \tag{3.77}$$

The boundaries of a mesh in $\sigma-$space are $\sigma_i/\sqrt{\sigma_{i+1}/\sigma_i}$ and $\sigma_i\sqrt{\sigma_{i+1}/\sigma_i}$.

Computation of the contribution by the tail is done as follows. It is assumed that in the tail the energy density is proportional to $\sigma^{-P^*}$. Furthermore, the discrete integration extends to $M \cdot \sigma_m$, where $M = \sqrt{1 + \Delta\sigma/\sigma}$. Then the contribution by the tail is:

$$\int_{\theta=0}^{2\pi} \int_{M\sigma_m}^{\infty} R\sigma^{-P^*} d\sigma d\theta = R\frac{M^{1-P^*} \cdot \sigma_m^{1-P^*}}{P^* - 1} = \frac{\sigma_m}{(P^* - 1)M^{P^*-1}}R\sigma_m^{-P^*} \tag{3.78}$$

Assuming that a function $f$ has a tail with power $P^*$, the integral over $f$ has a tail contribution of

$$\int_{\theta=0}^{2\pi} \int_{M\sigma_m}^{\infty} f(\sigma)d\sigma d\theta = \frac{\sigma_m}{(P^* - 1)M^{P^*-1}}f(\sigma_m) \tag{3.79}$$

Since, $M$ is close to 1, the tail factor can be approximated as

$$\frac{\sigma_m}{(P^* - 1)M^{P^*-1}} \approx \frac{\sigma_m}{(P^* - 1)(1 + (P^* - 1)(M - 1))} \tag{3.80}$$

In the SWAN program, we have $M =$`FRINTH`, $P^* =$`PWTAIL(1)` and $m =$`MSC`. The value of $P^*$ depends on the quantity that is integrated. For instance, in the computation of $\overline{k}$, $P^* = P - 2n - 1$. Note that it is required that $P^* > 1$, otherwise the integration fails.

## 3.14 Transformation from relative to absolute frequency

Internally, SWAN use action density as function of direction and relative (angular) frequency. Users may want to obtain results in terms of absolute frequency, if only because measurements were taken at fixed positions.

Two modifications of the SWAN model that were needed to supply the information to the users are

- the computation of integrated quantities such as average absolute frequency and

- the transformation of action or energy density.

The average absolute frequency is determined as follows:

$$\overline{\omega} = \frac{\int \omega E(\sigma, \theta)d\sigma d\theta}{\int E(\sigma, \theta)d\sigma d\theta} \tag{3.81}$$

The transformation of action or energy density from relative frequency $\sigma$ to absolute frequency $\omega$ is complicated because the mapping is not one-to-one, and therefore the Jacobian can become infinite. The value of $\omega$ is determined by $\omega = W(\sigma)$.

The transformation is designed such that the following requirements are met:

- If current velocities tend to zero the action densities for absolute frequency become identical with the densities with respect to relative frequency.

- The total energy density with respect to relative density is identical with the total energy density with respect to absolute density.

Furthermore, it is assumed that the distribution of absolute frequencies is the same as the distribution of relative frequencies.

In the continuous model the mapping is done by

$$E(\omega.\theta) = \int E(\sigma, \theta)\delta(\omega - W(\sigma))d\sigma \tag{3.82}$$

This relation is discretized whereby the energy density is assumed to be constant over intervals from $\sigma_i/M$ to $M\sigma_i$.

## 3.15   Interpolation of spectra

The interpolation of spectra in SWAN, both in space and time, is a slight modification of the procedure as used in WAM. This procedure is not a simple (spectral) bin-by-bin interpolation because that would cause reduction of the spectral peak if the peaks of the original spectra do not coincide. It is an interpolation where the spectra are first normalized by average frequency and direction, then interpolated and then transformed back.

The average frequencies of the two origin spectra are determined using the frequency moments of the spectra

$$m_{i,k} = \int N_i(\sigma, \theta)\sigma^k d\sigma d\theta \tag{3.83}$$

with $i$=1,2 (the two origin spectra) and $k$=0,1 (the zero- and first frequency moments of these spectra). Then

$$\overline{\sigma}_i = \frac{m_{i,1}}{m_{i,0}} \tag{3.84}$$

The average frequency for the interpolated spectrum is calculated as

$$\overline{\sigma} = (w_2 m_{1,1} + w_1 m_{2,1})/(w_2 m_{1,0} + w_1 m_{2,0}) \tag{3.85}$$

where $w_1$ is the relative distance (in space or time) from the interpolated spectrum to the first origin spectrum $N_1(\sigma, \theta)$ and $w_2$ is the same for the second origin spectrum $N_2(\sigma, \theta)$. Obviously, $w_1 + w_2 = 1$.

The average directions of the two origin spectra are determined using directional moments of the spectra:

$$m_{i,x} = \int N_i(\sigma, \theta)\cos(\theta)d\sigma d\theta \tag{3.86}$$

and

$$m_{i,y} = \int N_i(\sigma, \theta) \sin(\theta) d\sigma d\theta \tag{3.87}$$

with $i$=1,2. The average direction is then

$$\overline{\theta}_i = \mathrm{atan}(\frac{m_{i,y}}{m_{i,x}}) \tag{3.88}$$

The average direction of the interpolated spectrum is calculated as

$$\overline{\theta} = \mathrm{atan}[\frac{w_2 m_{1,y} + w_1 m_{2,y}}{w_2 m_{1,x} + w_1 m_{2,x}}] \tag{3.89}$$

Finally the interpolated spectrum is calculated as follows:

$$N(\sigma, \theta) = w_2 N_1[\overline{\sigma}_1 \sigma / \overline{\sigma}, \theta - (\overline{\theta} - \overline{\theta}_1)] + w_1 N_2[\overline{\sigma}_2 \sigma / \overline{\sigma}, \theta - (\overline{\theta} - \overline{\theta}_2)] \tag{3.90}$$

## 3.16 Computation of breaking source term

The surf breaking dissipation of Battjes and Janssen (1978) reads

$$D_{\mathrm{tot}} = -\alpha_{\mathrm{BJ}} Q_b \tilde{\sigma} \frac{H_{\mathrm{max}}^2}{8\pi} \tag{3.91}$$

The surf breaking source term for each spectral bin $i$ is

$$S_i = \frac{D_{\mathrm{tot}}}{E_{\mathrm{tot}}} E_i = \tilde{D} \, E_i \tag{3.92}$$

with the normalized total dissipation

$$\tilde{D} = -\frac{\alpha_{\mathrm{BJ}} \tilde{\sigma} Q_b}{\pi \mathcal{B}} < 0 \tag{3.93}$$

and

$$\mathcal{B} = \frac{8 E_{\mathrm{tot}}}{H_{\mathrm{max}}^2} = \left(\frac{H_{\mathrm{rms}}}{\gamma d}\right)^2 \tag{3.94}$$

Since, the source term is strongly nonlinear in $E$ (since $\tilde{D}$ depends on $E$ through $\mathcal{B}$), we apply the Newton linearisation to approximate the source term at iteration level $n+1$, as follows:

$$S_i^{n+1} \approx \tilde{D} E_i^n + \left(\frac{\partial S}{\partial E}\right)_i^n (E_i^{n+1} - E_i^n) \tag{3.95}$$

In SWAN, this approximation has been slightly adapted for reasons of numerical stability; the first term in the right hand side, $\tilde{D} E_i^n$, is replaced by $\tilde{D} E_i^{n+1}$. This preserves positivity of energy density $E$, if the following inequality holds

$$\frac{\partial S}{\partial E} < 0 \tag{3.96}$$

We derive an expression for this derivative as follows. From (3.92), we have

$$\frac{\partial S}{\partial E}|_i = \frac{\partial \tilde{D}}{\partial E}|_i E_i + \tilde{D} \tag{3.97}$$

The normalized dissipation $\tilde{D}$ is a function of $\mathcal{B}$ which is proportional to $E$, so

$$\frac{\partial S}{\partial E}|_i = \frac{\partial \tilde{D}}{\partial \mathcal{B}}|_i \mathcal{B}_i + \tilde{D} \tag{3.98}$$

Since, $Q_b$ is a function of $\mathcal{B}$, we get (using the quotient rule)

$$\frac{\partial S}{\partial E}|_i = -\frac{\alpha_{\text{BJ}}\tilde{\sigma}}{\pi} \frac{\partial Q_b}{\partial \mathcal{B}} \tag{3.99}$$

Since,

$$1 - Q_b + \mathcal{B}\ln Q_b = 0 \tag{3.100}$$

the derivative of $Q_b$ is found by differentiating this with respect to $\mathcal{B}$:

$$-Q'_b + \ln Q_b + \frac{\mathcal{B}}{Q_b}Q'_b = 0 \tag{3.101}$$

Hence,

$$Q'_b = \frac{\ln Q_b}{1 - \mathcal{B}/Q_b} = \frac{Q_b}{\mathcal{B}}\frac{Q_b - 1}{Q_b - \mathcal{B}} \tag{3.102}$$

using Eq. (3.100). Now, $Q'_b > 0$, because $0 < Q_b < 1$ and $\mathcal{B} > Q_b$. Substitution in (3.99) gives

$$\frac{\partial S}{\partial E}|_i = \tilde{D}\frac{Q_b - 1}{Q_b - \mathcal{B}}|_i < 0 \tag{3.103}$$

Finally, the approximation of the source term reads

$$S_i^{n+1} = \tilde{D}\left(1 + \frac{Q_b - 1}{Q_b - \mathcal{B}}\right)_i^n E_i^{n+1} - \tilde{D}\frac{Q_b - 1}{Q_b - \mathcal{B}}|_i^n E_i^n \tag{3.104}$$

# Chapter 4

# Wave boundary and initial conditions

To obtain the numerical solution of the action balance equation (2.16), the wave boundary and initial conditions should be provided. The incoming wave components at the up-wave boundaries in the SWAN model are specified by a two-dimensional spectrum. Several options are available:

- A parametric one-dimensional spectrum with a certain imposed directional distribution. An example is a Jonswap spectrum.

- A discrete one-dimensional spectrum with a certain imposed directional distribution. This is often obtained from measurements.

- A discret two-dimensional spectrum. This may be obtained from other SWAN runs or other models, e.g. WAM and WAVEWATCH III.

For the parametric one-dimensional spectrum, the following optional forms have been recommended: a Pierson-Moskowitz spectrum (Pierson and Moskowitz, 1964), a Jonswap spectrum (Hasselmann *et al.*, 1973) and a Gaussian-shaped spectrum.

The boundaries in frequency space are fully absorbing at the lowest and the highest discrete frequency. So, energy can freely propagate across these boundaries and thus total energy might not be conserved in some cases. However, a diagnostic tail $f^{-m}$ ($m = 4$ or $m = 5$) is added above the high frequency cut-off, which is used to compute nonlinear wave-wave interactions at the high frequencies and to compute integral wave parameters. When the directional space is a closed circular, no directional boundary conditions are needed. However, for reasons of economy, SWAN has an option to compute only wave components in a pre-defined directional sector. In this case, the boundaries of this sector are fully absorbing (action density might be removed from the model by refraction).

To facilitate the integration process of the action balance equation, wave boundary conditions in geographical space need to be provided. The boundaries of the computational grid in SWAN are either land or water. In case of land there is no problem. The land does not generate waves and in SWAN it absorbs all incoming wave energy. But in the case of

a water boundary there is a problem. If observations are available, they can be used as inputs at the boundary. In case no wave conditions are given along the boundary, SWAN assumes that no waves enter the model and waves can leave the model freely along that boundary. This assumption results in errors. Therefore, to get reliable results, especially for such case, the model boundaries must be placed far away from the area of interest.

In case of nonstationary computation, the default initial spectra are computed from the local wind velocities using the deep-water growth curve of Kahma and Calkoen (1992), cut off at values of significant wave height and peak frequency from Pierson and Moskowitz (1964). The average (over the model area) spatial step size is used as fetch with local wind. The shape of the spectrum is default Jonswap with a $\cos^2(\theta)$ directional distribution centred around the local wind direction.

The first guess conditions of a stationary run of SWAN are default determined with the second generation mode of SWAN.

It is possible to obtain an initial state by carrying out a previous stationary or nonstationary computation.

# Chapter 5

# Implementation of 2D wave setup

## 5.1   Introduction

Wave setup is usually confined to narrow zones in the immediate vicinity of the shoreline. The size of such areas is small enough that the setup process can be considered to be quasi-stationary. Wave-induced currents are usually weak compared to tidal currents. This implies an equilibrium between the wave-induced force and gradient of the wave setup,

$$
gd \left( \frac{\partial \zeta}{\partial x} + \frac{\partial \zeta}{\partial y} \right) + F_x + F_y = 0 \tag{5.1}
$$

where $\zeta$ is the setup, $d$ the water depth and $F_i$ is the wave-induced force in $x_i$-direction per unit mass. In order to reduce the number of equations to one, we use the observation by Dingemans (1997) that wave-driven currents are mainly due to the divergence-free part of the wave forces whereas the setup is mainly due to the rotation-free part of the force field. We therefore take the divergence of eq. (5.1) to obtain the following elliptic partial differential equation for $\zeta$,

$$
\frac{\partial}{\partial x}(gd\frac{\partial \zeta}{\partial x}) + \frac{\partial}{\partial y}(gd\frac{\partial \zeta}{\partial y}) + \frac{\partial F_x}{\partial x} + \frac{\partial F_y}{\partial y} = 0 \tag{5.2}
$$

This Poisson equation needs one boundary condition in each point of the boundary of the computational domain. Two types of boundary conditions are foreseen; the first one is used on the open boundaries and on the shoreline where the shoreline is defined as the line where the depth is zero:

$$
F_n + gd\frac{\partial \zeta}{\partial n} = 0 \tag{5.3}
$$

with $n$ the outward direct normal. It is not possible to use this boundary condition on all boundary points because then there remains an unknown constant. So some point for which we take the boundary point with the largest depth, the setup is assumed to be $\zeta = 0$.

The second type of boundary condition with given value of $\zeta$ is also used in nested models.

The setup computed in the larger model is used as boundary condition in the nested model. In the nested model the setup is given in all points of the outer boundary. On the shoreline inside the area again eq. (5.3) is used.

The Poisson equation (5.2) together with its boundary conditions will be solved numerically on a curvilinear grid. The next section discusses the details of the method. After each iteration performed in SWAN new values of the setup are being calculated and added to the depth, so that the SWAN model incorporates the effect of setup on the wave field. An output quantity SETUP is added so that the user can be informed about the magnitude and distribution of the wave setup.

## 5.2   Numerical approach

### 5.2.1   Discretization of the 2D setup equation

**Problem definition**

The equation to be solved has the following form:

$$\frac{\partial}{\partial x_k}(F_k + gd\frac{\partial \zeta}{\partial x_k}) = 0 \; , \tag{5.4}$$

In order to solve (5.4), the following types of boundary conditions may be applied

$$F_n + gd\frac{\partial \zeta}{\partial n} = 0 \quad \text{at the boundary} \; , \tag{5.5}$$

with $n$ the outward direct normal. This is a Neumann condition. The setup is fixed upon an additive constant.

$$\zeta = \text{ given at the boundary} \; . \tag{5.6}$$

This is boundary condition of Dirichlet type. At beaches always the Neumann condition (5.5) is applied.

In order to solve (5.4) with boundary conditions (5.5) and (5.6) a boundary fitted, vertex centered finite volume method is applied. In the remainder of this Chapter we use $k$ instead of $gd$.

**Discretization**

The physical domain is mapped onto a rectangular domain in the $(\xi^1, \xi^2)$ plane, which is called the computational domain. All points of the domain are used, including the dry ones.

Using the relation (summation convection applied)

$$\frac{\partial \varphi}{\partial x^\beta} = \frac{1}{\sqrt{g}}\frac{\partial}{\partial \xi^\gamma}(\sqrt{g} \, a_\beta^{(\gamma)} \, \varphi) \; , \tag{5.7}$$

with $a_\beta^{(\gamma)}$ the components of the contravariant basevectors $\vec{a}^{(\alpha)}$ defined as

$$\vec{a}^{(\alpha)} = \nabla \xi^\alpha \,, \tag{5.8}$$

and $\sqrt{g}$ the Jacobian of the transformation

$$\sqrt{g} = a_{(1)}^1 a_{(2)}^2 - a_{(1)}^2 a_{(2)}^1 \,. \tag{5.9}$$

$\vec{a}_{(\alpha)}$ are the covariant base vectors defined by

$$\vec{a}_{(\alpha)} = \frac{\partial \vec{x}}{\partial \xi^\alpha} \,. \tag{5.10}$$

The contravariant base vectors follow immediately from the covariant ones due to:

$$\sqrt{g}\vec{a}^{(1)} = (a_{(2)}^2, \; -a_{(2)}^1)^T \,, \tag{5.11}$$
$$\sqrt{g}\vec{a}^{(2)} = (-a_{(1)}^2, \; a_{(1)}^1)^T \,. \tag{5.12}$$

Application of (5.7) to equation (5.5) results in

$$\frac{1}{\sqrt{g}} \frac{\partial}{\partial \xi^\alpha} (\sqrt{g}\vec{a}^{(\alpha)} \cdot (k\nabla\zeta + \vec{F})) = 0 \,. \tag{5.13}$$

Note that $\nabla\zeta$ is a derivative in the Cartesian ($\vec{x}$) direction and not in the $\vec{\xi}$ direction.

In the remainder we shall use the local numbering as given in Figure 5.1. The points (0,0),
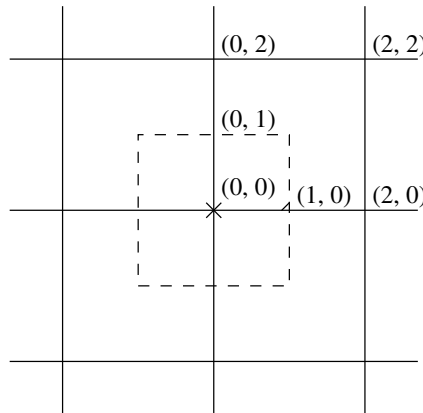


Figure 5.1: Local numbering in computational domain

(2,0), (0,2) and so on are the vertices of the cells. The integration cell for the finite volume method is defined by the cell $\Omega$ (-1,0), (0,-1), (1,0), (0,1).

Integrating (5.13) over this cell gives

$$\int_{\Omega_x} \frac{1}{\sqrt{g}} \frac{\partial}{\partial \xi^\alpha} (\sqrt{g} \vec{a}^{(\alpha)} \cdot (k\nabla\zeta + \vec{F})) d\Omega_x$$

$$\int_{\Omega_\xi} \frac{\partial}{\partial \xi^\alpha} (\sqrt{g} \vec{a}^{(\alpha)} \cdot (k\nabla\zeta + \vec{F})) d\Omega_\xi \tag{5.14}$$

$$\approx \sqrt{g} \vec{a}^{(1)} \cdot (k\nabla\zeta + F)|_{(-1,0)}^{(1,0)} + \sqrt{g} \vec{a}^{(2)} \cdot (k\nabla\zeta + \vec{F})|_{(0,-1)}^{(0,1)} ,$$

where $\Omega_x$ is the cell in the physical space and $\Omega_\xi$ the cell in the computational domain. The four points (1,0), (0,1), (-1,0) and (0,-1) will be cell integration points. The covariant basis vectors $\vec{a}_{(\alpha)}$ are approximated by central differences

$$\vec{a}_{(2)}|_{(0,1)} = \vec{x}_{(0,2)} - \vec{x}_{(0,0)} , \tag{5.15}$$

$$\vec{a}_{(1)}|_{(1,0)} = \vec{x}_{(2,0)} - \vec{x}_{(0,0)} , \tag{5.16}$$

and by linear interpolation in other points. In these relations we have used that the step width in the computational domain is equal to 1.

The term $\nabla\zeta$ needs special attention. Since it concerns derivatives in the $\vec{x}$ direction, whereas all derivatives in the computational domain are in the $\vec{\xi}$ directions it is necessary to make some approximation. We approximate this term by the integration path method as outlined in Wesseling (2001).

To that end $\nabla\zeta$ is integrated in two independent directions $\xi^1$ and $\xi^2$. This yields two equations to express $\frac{\partial\zeta}{\partial x}$ and $\frac{\partial\zeta}{\partial y}$ in $\zeta$ values of neighbours.

$$(\vec{x}_{2,0} - \vec{x}_{),0})\nabla\zeta|_{(1,0)} = \zeta_{2,0} - \zeta_{0,0} , \tag{5.17}$$

$$\frac{1}{2}((\vec{x}_{2,2} - \vec{x}_{2,-2}) + (\vec{x}_{0,2} - \vec{x}_{0,-2}))\nabla\zeta|_{(1,0)} = \frac{1}{2}((\zeta_{2,2} - \zeta_{2,-2}) + (\zeta_{0,2} - \zeta_{0,-2})) . \tag{5.18}$$

(5.17), (5.18) may be considered as two sets of equations to express $\nabla\zeta$ into $\zeta$ values. Solution of this linear system results in:

$$\nabla\zeta|_{(1,0)} = \zeta|_{(0,0)}^{(2,0)}\vec{c}^{(1)} + (\zeta|_{(0,-2)}^{(0,2)} + \zeta|_{(2,-2)}^{(2,2)})\vec{c}^{(2)} , \tag{5.19}$$

with

$$\vec{c}^1 = \frac{1}{C}(c_{(2)}^2, -c_{(2)}^1) ; \vec{c}^2 = \frac{1}{C}(-c_{(1)}^2, c_{(1)}^1) , \tag{5.20}$$

$$C = c_{(2)}^2 c_{(1)}^1 - c_{(1)}^2 c_{(2)}^1 , \tag{5.21}$$

$$\vec{c}_{(1)} = a_{(1)}|_{(1,0)} \ \vec{c}_{(2)} = \vec{a}_{(2)}|_{(0,-1)} + \vec{a}_{(2)}|_{(0,1)} + \vec{a}_{(2)}|_{(2,-1)} + \vec{a}_{(2)}|_{(2,1)} . \tag{5.22}$$

A similar formula is applied for point (0,1). Equation (5.14) together with expression (5.19) gives one row of the discretized equation.

**Treatment of the boundary conditions**

The boundary conditions at the outer boundary of the domain are relatively easy to implement.

In case of Dirichlet boundary conditions the corresponding row of the matrix is made equal to 0 and the diagonal element is set to 1. The value of the boundary condition is filled into the right hand side.

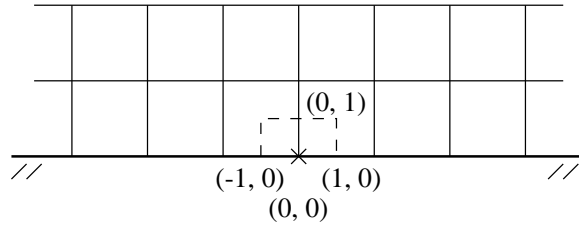Neumann boundary conditions are treated integrating over a half cell as sketched in Figure 5.2. In this case we get:



Figure 5.2: Half cell at boundary

$$
\int_{\Omega_\xi} \frac{\partial}{\partial \xi^\alpha} (\sqrt{g}\vec{a}^{(\alpha)} \cdot (k\nabla\zeta + \vec{F}) d\Omega_\xi
$$

$$
\simeq \frac{1}{2}\sqrt{g}\vec{a}^{(1)} \cdot (k\nabla\zeta + \vec{F})|_{(-1,0)}^{(1,0)} + \sqrt{g}\vec{a}^{(2)} \cdot (k\nabla\zeta + \vec{F})|_{(0,0)}^{(0,1)} . \tag{5.23}
$$

Due to the Neumann boundary conditions the term in the boundary point $(0, 0)$ vanishes.

Mark that in this case we need to evaluate $\nabla\zeta$ at the boundary. In order to do so we apply a one-sided integration path approach i.e.

$$
(\vec{x}_{(2,0)} - \vec{x}_{(1,0)}) \cdot \nabla\zeta|_{(1,0)} = \zeta_{(2,0)} - \zeta_{(0,0)} ,
$$
$$
((x_{(2,2)} - x_{(2,0)}) + (\vec{x}_{(0,2)} - \vec{x}_{(0,0)})) \cdot \nabla\zeta|_{(1,0)} = (\zeta_{(0,2)} - \zeta_{(0,0)}) + (\zeta_{(2,2)} - \zeta_{(2,0)}) \tag{5.24}
$$

Furthermore we need the values of $\vec{a}_{(\alpha)}$ in virtual cells, because we need the $c^{(\alpha)}$ at the boundary. To that end we construct a row of virtual cells by extrapolating the co-ordinates of the boundary cells.

**The implementation of dry points**

Dry points complicate the implementation considerably.

For the dry points itself there is no problem. In fact we make the corresponding row of the matrix, as well as the right hand side element completely equal to zero.
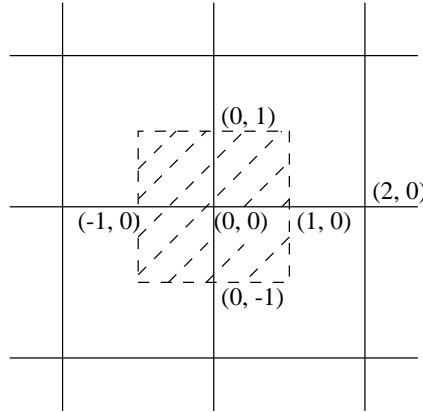
Figure 5.3: Dry point (2, 0) and wet point (0, 0)

Dry points in the neighbourhood of wet points, however, also influence the matrix for the wet point. Consider for example the integration point (1,0) in Figure 5.3. If (0,0) is a wet point and (2,0) a dry point then we assume that at point (1,0) we have a Neumann boundary condition. This means in fact that the contribution of the integration point (1,0) to the matrix and right hand side is equal to zero. With respect to the evaluation of the gradient of $\zeta$ with the integration path method one sided differences are applied for those formulas involving $\zeta_{(2,0)}$. This process is applied for all transitions from wet to dry points. As a consequence, in the case of a situation like in Figure 5.4 we make $\nabla\zeta$ for point 2 zero. The reason is that in point 2 it is only possible to evaluate $\frac{\partial \zeta}{\partial \xi^1}$ and not $\frac{\partial \zeta}{\partial \xi^2}$, and hence we
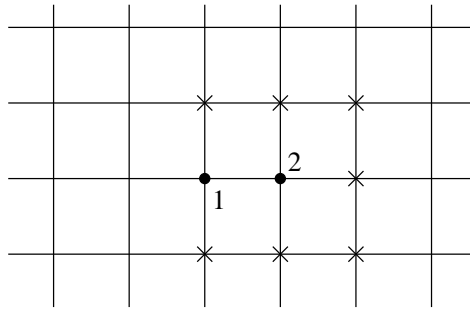


Figure 5.4: Wet points ● enclosed by a row of dry points ×

have too few information to express $\nabla\zeta$ in neighbour values.

## Building of the matrix and right hand side

With respect to the building of matrix and right hand side we start by computing all contributions in the integration points. This is done by looping over the various integration points. Since the contribution of point (0,1) in cell $(i,j)$ is equal to that of point (0, -1) in cell $(i-1, j)$ it is sufficient to loop over two sets of integration points only.

Once we have computed the coefficients in a set of integration points we must add these contributions, multiplied by some factor, to the matrix elements. This process is known as distribution.

## 5.2.2 The iterative solver for the linear system

### Data structure

After the discretization of the Poisson equation in curvilinear co-ordinates, one has to solve the following matrix vector system:

$$Ax = f, \tag{5.25}$$

where $A$ is the discrete Poisson operator, $x$ is an approximation of the setup (of the water level), and the right hand side vector $f$ contains the effects of the boundary conditions and the forces due to the surface waves. In the solver it is very efficient to calculate with direct addressing, so dry points are included in the vector $x$. This implies that the dimension of $x$ and $f$ are fixed and equal to $MXC \times MYC$. In the discretization a 9-point stencil is used. That implies that only 9 matrix elements per row are non-zero. These elements are stored in a diagonal-wise way. So for this part $NWKARR = 9$. The rows corresponding to dry points are filled with zeroes except on the main diagonal where the value 1 is substituted. The value of $x$ and $f$ are taken equal to 0 at these points.

### Properties of the matrix

The discrete operator is symmetric in the inner region. This means that $a_{i,j} = a_{j,i}$. Due to the boundary conditions the symmetry of the operator is lost. The reasons for this are:

- When Dirichlet boundary conditions are used the known elements of $x$ should be eliminated in order to keep the matrix symmetric. However this leads to a different dimension of $A, x$, and $f$, therefore the known elements are not eliminated.

- When dry points occur the derivation of the discrete boundary conditions is already complicated at the interface between wet and dry points. At this moment it is not clear how to discretize these conditions such that the resulting matrix is symmetric.

These difficulties motivate us to use a non-symmetric matrix. This is only a small drawback, because recently good methods have been developed to solve non-symmetric matrix vector systems.

When Neumann conditions are used on all boundaries the resulting matrix is singular. The solution is determined up to a constant. We have to keep this in mind during the construction of the solution procedure.

When Gauss elimination is used to solve equation (5.25), the zero elements in the bend of $A$ become non-zero. This means that the required memory is equal to $2 \times MXC + 2$ vectors. For $MXC$ large, this leads to an unacceptable large amount of memory. Therefore

we use an iterative solution method, where the total amount of memory is less than the memory used in the discretization procedure.

**The iterative solver**

In 1D cases, the wave-induced set-up is calculated in SWAN with a simple trapezoidal rule.

In 2D cases, the Poisson equation of the divergence-free force field is solved in SWAN with a modified Successive Over Relaxation (SOR) technique (Botta and Ellenbroek, 1985). The boundary conditions for this elliptical partial differential equation are:

- at open boundaries: equilibrium between wave force and hydrostatic pressure gradient normal to the model boundary,

- at last grid points before shoreline: equilibrium between wave force and hydrostatic pressure gradient normal to the model boundary and

- at deepest boundary point: set-up is zero.

The shoreline in SWAN moves as dictated by the wave-induced set-up. The set-up computations are available in both the rectilinear and curvilinear grids.

# Chapter 6

# Iterative solvers

## 6.1 Strongly Implicit Procedure (SIP)

We want to solve the following linear system of equations

$$A\,\vec{N} = \vec{b} \tag{6.1}$$

where $A$ is some non-symmetric penta-diagonal matrix, $\vec{N}$ is the wave action vector to be solved and $\vec{b}$ contains source terms and boundary values.

The basis for the SIP method (Stone, 1968; Ferziger and Perić, 1999) lies in the observation that an LU decomposition is an excellent general purpose solver, which unfortunately can not take advantage of the sparseness of a matrix. Secondly, in an iterative method, if the matrix $M = LU$ is a good approximation to the matrix $A$, rapid convergence results. These observations lead to the idea of using an approximate LU factorization of $A$ as the iteration matrix $M$, i.e.:

$$M = LU = A + K \tag{6.2}$$

where $L$ and $U$ are both sparse and $K$ is small. For non-symmetric matrices the incomplete LU (ILU) factorisation gives such an decomposition but unfortunately converges rather slowly. In the ILU method one proceeds as in a standard LU decomposition. However, for every element of the original matrix $A$ that is zero the corresponding elements in $L$ or $U$ is set to zero. This means that the product of $LU$ will contain more nonzero diagonals than the original matrix $A$. Therefore the matrix $K$ must contain these extra diagonals as well if Eq. (6.2) is to hold.

Stone reasoned that if the equations approximate an elliptic partial differential equation the solution can be expected to be smooth. This means that the unknowns corresponding to the extra diagonals can be approximated by interpolation of the surrounding points. By allowing $K$ to have more non zero entries on all seven diagonals and using the interpolation mentioned above the SIP method constructs an LU factorization with the property that for a given approximate solution $\phi$ the product $K\phi \approx 0$ and thus the iteration matrix $M$

is close to $A$ by relation (6.2).

To solve the system of equations the following iterations is performed, starting with an initial guess for the wave action vector $\vec{N}^0$ an iteration is performed solving:

$$U\,\vec{N}^{s+1} = L^{-1}\,K\,\vec{N}^s + L^{-1}\,\vec{b} \qquad (6.3)$$

Since the matrix $U$ is upper triangular this equation is efficiently solved by back substitution. An essential property which makes the method feasible is that the matrix $L$ is easily invertible. This iterative process is repeated $s = 0, 1, 2, ...$ until convergence is reached.

## 6.2   Successive Over Relaxation (SOR) technique

This section is under preparation. See also Botta and Ellenbroek (1985).

# Chapter 7

# Parallel implementation aspects

Domain decomposition methods have been successfully used for solving large sparse systems arising from finite difference or finite volume methods in computational fluid dynamics on distributed memory platforms. They are based, in essence, upon a partition of the whole computational domain in $\vec{x}$-space into a number of contiguous, non-overlapping subdomains with each of them being assigned to a different processor. In this case the same algorithm performs on all available processors and on its own set of data (known as the SPMD programming model). Each subdomain can have multiple neighbors on each of its four sides. For this, a data structure is implemented to store all the information about the relationship of the subdomain and its particular neighbors. Next, each subdomain, look in isolation, is then surrounded by an auxiliary layer of one to three grid points originating from neighbouring subdomains. This layer is used to store the so-called halo data from neighbouring subdomains that are needed for the solution within the subdomain in question. The choice of one, two or three grid points depends on the use of propagation scheme in geographical space, i.e., respectively, BSBT, SORDUP or Stelling/Leendertse. Since, each processor needs data that resides in other neighbouring subdomains, exchange of data across boundaries of subdomains is necessary. Moreover, to evaluate the stopping criterion (3.22), global communication is required. These message passings are implemented by a high level communication library such as MPI standard. A popular distribution is MPICH which is free software[1] and is used in the present study. Only simple point-to-point and collective communications have been employed. There are, however, some other implementation and algorithmic issues that need to be addressed.

## 7.1   Load balancing

The mapping of subdomains on processors should be chosen so as to distribute the computational load as equally as possible and to minimize the communication cost. Intuitively, it will be clear that we have to allocate contiguous blocks of equal numbers of grid points on each processor. However, in the context of SWAN applications to coastal areas, some dif-

---

[1]Available from *http://www-unix.mcs.anl.gov/mpi/mpich*.

ficulties arise. Firstly, wet and dry grid points may unevenly distributed over subdomains while no computations have to be done in dry points. Secondly, an unbalanced partition may arise during the simulation due to the tidal effect (dry points become wet and vice versa). In such a case, one may decide to adapt the partition such that it is balanced again (so-called dynamic load balancing). Finally, most end-users are not willing to determine the partitioning themselves, thus automatic support for partitioning the grids is desirable.

In the present study, two well-established partition methods are applied. The first is called stripwise partitioning in which the computational grid is cut along one direction, resulting in horizontal or vertical strips. The choice of cutting direction depends on the interface size of the strips which should be minimized. However, the communication volume, which is related to the total size of the interfaces, can be further reduced by means of recursive application of alternately horizontal and vertical bisection. This is known as Recursive Co-ordinate Bisection (RCB). Further details on these techniques and an overview on grid partitioning can be found, e.g. in Fox (1988) and Chrisochoides *et al.* (1994). .

Within SWAN, the grid partitioning is carried out automatically on wet grid points only. The size of the subdomain equals the total number of wet points divided by the total number of subdomains. The implementation of a stripwise partitioning is as follows. First, an empty strip is created. Next, assign point-by-point to the created part until the size of that part has been reached. Thereafter, verify whether non-assigning wet points remain in the current strip. If so, these points will be assign to the same part too, otherwise create next empty strip. As a result, all strips have straight interfaces and include approximately the same number of wet grid points. Moreover, experiences with SWAN simulation have shown that the amount of computations in each wet grid point remains more or less constant during the simulation and hence, there is no need for dynamic load balancing.

A final remark has to be made considering grid partitioning. The above described methodology does not seem to have been implemented in spectral wave models before. In Tolman (20020, another way of distributing data over the processors is discussed: each $p^{\text{th}}$ wet grid point is assign to the same processor with $p$ the total number of processors. The requirement of equal numbers of wet grid points per processor is provided automatically. However, it is impossible to compute the spatial wave propagation in an effective manner. The only alternative is to gather data for all grid points in a single processor before the calculation is performed. This will require a full data transpose, i.e. rearranging data distribution over separate processors. It is believed that this technique requires much more communication between processors than domain decomposition and therefore less suitable for SWAN.

## 7.2   Parallelization of implicit propagation schemes

Contrary to explicit schemes, implicit ones are more difficult to parallelize, because of the coupling introduced at subdomain interfaces. For example, concerning the four-sweep

technique, during the first sweep, an update of $N(i, j, l, m)$ can be carried out as soon as $N(i - 1, j, l, m)$ and $N(i, j - 1, l, m)$ have been updated and thus it can not be performed in parallel. Parallelization of this implicit scheme requires modifications. Ideally, the parallel algorithm need no more computing operations than the sequential one for the same accuracy.

The simplest strategy to circumvent this problem consists in treating the data on subdomain interfaces explicitly, which in mathematical terms amounts to using a block Jacobi approximation of the implicit operator. In this context, we employ the RCB partition method, since it gives the required balanced, low-communication partitioning. This strategy possess a high degree of parallelism, but may lead to a certain degradation of convergence properties. However, this numerical overhead can be reduced by colouring the subdomains with four different colors and subsequently permuting the numbering of unknowns in four sweeps in accordance with the color of subdomains. Furthermore, each subdomain is surrounded by subblocks of different colors. See Figure 7.1. As a result, each coloured subdomain start with a different ordering of updates within the same sweep and
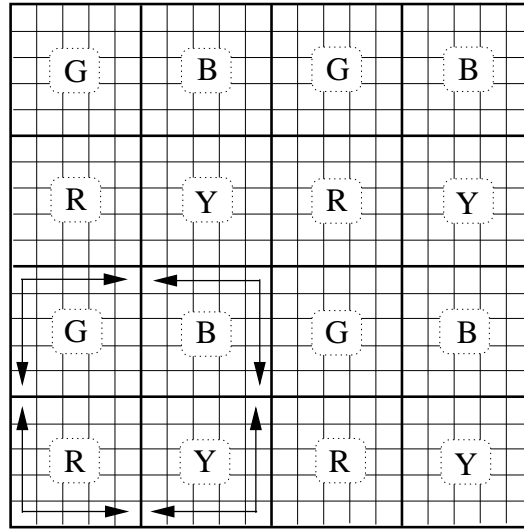


Figure 7.1: Four types of subblocks (red, yellow, green and black) treated differently with respect to the ordering of updates (indicated by arrows) per sweep.

thus reducing the number of synchronization points. This multicolor ordering technique has been proposed earlier, e.g. in Meurant (1988) and Van der Vorst (1989).

Another strategy is based on the ideas proposed by Bastian and Horton (1991) and is referred here to as the block wavefront approach. It is demonstrated with the following example. First, we decompose the computational domain into a number of strips. In this example, we assume that these strips are parallel to $y-$axis. Next, we start with the first sweep. The processor belonging to the first strip updates the unknowns $N(i, 1, l, m)$ along the first row $j = 1$. Thereafter, communication takes place between this processor and

processor for strip 2. The unknowns $N(i, 2, l, m)$ along $j = 2$ in strip 1 and $N(i, 1, l, m)$ along $j = 1$ in strip 2 can be updated in parallel, and so on. After some start-up time all processors are busy. This is depicted in Figure 7.2. Finally, this process is repeated for the
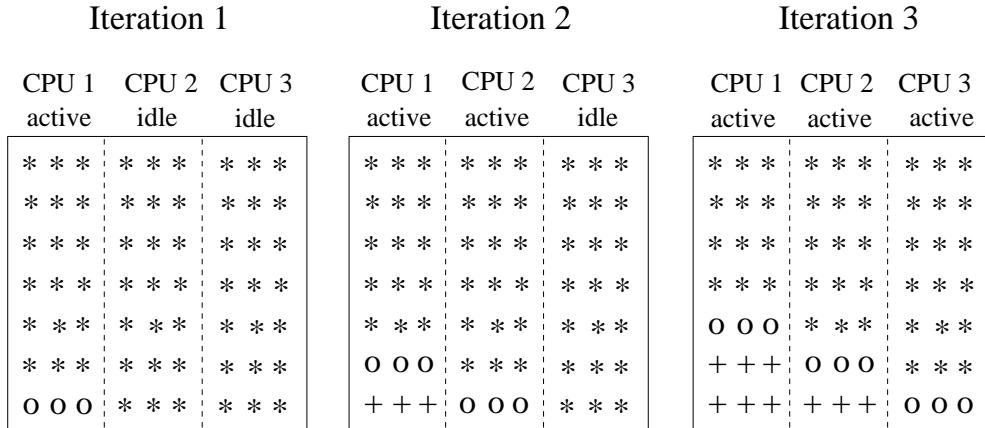
| Iteration 1 | | | Iteration 2 | | | Iteration 3 | | |
|---|---|---|---|---|---|---|---|---|
| CPU 1 | CPU 2 | CPU 3 | CPU 1 | CPU 2 | CPU 3 | CPU 1 | CPU 2 | CPU 3 |
| active | idle | idle | active | active | idle | active | active | active |
| * * * | * * * | * * * | * * * | * * * | * * * | * * * | * * * | * * * |
| * * * | * * * | * * * | * * * | * * * | * * * | * * * | * * * | * * * |
| * * * | * * * | * * * | * * * | * * * | * * * | * * * | * * * | * * * |
| * * * | * * * | * * * | * * * | * * * | * * * | * * * | * * * | * * * |
| * ** | * ** | * ** | * ** | * ** | * ** | o o o | * ** | * ** |
| * ** | * * * | * * * | o o o | * * * | * * * | + + + | o o o | * ** |
| o o o | * * * | * * * | + + + | o o o | * * * | + + + | + + + | o o o |

Figure 7.2: Application of block wavefront approach for the first 3 iterations during the first sweep. Domain is divided into 3 vertical strips. Stars represent unknowns to be updated, circles mean that unknowns are currently updated and the plus signs indicate unknowns that have been updated.

other three sweeps. Details can be found in the source code of SWAN. The block wavefront approach does not alter the order of computing operations of the sequential algorithm and thus preserving the convergence properties, but reduces parallel efficiency to a lesser extent because of the serial start-up and shut-down phases (Amdahl's law). This technique resembles much to the standard wavefront technique applied in a pointwise manner (unknowns on a diagonal are mutually independent and thus can be updated in parallel; for details, see Templates (1994), which has also been employed by Campbell *et al.* (2002) for parallelizing SWAN using OpenMP.

The performance of the two discussed parallelization methods applied in the SWAN model has been discussed in (Zijlema, 2005). Numerical experiments have been run on a dedicated Beowulf cluster with a real-life application. They show that good speedups have been achieved with the block wavefront approach, as long as the computational domain is not divided into too thin slices. Moreover, it appears that this technique is sufficiently scalable. Concerning the block Jacobi method, a considerable decline in performance has been observed which is attributable to the numerical overhead arising from doubling the number of iterations due to the relative weak stopping criteria as described in Section 3.3. Furthermore, it may result in a solution that is computed to an accuracy that may not be realistic. In conclusion, parallelization with the block wavefront technique has been favoured and has been implemented in the current operational version of SWAN.

Since version 41.10 it is possible to employ the block Jacobi approach instead of the wave-

front technique as an alternative (see the Implementation Manual how to activate this approach). The user is however advised to apply the curvature-based termination criterion, as described in Section 3.4. This will enhance the scalability significantly. This is especially the case when the user runs a (quasi-)nonstationary simulation.

A survey of other alternatives to the parallelization of the implicit schemes is given in Templates (1994).

# Chapter 8

# Unstructured mesh implementation

Since, the characteristic spatial scales of the wind waves propagating from deep to shallow waters are very diverse, a flexible grid would be required to allow local refinement of the mesh in areas of interest e.g., regions of strong bathymetry variations in estuaries and fjords, without incurring overhead associated with grid adaptation at some distance offshore. Traditionally, this can be achieved by employing a nesting technique. Although, this practise is very common for SWAN, it is generally recognized that this may lead to complicated programming with the corresponding significant increase in computational effort.

The use of unstructured grids, however, offers a good alternative to nested models not only because of the ease of local grid refinement, either adaptive or fixed, but also the high flexibility to generate grids along coastline and around islands. The variable mesh is especially useful in coastal regions where the water depth varies greatly. Thus, the variable grid gives the highest resolution where it is most needed. Moreover, this can be automated to a large extent. Although, the CPU cost per grid point is often relative higher than cases with structured grids, this effect is probably more than offset by the reduction in the number of grid points.

This chapter presents an unstructured grid procedure for SWAN. Details can also be found in (Zijlema, 2009, 2010). The numerical propagation scheme for structured grids is based on a four-direction Gauss-Seidel iteration technique and is accompanied by a fully implicit temporal discretization; see Section 3.3. Hence, SWAN is stable for any time step. Because of this nice property, this solution technique is tailored to unstructured grids.

## 8.1 Description of an unstructured grid

### 8.1.1 Definitions

We distinguish between two types of grids, namely structured and unstructured grids. A two-dimensional structured grid may contain quadrilaterals. These can be rectilinear or

curvilinear. The number of cells that meet each other in an internal vertex is always 4. In unstructured meshes this restriction is abandoned. Moreover, 2D unstructured grids usually consist of triangles or a combination of triangles and quadrilaterals, a so-called hybrid grid. The unstructured meshes that we consider in SWAN consist solely of triangles, also called cells. The edges of the triangles are called faces.

## 8.1.2   Relations between number of cells, vertices and faces

For a two-dimensional triangular mesh, the number of cells $C$, the number of boundary faces $E_b$ and internal faces $E_i$ are related according to:

$$E_b + 2E_i = 3C \tag{8.1}$$

The total number of faces $E = E_i + E_b$. With $V$ the number of vertices and $H$ the number of holes ('islands'), we have the following Euler's relation for a triangulation:

$$C + V - E = 1 - H \tag{8.2}$$

Usually, $E_b << E_i$ and the number of holes $H$ is negligibly small, so

$$C \approx 2V, \quad E \approx 3V \tag{8.3}$$

There are approximately twice as many cells as vertices in a triangular mesh. Therefore, it is an optimal choice to locate the action density in vertices as the number of unknowns is minimal on a given grid. Concerning the time-consuming evaluation of the physical processes representing the wave energy generation, dissipation and redistribution, this allows SWAN to save a considerable amount of computing time.

## 8.1.3   Conditions imposed to the grid

In order to avoid badly shaped grids, the grids must satisfy the following properties:

- The number of cells that meet at each vertex in the interior of the mesh must be at least 4 and at most 10.

- The angles inside each triangle must be smaller than a certain value. Let $\vec{a}$ and $\vec{b}$ be the tangential vectors of two faces of a triangle, then the angle $\phi$ between these two faces equals

$$\cos \phi = \frac{\vec{a} \cdot \vec{b}}{|\vec{a}||\vec{b}|} \tag{8.4}$$

   For safety, we do not allow for angles with $\cos \phi < -0.8$ or, equivalently, $\phi > 143^o$.

## 8.2   Some notes on grid generation

We briefly outline some issues related to grid generation from a practical point of view. The process of grid generation can be difficult and time consuming. A common approach is proceeding from coarse to fine grid through refinement in various ways. Generally, one would like to have an optimal grid in which areas where the bathymetry or evolution of the waves change rapidly require a higher resolution than areas where the physics or depth changes less. This goes around by having an indication how to determine the refinement based on bathymetry or geometric variations through preliminary evaluations. To facilitate this procedure, many user-friendly mesh generation packages are available on the Internet. In addition, there are public-domain, graphical Matlab and Python interfaces to Triangle (Shewchuk, 1996). Triangle is a freely-distributed, two-dimensional Delaunay triangulator and is widely utilized.

An important key ingredient for the preparation of the grid for the wave model domain is bathymetry data. Boundary nodes, segments and holes can be created from this data with the use of the mesh editing options of a mesh generation package. After checking and improving grid quality, the final information on nodes and segments is forced into the triangulation of the domain. This triangulation includes only acute triangles.

A good grid generator provides many pre-defined depth-dependent contraints for further mesh refinement. From a numerical point of view, mesh refinement is often directly related to properly resolve the shape of the wave, i.e. to keep the wavelength to grid size ratio relatively large. When wavelength decreases in shallower water, the grid size must decrease as well. Therefore, this criterion, called the $h$-refinement, has the effect of using smaller cells in shallow water and larger cells in deeper water. Here, $h$ refers to the water depth. Another useful criterion is known as the topographic length scale constraint, when one try to keep the ratio $\Delta h/h$ less than one. Here, $\Delta h$ equals the difference between the maximum depth of a triangle and the minimum depth and $h$ is the average depth. This criterion addresses the bathymetric slope and cells with a high value of $\Delta h/h$ indicate areas of steep bottom topography that will need to be more finely resolved. When refining the grid, one must balance the need to fully meet the refinement criteria with the desire to keep the triangle sizes from becoming too small. Thus, these criteria are generally imposed along with a minimum area constraint. The refinement process is repeated iteratively until a final grid with the appropriate resolution is obtained.

## 8.3   Numerical method

### 8.3.1   Discretization procedure

For the sake of clarity of the algorithm description below, we put all the terms but the time derivative and propagation term in the geographical space of Eq. (2.16) in one term

$F(\vec{x}, \sigma, \theta)$:

$$\frac{\partial N}{\partial t} + \nabla_{\vec{x}} \cdot [\vec{c}_{\vec{x}} N] = F \tag{8.5}$$

with $\vec{c}_{\vec{x}} = \vec{c}_g + \vec{U}$ the geographic velocity vector.

For the time being, we restrict ourselves to triangular meshes. However, other type of meshes can be employed as well, e.g. hybrid grids (consisting of both triangles and quadrilaterals). We consider a triangulation of a geographical domain in which Eq. (8.5) is solved; see Fig 8.1. Every vertex and all the triangles around this vertex are taken into
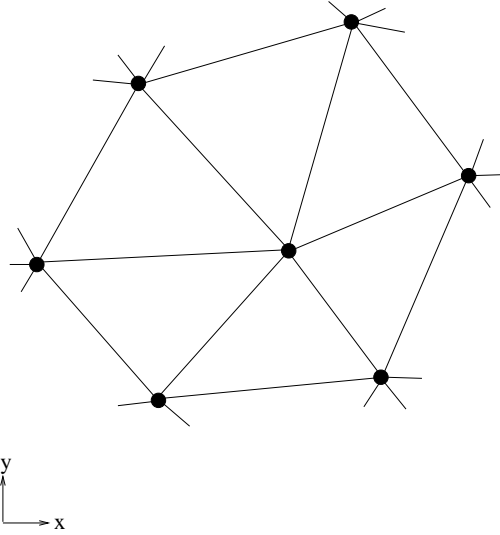


Figure 8.1: An example of triangulation.

account. Observe that the number of cells around a vertex can be different for all vertices. A vertex-based scheme is used in which the wave action $N$ is stored at the vertices and Eq. (8.5) is solved in each vertex. We note that the values at boundary vertices are fixed during the computation.

For the time integration, we adopt the first order implicit Euler scheme, as follows

$$\frac{N^n - N^{n-1}}{\Delta t} + \nabla_{\vec{x}} \cdot [\vec{c}_{\vec{x}} N^n] = F^n \tag{8.6}$$

where $\Delta t$ is the time step and $n$ is the time step counter. The main property of this approximation is that it does not suffer from the stability restriction imposed by the CFL condition inherent in the explicit methods as employed in most spectral models. In principle, the time step is limited only by the desired temporal accuracy. This procedure, however, involves the solution of a large system of equations.

A point-by-point multi-directional Gauss-Seidel iteration technique is employed for updating all grid vertices. A key feature of this technique is that it takes advantage of the newly

acquired vertex values during an iteration. It is locally implicit but globally explicit. In other words, it circumvents the need to build or store large matrices and remains stable at any time steps. This means that this numerical procedure can converge to steady state much more rapidly than explicit methods without requiring too much computational work and memory as do implicit methods.

We consider the update of a vertex as labeled 1 in Figure 8.2. This involves looping over each cell of this vertex. We want to find an approximation for the propagation term of



○ = not updated
● = to be updated
● = updated
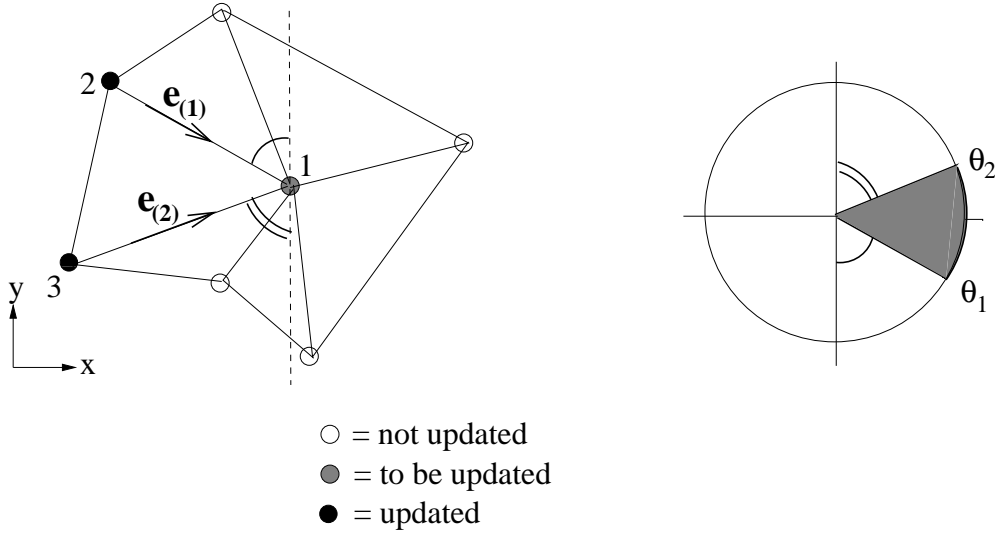
Figure 8.2: Update of the wave action at vertex 1 in a triangle △123 and the shaded directional sector in spectral space for which the waves are propagated.

Eq. (8.6). To this end, we employ some vector calculus. We consider a triangular cell as depicted in Figure 8.3. In vertex 1, we apply a mapping from a local coordinate system $\vec{\xi}$ = $(\xi, \eta)$ to the Cartesian one $\vec{x} = (x, y)$. Based on this transformation $\vec{x}(\vec{\xi})$, we have the following base vectors that are tangential to the coordinate lines $\xi$ and $\eta$, respectively,

$$\vec{e}_{(1)} = \frac{\partial \vec{x}}{\partial \xi}, \quad \vec{e}_{(2)} = \frac{\partial \vec{x}}{\partial \eta}. \tag{8.7}$$

The vectors

$$\vec{e}^{(1)} = \operatorname{grad} \xi, \quad \vec{e}^{(2)} = \operatorname{grad} \eta \tag{8.8}$$

are normal to the coordinate surface of constant $\xi$ and $\eta$, respectively (see Figure 8.3). Moreover, they are reciprocal to the base vectors, i.e.

$$\vec{e}_{(\alpha)} \cdot \vec{e}^{(\beta)} = \delta_\alpha^\beta, \quad \alpha, \beta = \{1, 2\}, \tag{8.9}$$

where $\delta_\alpha^\beta$ is Kronecker delta (which is unity if $\alpha = \beta$, and zero otherwise). Using Cramer's rule, one can find

$$\vec{e}^{(1)} = \frac{1}{D}(e_{(2)}^2, -e_{(2)}^1)^\top, \quad \vec{e}^{(2)} = \frac{1}{D}(-e_{(1)}^2, e_{(1)}^1)^\top, \quad D = e_{(2)}^2 e_{(1)}^1 - e_{(1)}^2 e_{(2)}^1. \tag{8.10}$$
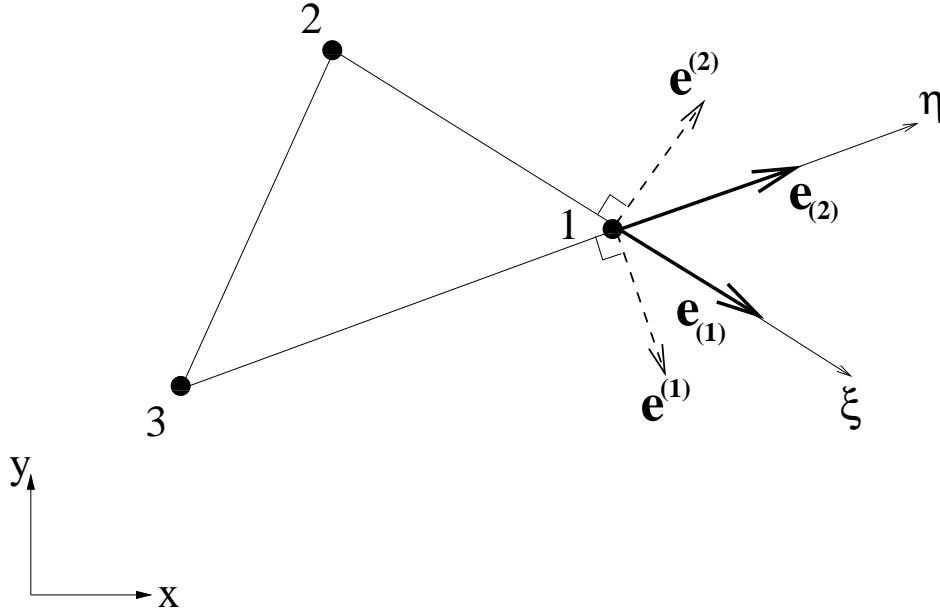
Figure 8.3: A triangular cell with geometrical quantities used for discretization in geographical space. Definitions of these quantities are provided in the text.

Next, we expand the propagation term of Eq. (8.6):

$$\nabla_{\vec{x}} \cdot [\vec{c}_{\vec{x}} N] = \frac{\partial c_x N}{\partial x} + \frac{\partial c_y N}{\partial y} , \qquad (8.11)$$

where $c_x$ and $c_y$ are the $x-$ and $y-$components of the wave propagation vector $\vec{c}_{\vec{x}}$, respectively. Using the chain rule, we obtain

$$\nabla_{\vec{x}} \cdot [\vec{c}_{\vec{x}} N] = e_1^{(1)} \frac{\partial c_x N}{\partial \xi} + e_1^{(2)} \frac{\partial c_x N}{\partial \eta} + e_2^{(1)} \frac{\partial c_y N}{\partial \xi} + e_2^{(2)} \frac{\partial c_y N}{\partial \eta} . \qquad (8.12)$$

Further, we approximate the derivatives in Eq. (8.12). The most simplest one is a one-sided first order difference scheme, as follows

$$\frac{\partial c_x N}{\partial \xi} \approx \frac{c_x N_1 - c_x N_2}{\Delta \xi} , \quad \frac{\partial c_x N}{\partial \eta} \approx \frac{c_x N_1 - c_x N_3}{\Delta \eta} ,$$

$$\frac{\partial c_y N}{\partial \xi} \approx \frac{c_y N_1 - c_y N_2}{\Delta \xi} , \quad \frac{\partial c_y N}{\partial \eta} \approx \frac{c_y N_1 - c_y N_3}{\Delta \eta} , \qquad (8.13)$$

where the action densities at vertices 1, 2 and 3 are denoted by $N_1$, $N_2$ and $N_3$, respectively. Here, we choose the mapping $\vec{x}(\vec{\xi})$ such that $\Delta \xi = \Delta \eta = 1$. The approximation is completed by substituting (8.13) in (8.12):

$$\nabla_{\vec{x}} \cdot [\vec{c}_{\vec{x}} N] \approx c_x N|_2^1 e_1^{(1)} + c_x N|_3^1 e_1^{(2)} + c_y N|_2^1 e_2^{(1)} + c_y N|_3^1 e_2^{(2)} . \qquad (8.14)$$

Note that the components of the vectors $\vec{e}^{(1)}$ and $\vec{e}^{(2)}$ in Eq. (8.14) are given by Eqs. (8.10), while the base vectors are calculated according to

$$\vec{e}_{(1)} = \vec{x}_1 - \vec{x}_2, \quad \vec{e}_{(2)} = \vec{x}_1 - \vec{x}_3 \tag{8.15}$$

with $\vec{x}_i = (x_i, y_i)$ the position vector of vertex $i$ in a Cartesian coordinate system. This space discretization is of lowest order accurate and conserves action (see Section 8.7).

The upwind difference scheme BSBT (8.14) is employed for three reasons. First, it is compact, i.e. operating on one triangle only. Second, it enforces the propagation of wave action to follow the characteristics. Hence, this scheme produces numerical diffusion along these characteristics, and as such, it is multidimensional with a minimum amount of cross-diffusion. Third, it is monotone, i.e. guaranteeing $N > 0$ everywhere. This finite difference BSBT scheme appears to be identical to the well-known N(arrow) scheme, based on the fluctuation splitting method, on regular, triangular grids obtained from triangulation of rectangles with diagonals aligning with the wave characteristic as much as possible (see Struijs, 1994, pp. 63-64). Hence, the BSBT scheme share with the N scheme in many respects: it is multidimensional, first order accurate, optimal in terms of cross-diffusion, monotone, conservative, narrow stencil and consistent with local wave characteristics (see Section 3.2.1), but they are not identical in general.

Given the action densities $N_2^n$ and $N_3^n$ at vertices 2 and 3 of triangle $\triangle 123$, the wave action in vertex 1 is readily determined according to

$$\left[ \frac{1}{\Delta t} + c_{x,1} \left( e_1^{(1)} + e_1^{(2)} \right) + c_{y,1} \left( e_2^{(1)} + e_2^{(2)} \right) \right] N_1^n =$$

$$\frac{N_1^{n-1}}{\Delta t} + \left( c_{x,2} e_1^{(1)} + c_{y,2} e_2^{(1)} \right) N_2^n + \left( c_{x,3} e_1^{(2)} + c_{y,3} e_2^{(2)} \right) N_3^n + F^n . \tag{8.16}$$

The wave directions between faces $\vec{e}_{(1)}$ and $\vec{e}_{(2)}$ enclose all wave energy propagation in between the corresponding directions $\theta_1$ and $\theta_2$ as indicated as a shaded sector in Figure 8.2. This sector is the domain of dependence of Eq. (8.16) in vertex 1. Since, the wave characteristics lie within this directional sector, this ensures that the CFL number used will properly capture the propagation of wave action towards vertex 1. So, propagation is in line with the causality principle and is not subjected to a CFL stability criterion. Next, the term $F^n$ in Eq. (8.16) is discretized implicitly in the sector considered. Since the approximation in the spectral space and the linearization of the source terms are well explained in Section 3.3, we shall not pursue them any further. Eq. (8.16) constitute a coupled set of linear, algebraic equations for all spectral bins within the sector considered at vertex 1. The solution is found by means of an iterative solver; see Section 3.3 for details.

The update of vertex 1 is completed when all surrounding cells have been treated. This allows waves to transmit from all directions. Due to refraction and nonlinear interactions, wave energy shifts in the spectral space from one directional sector to another. This is taken into account properly by repeating the whole procedure with converging results.

## 8.3.2   The sweeping algorithm

The solution of each vertex must be updated geographically before proceeding to the next one. For example, referring to Figure 8.2, the value in vertex 1 is determined by its two upwave vertices 2 and 3 only if they are already updated. In this way causality can be preserved. For regular grids, the four-sweep scheme based on a four-direction Gauss-Seidel relaxation is employed as outlined in Section 3.3. The grid points are ordered in a natural manner, e.g. left to right and bottom to top during the first sweep, right to left and bottom to top during the second sweep, and so on. Hence, the updated values will be used immediately for updating the next unknown. However, in an unstructured mesh there are no distinct directions. Thus the vertices are ordered by their numbering which for an unstructured grid are quite random. As a consequence, the latest obtained solution will not necessarily be used for updating surrounding vertices. Also, we select wave directions in every triangular cell around a vertex for an update in spectral space. This selection differs for each vertex.

An ordering is proposed such that the solution of each vertex will tend to ensure that updated values from the surrounding vertices are used as soon as they are available. This ordering of vertices is perpendicular to the main wave direction and thus along the wave crests. Usually, the main wave direction is the direction of the incoming wave energy on the imposed boundary or the wind direction. All the vertices are ordered according to their distances to the origin of the grid in ascending order. It is expected that this so-called crest ordering, by which we update along wave characteristics as much as possible, should result in a faster convergence than a random ordering of vertices. This ordering is usually fine for wind waves or swells propagating along rather straight wave characteristics. However, it might be less efficient in case of waves propagated along (strong) curved wave rays (e.g. around islands). In that case the iteration process is not effectively Gauss-Seidel. Like the structured grid case, a fixed number of sweeps (not necessarily 4) is introduced. Each sweep represents a range of wave directions that is equal to $2\pi$ divided by the number of sweeps. As an illustrative example we choose 3 sweeps of each $120^o$. For each sweep the vertices are ordered in line with the corresponding sweep direction. The first sweep direction is the dominant wave direction, the second one equals the first one plus $120^o$ and the last one equals the first one minus $120^o$. Hence, we have three different ordering of vertices. This will speed up the iteration process because propagation of wave energy in other directions is covered as well. In general, the higher the number of sweeps, the smaller the directional interval, the better the wave energy in various directions is captured in one series of sweeps, the lesser the number of required iterations to obtain the steady-state convergence (see also Section 3.5). However, by enhancing the number of sweeps, the amount of computations will be increased as well and thus more computing intensive. Experiences have shown that three sweeps is a good compromise between the reduced number of iterations and the extended amount of required computation time.

An algorithm is employed that consists of simply proceeding through a list of vertices per sweep that remain to be updated. This list is sorted according to the ascending distances

of vertices to the origin of the grid in line with the sweep direction. This algorithm goes along with an iteration process. Initially, all vertices are non-updated in both geographic and spectral spaces. In each iteration, a number of sweeps through the vertices is executed, while the solution of each vertex must be updated geographically before proceeding to the next one. The two upwave faces connecting the vertex to be updated enclose those wave directions that can be processed in the spectral space; see Figure 8.2. The solution of each cell having a vertex as one of their vertices and (partly) enclosed by the present sweep must be updated. The vertex is updated when all cells around this vertex have been considered. As such, all wave directions can be covered efficiently. The process continues with the next vertex in the list of non-updated vertices. A sweep is complete when all vertices are updated geographically (but not necessarily in whole spectral space, e.g. due to refraction and quadruplets). An iteration is complete when all sweeps have been carried out and so all vertices are updated in both geographic and spectral spaces so that wave energy from all directions has been propagated through geographical space. This numerical process is iterated until an *a priori* convergence condition is satisfied. Here, the curvature-based stopping criteria as outlined in Section 3.4 will be applied. The total number of iterations depends mainly on local change in propagation direction due to bed changes and ambient current, and possibly also on the domain size. See also Section 3.4 for further details.

## 8.4 Interpolation at user-defined locations

All the quantities deals with in SWAN are located at the vertices. Hence, due to the user-defined locations of the wave parameters, interpolations are required. Let parameter $\varphi_j = \varphi(\vec{x}_j)$ and Cartesian coordinates $\vec{x}_j = (x_j, y_j)$, with $j \in \{1, 2, 3\}$ indicating the vertices of cell $i$, be given. The vertices 1, 2 and 3 are ordered in a counterclockwise direction, see Figure 8.2. The associated 3 edges are denoted as 12, 23 and 31.

Linear interpolation, with $\vec{x}_0$ inside cell $i$ and $\varphi_0 = \varphi(\vec{x}_0)$, is given by

$$\varphi(\vec{x}) = \varphi_0 + \nabla\varphi \cdot (\vec{x} - \vec{x}_0) \tag{8.17}$$

where $\nabla\varphi$ is a constant vector inside cell $i$. We apply Green-Gauss reconstruction, i.e.,

$$\nabla\varphi \approx \frac{1}{A_i} \int_{\triangle i} \nabla\varphi d\Omega = \frac{1}{A_i} \oint_{\partial\triangle i} \varphi\vec{n} d\Gamma \approx \frac{1}{A_i} \sum_e \varphi_e \vec{n}_e \tag{8.18}$$

where $A_i$ is the area of cell $i$ and the summation runs over the 3 edges $e \in \{12, 23, 31\}$ of cell $i$. The values $\varphi_e$ at edges are taken as averages:

$$\varphi_{12} = \frac{1}{2}(\varphi_1 + \varphi_2), \quad \varphi_{23} = \frac{1}{2}(\varphi_2 + \varphi_3), \quad \varphi_{31} = \frac{1}{2}(\varphi_3 + \varphi_1) \tag{8.19}$$

Furthermore, $\vec{n}_e$ is the outward pointing normal at edge $e$ and is obtained by rotating the edge over $90^o$ in the clockwise direction. Hence,

$$\vec{n}_{12} = R\vec{t}_{12}, \quad R = \begin{pmatrix} 0 & 1 \\ -1 & 0 \end{pmatrix}, \quad \vec{t}_{12} = \vec{x}_2 - \vec{x}_1 \tag{8.20}$$

We also need the following identity

$$\vec{n}_{12} + \vec{n}_{23} + \vec{n}_{31} = 0 \tag{8.21}$$

It is not difficult to show that

$$\begin{aligned}
\nabla\varphi &= \frac{1}{2A_i}[\vec{n}_{12}(\varphi_1 - \varphi_3) + \vec{n}_{31}(\varphi_1 - \varphi_2)] \\
&= -\frac{1}{2A_i}[\varphi_1\vec{n}_{23} + \varphi_2\vec{n}_{31} + \varphi_3\vec{n}_{12}]
\end{aligned} \tag{8.22}$$

or

$$\frac{\partial\varphi}{\partial x} = \frac{1}{2A_i}[\varphi_1(y_2 - y_3) + \varphi_2(y_3 - y_1) + \varphi_3(y_1 - y_2)] \tag{8.23}$$

and

$$\frac{\partial\varphi}{\partial y} = \frac{1}{2A_i}[\varphi_1(x_3 - x_2) + \varphi_2(x_1 - x_3) + \varphi_3(x_2 - x_1)] \tag{8.24}$$

The area $A_i$ of cell $i$ is given by $|\vec{t}_{12} \cdot \vec{n}_{13}|/2$. Hence, with

$$\vec{n}_{13} = R\vec{t}_{13} = \begin{pmatrix} y_3 - y_1 \\ x_1 - x_3 \end{pmatrix} \tag{8.25}$$

we have

$$A_i = \frac{1}{2}|(x_2 - x_1)(y_3 - y_1) - (x_3 - x_1)(y_2 - y_1)| \tag{8.26}$$

Alternatively, we may interpolate using the following relation

$$\varphi(\vec{x}) = \sum_k \varphi_k \lambda_k(\vec{x}) = \varphi_1\lambda_1 + \varphi_2\lambda_2 + \varphi_3\lambda_3 \tag{8.27}$$

where $\lambda_k$ is a linear shape function with the following properties:

1. $\lambda_k$ is linear per cell and

2. $\lambda_k(\vec{x}_j) = \delta_{kj}$ with $\delta_{kj}$ is the Kronecker delta.

We choose the following shape function

$$\lambda_k(\vec{x}) = a_0^k + a_x^k x + a_y^k y \tag{8.28}$$

and the coefficients $a$ follow from solving

$$\begin{pmatrix} 1 & x_1 & y_1 \\ 1 & x_2 & y_2 \\ 1 & x_3 & y_3 \end{pmatrix} \begin{pmatrix} a_0^1 & a_0^2 & a_0^3 \\ a_x^1 & a_x^2 & a_x^3 \\ a_y^1 & a_y^2 & a_y^3 \end{pmatrix} = \begin{pmatrix} 1 & 0 & 0 \\ 0 & 1 & 0 \\ 0 & 0 & 1 \end{pmatrix} \tag{8.29}$$

## 8.5   Computation of wave-induced force

`FORCE` is the wave-driven stress, i.e. the force per unit surface driving the wave-driven current, expressed in N/m², is defined as the gradient of the radiation stresses:

$$S_{xx} = \rho g \int \lfloor n \cos^2 \theta + n - \frac{1}{2} \rfloor E d\sigma d\theta \tag{8.30}$$

$$S_{xy} = S_{yx} = \rho g \int n \sin \theta \cos \theta E d\sigma d\theta \tag{8.31}$$

$$S_{yy} = \rho g \int \lfloor n \sin^2 \theta + n - \frac{1}{2} \rfloor E d\sigma d\theta \tag{8.32}$$

with $n$ the ratio of group velocity and phase velocity. The force is then

$$F_x = -\frac{\partial S_{xx}}{\partial x} - \frac{\partial S_{xy}}{\partial y} \tag{8.33}$$

and

$$F_y = -\frac{\partial S_{yx}}{\partial x} - \frac{\partial S_{yy}}{\partial y} \tag{8.34}$$

In order to compute the force in all internal vertices of the unstructured mesh, we consider a control volume (CV) as depicted in Figure 8.4. This CV is called centroid dual and is
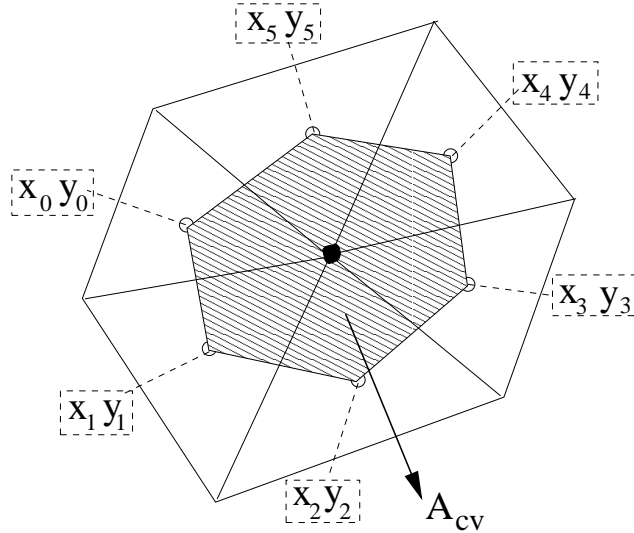


Figure 8.4: Control volume (centroid dual) of vertex is shaded. Some notation is introduced.

constructed by joining the centroids neighbouring the vertex under consideration. The set of CVs must fill the whole computational domain and must also be non-overlapping. In

the following we use the numbering from Figure 8.4. Let $\varphi$ be one of the radiation stresses $S_{xx}$, $S_{xy}$ and $S_{yy}$. The gradient of $\varphi$ is computed as follows:

$$\nabla\varphi \approx \frac{1}{A_{\text{CV}}} \sum_e \varphi_e \vec{n}_e \tag{8.35}$$

where $A_{\text{CV}}$ is the area of the CV and the summation runs over the associated edges $e$ of this CV. The values $\varphi_e$ at edges of the centroid dual are taken as averages, i.e. $(\varphi_0 + \varphi_1)/2$, $(\varphi_1 + \varphi_2)/2$, etc. Moreover, the value of the radiation stresses inside each triangle is simply the average of the radiation stresses in the associated vertices of the cell. Now, the derivatives of $\varphi$ inside CV are

$$\frac{\partial\varphi}{\partial x} = \frac{1}{2A_{\text{CV}}} \sum_{i=0}^{n-1} (\varphi_i + \varphi_{i+1})(y_{i+1} - y_i) \tag{8.36}$$

and

$$\frac{\partial\varphi}{\partial y} = \frac{1}{2A_{\text{CV}}} \sum_{i=0}^{n-1} (\varphi_i + \varphi_{i+1})(x_i - x_{i+1}) \tag{8.37}$$

with $n$ the number of surrounding cells of the considered vertex and $\varphi_n = \varphi_0$, $x_n = x_0$ and $y_n = y_0$. The area of the CV is given by

$$A_{\text{CV}} = \frac{1}{2} \sum_{i=0}^{n-1} (x_i\, y_{i+1} - x_{i+1}\, y_i) \tag{8.38}$$

## 8.6   Calculation of diffusion-like terms

There are situations in which the following diffusion-like term need to be computed on unstructured meshes:

$$\nabla \cdot (\kappa\nabla\varphi) \tag{8.39}$$

in vertices with $\kappa$ a space-varying diffusion coefficient (a tensor) and $\varphi$ a scalar defined in vertices. In SWAN, these are

- the alleviation of the garden-sprinkler effect; see Eq. (3.2.1), and

- the computation of the diffraction parameter; see Eq. (2.123).

We consider the centroid dual as shown in Figure 8.4. The calculation consists of 3 steps. First, we compute the gradient of $\varphi$ inside each surrounding cell using expressions (8.23) and (8.24). Next, this gradient is multiplied with the appropriate diffusion coefficient $\kappa$ as given in the centroid. Finally, we compute the gradient of $\kappa\nabla\varphi$ inside the CV according to Eqs. (8.36) and (8.37).

## 8.7  Conservation of action

In this section, we proof that the discretization Eq. (8.16) is energy conserving. For this, we assume stationarity and neglect the source terms, so $F = 0$. From Eq. (8.16), it follows

$$\vec{e}^{(1)} \cdot (\vec{c}_{\vec{x}} N)_1 + \vec{e}^{(2)} \cdot (\vec{c}_{\vec{x}} N)_1 = \vec{e}^{(1)} \cdot (\vec{c}_{\vec{x}} N)_2 + \vec{e}^{(2)} \cdot (\vec{c}_{\vec{x}} N)_3 \tag{8.40}$$

On the other hand, we have

$$\nabla \cdot (\vec{c}_{\vec{x}} N) = \frac{1}{\Omega} \oint \vec{c}_{\vec{x}} N \cdot \vec{n} d\Gamma \tag{8.41}$$

The vectors $\vec{c}_{\vec{x}} N$ at edges are taken as averages, and so (see Figure 8.3 for reference)

$$\begin{aligned} \nabla \cdot (\vec{c}_{\vec{x}} N) \quad \approx \quad & \frac{1}{2\Omega} [( (\vec{c}_{\vec{x}} N)_1 + (\vec{c}_{\vec{x}} N)_2 ) \cdot \vec{n}_{12} + \\ & ( (\vec{c}_{\vec{x}} N)_2 + (\vec{c}_{\vec{x}} N)_3 ) \cdot \vec{n}_{23} + ( (\vec{c}_{\vec{x}} N)_3 + (\vec{c}_{\vec{x}} N)_1 ) \cdot \vec{n}_{31}] \end{aligned} \tag{8.42}$$

Using the identity

$$\vec{n}_{23} = -\vec{n}_{12} - \vec{n}_{31} \tag{8.43}$$

and

$$\vec{n}_{12} = -\vec{e}^{(2)} , \quad \vec{n}_{31} = -\vec{e}^{(1)} \tag{8.44}$$

we have

$$\nabla \cdot (\vec{c}_{\vec{x}} N) \approx \frac{1}{2\Omega} [\vec{e}^{(1)} \cdot (\vec{c}_{\vec{x}} N)_1 + \vec{e}^{(2)} \cdot (\vec{c}_{\vec{x}} N)_1 - \vec{e}^{(1)} \cdot (\vec{c}_{\vec{x}} N)_2 - \vec{e}^{(2)} \cdot (\vec{c}_{\vec{x}} N)_3] = 0 \tag{8.45}$$

If the situation is stationary and there are no source terms then the divergence term is zero. Hence, the energy flux vector is divergence free. From this it follows that the closed integral of the flux normal to the faces of the triangle is zero, i.e. source free, if the compact BSBT scheme is applied. This also implies that the wave energy flux is constant along any wave characteristic in between faces $\vec{e}_{(1)}$ and $\vec{e}_{(2)}$ (see Figure 8.2 for reference). The BSBT scheme is thus consistent with local wave characteristics and can be viewed as a semi-Lagrangian scheme. This also holds for non-uniform depth and ambient current. Note that energy flux conservation is the one that really matters. (Energy flux conservation implies conservation of wave action, whereas the opposite is not always true .) In addition, the energy flux must remain constant along a wave ray (see e.g. Whitham (1974), pg. 245), particularly when ocean beds are steep, in order to describe the correct enhancement of local wave energy (shoaling). This can be ensured easily using semi-Lagrangian schemes like the BSBT one.

# Chapter 9

# The overall solution algorithm

This chapter is under preparation.

# Bibliography

[1] Abreu, M., A. Larraza and E. Thornton, 1992: Nonlinear transformation of directional wave spectra in shallow water, *J. Geophys. Res.*, **97**, 15579-15589

[2] Alves, J.H.G.M. and M.L. Banner, 2003: Performance of a saturation-based dissipation-rate source term in modelling the fetch-limited evolution of wind waves, *J. Phys. Oceanogr.*, **33**, 1274-1298

[3] Arcilla, A.S. and C.M. Lemos, 1990: *Surf-Zone Hydrodynamics*, Centro Internacional de Métodos Numéricos en Ingenieria, Barcelona, 310 p.

[4] Arcilla, A.S., J.A. Roelvink, B.A. O'Connor, A.J.H.M. Reniers and J.A. Jimenez, 1994: The Delta flume '93 experiment, *Proc. Coastal Dynamics Conf. '94*, 488-502

[5] Ardhuin, F., Rogers, E., Babanin, A.V., Filipot, J.F., Magne, R., Roland, A., Van der Westhuysen, A., Queffeulou, P., Lefevre, J.M., Aouf, L., Collard, F., 2010: Semiempirical dissipation source functions for ocean waves. Part I: definition, calibration, and validation. *J. Phys. Oceanogr.* **40**, 1917-1941.

[6] Banner, M.L. and I.R. Young, 1994: Modelling spectral dissipation in the evolution of wind waves. Part I: Assessment of existing model performance, *J. Phys. Oceanogr.*, **24**, No. 7, 1550-1571

[7] R. Barrett, M. Berry, T.F. Chan, J. Demmel, J. Donato, J. Dongarra, V. Eijkhout, R. Pozo, C. Romine, H. van der Vorst, Templates for the solution of linear systems: Building blocks for iterative methods, SIAM, Philadelphia, PA, 1994, accessible from *http://www.netlib.org/templates/Templates.html*.

[8] P. Bastian, G. Horton, Parallelization of robust multi-grid methods: ILU factorization and frequency decomposition method, SIAM J. Sci. Stat. Comput. 12 (1991) 1457–1470.

[9] Battjes, J.A. and J.P.F.M. Janssen, 1978: Energy loss and set-up due to breaking of random waves, *Proc. 16th Int. Conf. Coastal Engineering*, ASCE, 569-587

[10] Battjes, J.A. and G.Ph. van Vledder, 1984, Verification of Kimura's theory for wave group statistics, *Proc. 19th Int. Conf. Coastal Engineering*, ASCE, Houston, 642-648

126

[11] Battjes, J.A. and M.J.F. Stive, 1985: Calibration and verification of a dissipation model for random breaking waves, *J. Geophys. Res.*, **90**, No. C5, 9159-9167

[12] Battjes, J.A. and S. Beji, 1992: Breaking waves propagating over a shoal, *Proc. 23*[rd] *Int. Conf. Coastal Engineering*, ASCE, 42-50

[13] Battjes, J.A., 1994: Shallow water wave modelling, M. Isaacson and M. Quick (Eds.), *Proc. Waves-Physical and Numerical Modelling*, University of British Columbia, Vancouver, 1-24

[14] Beji, S. and J.A. Battjes 1993: Experimental investigation of wave propagation over a bar, *Coastal Engineering*, **19**, 151-162

[15] Bender, L.C., 1996, Modification of the physics and numerics in a third-generation ocean wave model, *J. Atm. and Ocean. Techn.*, 13, 3, 726-750

[16] Bidlot, J.-R., B. Hansen and P.A.E.M. Janssen, 1996: Wave modelling and operational forecasting at ECMWF, *1*[st] *International Conference on EuroGOOS*, 7-11 October, 1996, The Hague, 206-213

[17] Benoit, M., F. Marcos and F. Becq, 1996: Development of a third-generation shallow-water wave model with unstructured spatial meshing. *Proc. 25*[th] *Int. Conf. Coastal Engineering*, ASCE, Orlando, 465-478

[18] Benoit, M., 2005: Evaluation of methods to compute the non-linear quadruplet interactions for deep-water wave spectra, *Proc. 5th Int. Symp. WAVES 2005*, Madrid, Spain

[19] Berkhoff, J.C.W., 1972: Computation of combined refraction-diffraction, *Proc. 13*[th] *Int. Conf. Coastal Engineering*, ASCE, 471-490

[20] Bertotti, L and L. Cavaleri, 1994: Accuracy of wind and wave evaluation in coastal regions, *Proc. 24*[th] *Int. Conf. Coastal Engineering*, ASCE, 57-67

[21] Booij, N., and L.H. Holthuijsen, 1987, Propagation of ocean waves in discrete spectral wave m*odels, Journal of Computational Physics*, vol. 68, 307-326.

[22] Booij, N., L.H. Holthuijsen and P.H.M. de Lange, 1992, The penetration of short-crested waves through a gap, *Proc. 23rd Int. Conf. Coastal Eng*, Venice 4-9 Oct., 1992, New York, 1993, 1044-1052

[23] Booij, N., L.H. Holthuijsen and R.C. Ris, 1996: The "SWAN" wave model for shallow water, *Proc. 25th Int. Conf. Coastal Engng.*, Orlando, 668-676

[24] Booij, N., L.H. Holthuijsen and R. Padilla-Hernandez, 1997: A nonstationary, parametric coastal wave model, *Conf. Coastal Dynamics '97*, Plymouth, 99-107

[25] Booij, N., L.H. Holthuijsen and R. Padilla-Hernandez, 1997: Numerical wave propagation on a curvilinear grid, *Proceedings 3rd International Symposium on Ocean Wave Measurement and Analysis, WAVES '97*, ASCE, 286-294

[26] Booij, N., L.H. Holthuijsen and R.C. Ris, 1998: Shallow water wave modelling, *Oceanology International 98, The Global Ocean, Brighton, Conference Proceedings*, 3, 483-491

[27] Booij, N., L.H. Holthuijsen and IJ.G. Haagsma, 1998: Comparing the second-generation HISWA wave model with the third-generation SWAN wave model, *5th International Workshop on Wave Hindcasting and Forecasting*, Melbourne, Florida, 215-222

[28] Booij, N., R.C. Ris and L.H. Holthuijsen, 1999, A third-generation wave model for coastal regions, Part I, Model description and validation, *J.Geoph.Research*, 104, C4, 7649-7666

[29] Booij, N., L.H. Holthuijsen and J.A. Battjes, 2001: Ocean to near-shore wave modelling with SWAN, *4th International Conference on Coastal Dynamics 2001*, Lund, Sweden, 335-344

[30] Booij, N., L.H. Holthuijsen and IJ.G. Haagsma, 2001: The effect of swell on the generation and dissipation of waves, *4th International Symposium on Ocean Wave Measurements and Analysis WAVES 2001*, San Francisco, 501-506

[31] Botta, E.F.F. and M.H.M. Ellenbroek, 1985: A modified SOR method for the Poisson equation in unsteady free-surface flow calculations, *J. Comput. Phys.*, **60**, 119-134

[32] Bouws, E. and J.A. Battjes, 1982: A Monte-Carlo approach to the computation of refraction of water waves, *J. Geophys. Res.*, **87**, 5718-5722

[33] Bouws, E. and G.J. Komen, 1983: On the balance between growth and dissipation in an extreme, depth-limited wind-sea in the southern North Sea, *J. Phys. Oceanogr.*, **13**, 1653−1658

[34] Burnside, W., 1915: On the modification of a train of waves as it advances into shallow water, *Proceedings of the London Mathematical Society*, Series 2, **14**, 131−133

[35] Campbell, T., J. Cazes, E. Rogers, Implementation of an important wave model on parallel architectures, in: Oceans 2002 MTS/IEEE Conference, IEEE, 2002, pp. 1509–1514, available from *http://www7320.nrlssc.navy.mil/mts2002/PDF/campbell-paper.pdf.*

[36] Cardone, V.J., W.J. Pierson and E.G. Ward, 1976: Hindcasting the directional spectra of hurricane-generated waves, *J. Petr. Techn.*, **28**, 385-394

128

[37] Cavaleri, L. and P. Malanotte-Rizzoli, 1981: Wind wave prediction in shallow water: Theory and applications. *J. Geophys. Res.*, **86**, No. C11, 10,961-10,973

[38] Cavaleri, L. and L.H. Holthuijsen, 1998: Wave modelling in the WISE group, *Proc. 26th Int. Conf. Coastal Engng.*, Copenhagen, 498-508

[39] CERC, 1973: Shore Protection Manual, U.S. Army Corps of Engineers, Techn. Rep. No. 4, Vol. I

[40] Chen, Y. and H. Wang, 1983: Numerical model for nonstationary shallow water wave spectral transformations, *J. Geophys. Res.*, **88**, 9851-9863

[41] Chen, Y., R.T. Guza, and S. Elgar, 1997: Modelling of breaking surface waves in shallow water, *J. Geophys. Res.*, 102, C11, 25035-25046

[42] Chrisochoides, N.P., E.N. Houstis, J.R. Rice, Mapping algorithms and software environment for data parallel PDE iterative solvers, J. Parallel and Distr. Comput. 21 (1994) 75–95.

[43] Collins, J.I., 1972: Prediction of shallow water spectra, *J. Geophys. Res.*, **77**, No. 15, 2693-2707

[44] Collins, C.O., and W.E. Rogers, 2017: A Source Term for Wave Attenuation by Sea ice in WAVEWATCH III: IC4, NRL Report NRL/MR/7320–17-9726, 25 pp. (available from www7320.nrlssc.navy.mil/pubs.php).

[45] Dalrymple, R.A., J.T. Kirby and P.A. Hwang, 1984: Wave diffraction due to areas of energy dissipation, *Journal of Waterways, Ports, Harbours and Coastal Engineering*, **110**, 67-79

[46] d'Angremond, K., J.W. van der Meer and R.J. de Jong, 1996: Wave transmission at low-crested structures, *Proc. 25th Int. Conf. Coastal Engng.*, ASCE, Orlando, 2418-2427

[47] Dietrich, C. et al., 2011. Modeling hurricane waves and storm surge using integrally-coupled, scalable computations, *Coast. Engng.*, **58**, 45-65.

[48] Dietrich, C. et al., 2013. Limiters for spectral propagation velocities in SWAN, *Ocean Modelling*, **70**, 85-102

[49] Dingemans, M.W., A.C. Radder and H.J. de Vriend, 1978: Computations of the driving forces of wave-induced currents, *Coastal Engng.*, 11, 539-563

[50] De Waal, J.P., 2001. Wave growth limit in shallow water. Proc. 4th Int. Symp. Waves 2001, pp. 560–569.

[51] Dingemans, M.W., 1997: Water wave propagation over uneven bottoms. Part 1 -linear wave propagation, *Advanced Series on Ocean Engineering*, 13, World Scientific, 471 p.

[52] Doble, M. J., De Carolis, G., Meylan, M.H., Bidlot, J.-R. and Wadhams, P., 2015. Relating wave attenuation to pancake ice thickness, using field measurements and model results, *Geophys. Res. Lett.*, **42**, 4473-4481, doi:10.1002/2015GL063628.

[53] Donelan, M.A., A.V. Babanin, I.R. Young, and M.L. Banner, 2006: Wave follower field measurements of the wind input spectral function. Part II: Parameterization of the wind input. *J. Phys. Oceanogr.*, **36**, 1672-1688.

[54] Eldeberky, Y., 1996: Nonlinear transformation of wave spectra in the nearshore zone, *Ph.D. thesis*, Delft University of Technology, Department of Civil Engineering, The Netherlands

[55] Eldeberky, Y. and J.A. Battjes, 1995: Parameterization of triad interactions in wave energy models, *Proc. Coastal Dynamics Conf. '95*, Gdansk, Poland, 140-148

[56] Eldeberky, Y. and J.A. Battjes, 1996: Spectral modelling of wave breaking: Application to Boussinesq equations, *J. Geophys. Res.*, **101**, No. C1, 1253-1264

[57] Elgar, S. and R.T. Guza, 1986: Nonlinear model predictions of bispectra of shoaling surface gravity waves, *J. Fluid Mech.*, 167, 1-18

[58] Elgar, S., R.T. Guza, B. Raubenheimer, T.H.C. Herbers and E.L. Gallagher, 1997: Spectral evolution of shoaling and breaking waves on a barred beach, *J. Geophys. Res.*, 102,C7, 15797-15805

[59] Ewing, J.A., 1971: A numerical wave prediction method for the North Atlantic Ocean, *Deutsch. Hydrogr. Z.*, **24**, No. 6, 241−261

[60] Ewing, J.A. and R.C. Hague, 1993: A second-generation wave model for coastal wave prediction, *Proc. of 2$^{nd}$ Int. Symposium on Ocean Wave Measurement and Analysis*, New Orleans, 576-589

[61] Fan, Y., S-J Lin, I.M. Held, Z. Yu, and H. Tolman, 2012: Global ocean surface wave simulation using a coupled atmosphere-wave model, *J. of Climate*, **25**, 6233-6252.

[62] Ferziger, J.H. and Perić, M., 1999. Computational methods for fluid dynamics (2nd edition). Springer-Verlag, Berlin.

[63] G.C. Fox, A review of automatic load balancing and decomposition methods for the hypercube, in: M. Schulz (Ed.), Numerical Algorithms for Modern Parallel Computer Architectures, Springer, Verlag, 1988, pp. 63–76, IMA volume 13.

130

[64] Freilich, M.H. and R.T. Guza, 1984: nonlinear effects on shoaling surface gravity waves, *Phil. Trans. R. Soc. London,* A 311, 1-41

[65] Galvin, C.J., 1972: Wave breaking in shallow water, *Waves on beaches and resulting sediment transport*, Academic Press Inc., 413-455

[66] Gear, C.W., 1971. *Numerical initial value problems in ordinary differential equations*, Prentice-Hall.

[67] Gelci, R., H. Cazalé and J. Vassal, 1956: Utilization des diagrammes de propagation à la prévision énergétique de la houle, *Bulletin d'information du Comité Central d'océanographie et d'études des côtes*, **8**, No. 4, 160-197 (in French)

[68] Goda, Y., H. Takeda and Y. Moriya, 1967: Laboratory investigation of wave transmission over breakwaters*, Rep. port and Harbour Res. Inst.*, 13 (from Seelig, 1979)

[69] Golding, B.W., 1983: A wave prediction system for real-time sea state forecasting, *J. R. Met. Soc.*, **109**, 393-416

[70] Golub, G.H. and C.F. van Loan, 1986: Matrix Computations, North Oxford Academic, London, 476 p.

[71] Gorman, R.M. and C.G. Neilson, 1999: Modelling shallow water wave generation and transformation in an intertidal estuary, *Coastal Engineering*, 36, 197-217

[72] W. Gropp, E. Lusk, A. Skjellum, Using MPI: Portable parallel programming with the Messing Passing Interface, MIT Press, Cambridge, MA, 1999.

[73] Günther, H., S. Hasselmann and P.A.E.M. Janssen, 1992: The WAM model Cycle 4 (revised version), *Deutsch. Klim. Rechenzentrum, Techn. Rep. No. 4*, Hamburg, Germany

[74] Hargreaves, J.C. and Annan, J.D., 2001. Comments on "Improvement of the short-fetch behavior in the wave ocean model (WAM)". J. Atmos. Oceanic Techn., 18: 711–715.

[75] Hashimoto, N., IJ.G. Haagsma and L.H. Holthuijsen, 2002: Four-wave interactions in SWAN, *Proc. 28*[th] *Int. Conf. Coastal Engng.*, ASCE, Cardiff, 392-404

[76] Hasselmann, K., 1960: Grundgleichungen der Seegangsvoraussage, *Schiffstechnik*, 1, 191−195

[77] Hasselmann, K., 1962: On the non-linear transfer in a gravity wave spectrum, part 1. General theory, *J. Fluid Mech.*, **12**, 481-500

[78] Hasselmann, K., 1963a: On the non-linear transfer in a gravity wave spectrum, part 2. Conservation theory, wave-particle correspondence, irreversibility, *J. Fluid Mech.*, **15**, 273-281

[79] Hasselmann, K., 1963b: On the non-linear transfer in a gravity wave spectrum, part 3. Evaluation of energy flux and sea-swell interactions for a Neuman spectrum, *J. Fluid Mech.*, **15**, 385-398

[80] Hasselmann, K. and J.I. Collins, 1968: Spectral dissipation of finite-depth gravity waves due to turbulent bottom friction, *J. Mar. Res.*, **26**, 1-12

[81] Hasselmann, K., T.P. Barnett, E. Bouws, H. Carlson, D.E. Cartwright, K. Enke, J.A. Ewing, H. Gienapp, D.E. Hasselmann, P. Kruseman, A. Meerburg, P. Müller, D.J. Olbers, K. Richter, W. Sell and H. Walden, 1973: Measurements of wind−wave growth and swell decay during the Joint North Sea Wave Project (JONSWAP), *Dtsch. Hydrogr. Z.* Suppl., **12**, A8

[82] Hasselmann, K., 1974: On the spectral dissipation of ocean waves due to whitecapping, *Bound.-layer Meteor.*, **6**, 1-2, 107-127

[83] Hasselmann, K., D.B. Ross, P. Müller and W. Sell, 1976: A parametric wave prediction model, *J. Phys. Oceanogr.*, **6**, 200−228

[84] Hasselmann, S. and K. Hasselmann, 1981: A symmetrical method of computing the non-linear transfer in a gravity-wave spectrum, *Hamburger Geophys. Einzelschr.*, Serie A., 52, 8

[85] Hasselmann, S., K. Hasselmann, J.H. Allender and T.P. Barnett, 1985: Computations and parameterizations of the nonlinear energy transfer in a gravity wave spectrum. Part II: Parameterizations of the nonlinear transfer for application in wave models, *J. Phys. Oceanogr.*, **15**, 11, 1378-1391

[86] Hedges, T.S., 1987: Combination of waves and currents: an introduction, *Proc. Instn. Civ. Engrs.*, Part 1, **82**, 567-585

[87] Hersbach, H. and Janssen, P.A.E.M., 1999. Improvement of the short-fetch behavior in the wave ocean model (WAM). J. Atmos. Oceanic Techn., 16: 884–892.

[88] Herterich, K. and K. Hasselmann, 1980: A similarity relation for the nonlinear energy transfer in a finite-depth gravity-wave spectrum, *J. Fluid Mech.*, **97**, 215-224

[89] Holthuijsen, L.H., 1980: Methods of wave prediction, part I and II (Methoden voor golfvoorspelling, deel I en II, in Dutch), Technical Advisory Commission against Inundation (Technische Adviescommissie voor de Waterkeringen, in Dutch), Den Haag, The Netherlands

[90] Holthuijsen, L.H. and S. De Boer, 1988: Wave forecasting for moving and stationary targets, *Computer modelling in Ocean Engineering*, Eds. B.Y. Schrefler and O.C. Zienkiewicz, Balkema, Rotterdam, The Netherlands, 231-234

132

[91] Holthuijsen, L.H., Booij, N. and T.H.C. Herbers, 1989: A prediction model for stationary, short-crested waves in shallow water with ambient currents, *Coastal Engineering*, **13**, 23-54

[92] Holthuijsen, L.H., N. Booij and R.C. Ris, 1993: A spectral wave model for the coastal zone, *Proceedings 2nd International Symposium on Ocean Wave Measurement and Analysis*, New Orleans, Louisiana, July 25−28, 1993: New York, pp. 630−641

[93] Holthuijsen, L.H., N. Booij and L. Bertotti, 1996: The propagation of wind errors through ocean wave hindcasts, *J. Offshore Mech. And Arctic Eng.*, **118**, 184-189

[94] Holthuijsen, L.H., N. Booij and R. Padilla-Hernandez, 1997: A curvilinear, third-generation coastal wave model, *Conf. Coastal Dynamics '97*, Plymouth, 128-136

[95] Holthuijsen, L.H., N. Booij, R. Ris, J.H. Andorka Gal and J.C.M. de Jong, 1997: A verification of the third-generation wave model "SWAN" along the southern North Sea coast, *Proceedings 3rd International Symposium on Ocean Wave Measurement and Analysis, WAVES '97*, ASCE, 49-63

[96] Holthuijsen, L.H., 1998: The concept and features of the ocean wave spectrum, Provision and engineering/operational application of ocean wave spectra, *COST Conference*, UNESCO, 21-25 sept., Paris, keynote address, 11-20

[97] Holthuijsen, L.H., 1998: Waves in shallow water, *World Meteorological Organization Guide to wave analysis and forecasting*, WMO-N0. 702, Chapter 7, 81-88

[98] Holthuijsen, L.H., R.C. Ris and N. Booij, 1998: A verification of the third-generation wave model SWAN, *5th International Workshop on Wave Hindcasting and Forecasting*, Melbourne, Florida, 223-230

[99] Holthuijsen, L.H., N. Booij and IJ.G. Haagsma, 1998: Comparing 1$^{st}$-, 2$^{nd}$ - and 3$^{rd}$-generation coastal wave modelling, *26th Int. Conf. Coastal Engng.*, Copenhagen, 140-149

[100] Holthuijsen, L.H. and N. Booij, 2000: Oceanic and near-shore whitecapping effects in SWAN, 6$^{th}$ Int. Workshop on Wave Hindcasting and Forecasting, Monterey, 362-368

[101] Holthuijsen, L.H, R.C. Ris, N. Booij and E. Cecchi, 2000: Swell and whitecapping, a numerical experiment, Proc. 27th Int. Conf. Coastal Engng., Sydney, 346-354

[102] Holthuijsen, L.H., Herman, A. and Booij, N., 2003: Phase-decoupled refraction-diffraction for spectral wave models, *Coastal Engineering*, **49**, 291-305

[103] Holthuijsen, L.H., 2007: *Waves in oceanic and coastal waters*, Cambridge University Press.

[104] Hsu, T.-W., S.-H. Ou and J.-M. Liau, 2005: Hindcasting nearshore wind waves using a FEM code for SWAN, *Coastal Engineering*, **52**, 177-195

[105] Jacobsen, N.G., B.C. McFall and D.A. van der A, 2019: A frequency distributed dissipation model for canopies, *Coast. Engng.*, **150**, 135-146

[106] Janssen, P.A.E.M., 1989: Wave induced stress and the drag of air flow over sea waves, *J. Phys. Oceanogr.*, **19**, 745-754

[107] Janssen, P.A.E.M., 1991a: Quasi-linear theory of wind-wave generation applied to wave forecasting, *J. Phys. Oceanogr.*, **21**, 1631-1642

[108] Janssen, P.A.E.M., 1991b: Consequences of the effect of surface gravity waves on the mean air flow, *Int. Union of Theor. and Appl. Mech.* (IUTAM), Sydney, Australia, 193-198

[109] Jonsson, I.G. 1966: Wave boundary layers and friction factors, *Proc. 10*[th] *Int. Conf. Coastal Engineering*, ASCE, 127-148

[110] Jonsson, I.G., 1980: A new approach to rough turbulent boundary layers, *Ocean Engineering*, **7**, 109-152

[111] Jonsson, I.G., 1993: *The Sea*, Ocean Engineering Science, **9**, Part A

[112] Jonsson, I.G. and N.A. Carlsen, 1976: Experimental and theoretical investigations in an oscillatory turbulent boundary layer, *J. Hydraulic Research*, **14**, 45-60

[113] Kahma, K.K. and C.J. Calkoen, 1992: Reconciling discrepancies in the observed growth of wind−generated waves, *J. Phys. Oceanogr.*, **22**, 1389−1405

[114] Kaminsky, G.M. and N.C. Kraus, 1993: Evaluation of depth-limited wave breaking criteria, *Proc. of 2*[nd] *Int. Symposium on Ocean Wave Measurement and Analysis*, New Orleans, 180-193

[115] Karlson, T, 1969: Refraction of continuous ocean wave spectra, *Journal of Waterways, Ports, Harbours and Coastal Engineering*, **95**, 275-287

[116] Kirby, J.T., 1986: Higher-order approximation in the parabolic equation method for water waves, *J. Geophys. Res.*, **91**, C1, 933-952

[117] Komen, G.J., S. Hasselmann, and K. Hasselmann, 1984: On the existence of a fully developed wind-sea spectrum, *J. Phys. Oceanogr.*, **14**, 1271-1285

[118] Komen, G.J., Cavaleri, L., Donelan, M., Hasselmann, K., Hasselmann, S. and P.A.E.M. Janssen, 1994: *Dynamics and Modelling of Ocean Waves*, Cambridge University Press, 532 p.

134

[119] Kuik, A.J., G.Ph. van Vledder and L.H. Holthuijsen, 1988: A method for the routine analysis of pitch-and-roll buoy wave data, *J. Phys. Oceanogr.*, **18**, 1020-1034

[120] Li, C.W. and M. Mao, 1992: Spectral modelling of typhoon-generated waves in shallow waters, *J. Hydraulic Research*, **30**, 5, 611-622

[121] Lin, R.Q. and N.E. Huang, 1996: The Goddard coastal wave model. Part I: Numerical method, *J. Phys. Oceanogr.*, **26**, 833-847

[122] Lin, S.-J. and R.B. Rood, 1996: Multidimensional flux-form semi-Lagrangian transport schemes, *Monthly Weather Review*, **124**, 2046-2070

[123] Liu, P.L., S.B. Yoon and J.T. Kirby, 1985: Nonlinear refraction-diffraction of waves in shallow water, *J. Fluid Mech.*, 153, 185-201

[124] Liu, Q., Rogers, W.E., Babanin, A., Li, J., and Guan, C., 2020. Spectral modelling of ice-induced wave decay, *J. Phys. Oceanogr.*, https://doi.org/10.1175/JPO-D-19-0187.1

[125] Luo, W. and J. Monbaliu, 1994: Effects of the bottom friction formulation on the energy balance for gravity waves in shallow water, *J. Geophys. Res.*, **99**, C9, 18,501-18,511

[126] Madsen, O.S., Y.-K. Poon and H.C. Graber, 1988: Spectral wave attenuation by bottom friction: Theory, *Proc. 21*[th] *Int. Conf. Coastal Engineering*, ASCE, 492-504

[127] Madsen, P.A. and O.R. Sørensen, 1992: A new form of the Boussinesq equations with improved linear dispersion characteristics. Part 2: A slowly-varying bathymetry, *Coastal Engineering*, **18**, 183-205

[128] Madsen, P.A. and O.R. Sørensen, 1993: Bound waves and triad interactions in shallow water, *Ocean Engineering,* **20**, 4, 359-388

[129] Mase, H. and J.T. Kirby, 1992: Hybrid frequency-domain KdV equation for random wave transformation, *Proc. 23*[th] *Int. Conf. Coastal Engineering*, ASCE, 474-487

[130] Mastenbroek, C., G. Burgers, and P.A.E.M. Janssen, 1993: The dynamical coupling of a wave model in a storm surge model through the atmospheric boundary layer, *J. Phys. Oceanogr.*, **23**, 1856-1866

[131] Van der Meer, J.W., R. Briganti, B. Zanuttigh and B. Wang, 2005: Wave transmission and reflection at low-crested structures: design formulae, oblique wave attack and spectral change, *Coast. Engng.*, **52**, 915-929

[132] Mendez, F.J. and I.J. Losada, 2004: An empirical model to estimate the propagation of random breaking and nonbreaking waves over vegetation fields, *Coast. Engng.*, **51**, 103-118

[133] Mei, C.C., 1983: *The applied dynamics of ocean surface waves*, Wiley, New York, 740 p.

[134] G. Meurant, Domain decomposition methods for partial-differential equations on parallel computers, Int. J. Supercomputer Appl. and High Perform. Comput. 2 (4) (1988) 5–12.

[135] Meylan, M., L. G. Bennetts, and A. L. Kohout, 2014: In situ measurements and analysis of ocean waves in the Antarctic marginal ice zone, *Geophys. Res. Lett.*, **41**, 5046-5051, doi:10.1002/2014GL060809.

[136] Meylan, M.H., Bennetts, L.G., Mosig, J.E.M., Rogers, W.E., Doble, M.J. and Peter, M.A., 2018. Dispersion relations, power laws, and energy loss for waves in the marginal ice zone, *J. Geophys. Res.*, **123**, 3322-3335. https://doi.org/10.1002/2018JC013776.

[137] Miles, J.W., 1957: On the generation of surface waves by shear flows, *J. Fluid Mech.*, **3**, 185−204

[138] Miles, J.W., 1981: Hamiltonian formulations for surface waves, *Applied Scientific Research*, **37**, 103-110

[139] Nelson, R.C., 1987: Design wave heights on very mild slopes: An experimental study, *Civil. Eng. Trans., Inst. Eng. Aust.*, **29**, 157-161

[140] Nelson, R.C., 1994: Depth limited design wave heights in very flat regions, *Coastal Engineering*, **23**, 43-59

[141] Nelson, R.C., 1997: Height limits in top down and bottom up wave environments, *Coastal Engineering*, **32**, 247-254

[142] Nwogu, O., 1994: Nonlinear evolution of directional wave spectra in shallow water, *Proc. 24*[th] *Int. Conf. Coastal Engineering*, ASCE, 467-481

[143] OpenMP ARB, OpenMP, *http://www.openmp.org*.

[144] Padilla-Hernandez, R., P. Osuna, J. Monbaliu and L. Holthuijsen, 1998: Intercomparing third-generation wave model nesting, *5th International Workshop on Wave Hindcasting and Forecasting*, Melbourne, Florida, 102-112

[145] Peregrine, D.H., 1966: Long waves on a beach, *J. Fluid Mech.*, **27**, 4, 815-827

[146] Phillips, O.M., 1957: On the generation of waves by turbulent wind, *J. Fluid Mech.*, **2**, 417−445

[147] Phillips, O.M., 1960: On the dynamics of unsteady gravity waves of finite amplitude. Part 1, *J. Fluid Mech.*, **9**, 193-217

136

[148] Phillips, O.M., 1977: *The dynamics of the upper ocean*, Cambridge University Press, 336 p.

[149] Phillips, O.M., 1985: Spectral and statistical properties of the equilibrium range in wind-generated gravity waves, *J. Fluid Mech.*, **156**, 505-531

[150] Pierson, W.J. and L. Moskowitz, 1964: A proposed spectral form for fully developed wind seas based on the similarity theory of S.A. Kitaigorodskii, *J. Geophys. Res.*, **69**, 24, 5181-5190

[151] Piest, J., 1965: Seegangsbestimmung und Seegangsrefraktion in einem Meer mit nicht- ebenem Boden; eine theoretische Untersuchung, *Deutsch. Hydrogr. Z.*, **18**: 67-74 (in German)

[152] Press, W.H., Flannery, B.P., Teukolsky, S.A. and Vetterling, W.T., 1993. Numerical recipes in Fortran 77. The art of scientific computing (2nd edition). Cambridge University Press, New York (available from *http://www.nr.com*).

[153] Putnam, J.A. and J.W. Johnson, 1949: The dissipation of wave energy by bottom friction, *Trans. Am. Geoph. Union*, **30**, 67-74

[154] Radder, A.C., 1979: On the parabolic equation method for water-wave propagation, *J. Fluid Mech.*, **95**, 159-176

[155] Radder, A.C., 1992: An explicit Hamiltonian formulation of surface waves in water of finite depth, *J. Fluid Mech.*, **237**, 435-455

[156] Radder, A.C., 1996: Hamiltonian dynamics of water waves, *Advances of Coastal and Ocean Engineering*, World Scientific, **4**, ??-??

[157] Resio, D. and W. Perrie, 1991: A numerical study of nonlinear energy fluxes due to wave-wave interactions. Part I: Methodology and basic results, *J. Fluid Mech.*, **223**, 609-629

[158] Resio, D.T., J.H. Pihl, B.A. Tracy and C.L. Vincent, 2001: Nonlinear energy fluxes and the finite depth equilibrium range wave spectra, *J. Geophys. Res.*, **106**, C4, 6985-7000.

[159] Resio, D.T., C.E. Long and C.L. Vincent, 2004: Equilibrium-range constant in wind-generated wave spectra, *J. Geophys. Res.*, **109**, C01018.

[160] Ris, R.C., L.H. Holthuijsen and N. Booij, 1994: A spectral model for waves in the near shore zone, *Proc. 24th Int. Conf. Coastal Engng*, Kobe, Japan, pp. 68-78

[161] Ris, R.C. and L.H. Holthuijsen, 1996: Spectral modelling of current wave-blocking. *Proc. 25*[th] *Int. Conf. Coastal Engng.*, ASCE, 1247-1254.

[162] Ris, R.C. and L.H. Holthuijsen, 1997: Modelling of current induced wave-blocking in a spectral wave model, $8^{th}$ *International Biennal Conference on Physics of Estuaries and Coastal Seas*, J. Dronkers and M.B.A.M. Scheffers (eds.), The Hague, 139-144

[163] Ris, R.C., 1999. Model convergence of SWAN in the Westerschelde estuary. WL|Delft Hydraulics, Report H3496.

[164] Ris, R.C., N. Booij and L.H. Holthuijsen, 1999: A third-generation wave model for coastal regions, Part II: Verification, *J. Geophys. Res.*, 104, C4, 7667-7681

[165] Ris, R., L.H. Holthuijsen, J.M. Smith, N. Booij and A.R. van Dongeren, 2002: The ONR virtual testbed for coastal and oceanic wave models, *Proc. 28th Int. Conf. Coastal Engng.*, ASCE, Cardiff, 380-391

[166] Roache, P.J., 1972: *Computational Fluid Dynamics*, Hermosa Publishers, Albuquerque, 446 p.

[167] Rogers, W.E., J.M. Kaihatu, H.A. H. Petit, N. Booij, and L.H. Holthuijsen, 2002: Diffusion reduction in a arbitrary scale third generation wind wave model, *Ocean Engng.*, **29**, 1357-1390.

[168] Rogers, W.E., P.A. Hwang and D.W. Wang, 2003: Investigation of wave growth and decay in the SWAN model: three regional-scale applications, *J. Phys. Oceanogr.*, **33**, 366-389.

[169] Rogers, W.E., J.M. Kaihatu, L. Hsu, R.E. Jensen, J.D. Dykes and K.T. Holland, 2007: Forecasting and hindcasting waves with the SWAN model in the Southern California Bight, *Coastal Engineering*, **54**, 1-15.

[170] Rogers, W.E., A.V. Babanin, D.W. Wang, 2012: Observation-consistent input and whitecapping-dissipation in a model for wind-generated surface waves: Description and simple calculations, *J. Atmos. Oceanic Tech.*, **29(9)**, 1329-1346.

[171] Rogers, W.E., J. Thomson, H.H. Shen, M.J. Doble, P. Wadhams and S. Cheng, 2016: Dissipation of wind waves by pancake and frazil ice in the autumn Beaufort Sea, *J. Geophys. Res. Oceans*, **121**, 7991-8007, doi:10.1002/2016JC012251.

[172] Rogers, W.E., M.H. Meylan, A.L. Kohout, 2018: Frequency Distribution of Dissipation of Energy of Ocean Waves by Sea Ice Using Data from Wave Array 3 of the ONR "Sea State" Field Experiment. NRL Report NRL/MR/7322–18-9801., 25 pp. (available from www7320.nrlssc.navy.mil/pubs.php).

[173] Rogers, W.E., 2019: Implementation of sea ice in the wave model SWAN, NRL Memorandum Report NRL/MR/7322–19-9874, 25 pp. (available from www7320.nrlssc.navy.mil/pubs.php).

[174] Rogers, W.E., M.H. Meylan, Alison L. Kohout, 2021a. Estimates of spectral wave attenuation in Antarctic sea ice, using model/data inversion, *Cold Reg. Sci. Technol.*, 13 pp., https://doi.org/10.1016/j.coldregions.2020.103198

[175] Rogers, W.E., Yu, J., Wang, D.W., 2021b. Incorporating dependencies on ice thickness in empirical parameterizations of wave dissipation by sea ice, *Technical Report*, NRL/OT/7320-21-5145, 35 pp., https://arxiv.org/abs/2104.01246 .

[176] Roland, A., 2009: Development of WWM II: spectral wave modelling on unstructured meshes. PhD thesis. Darmstadt University.

[177] Ruessink, B.G., D.J.R. Walstra and H.N. Southgate, 2003: Calibration and verification of a parametric wave model on barred beaches, *Coastal Engineering*, **48**, 139-149

[178] Sakai, T., M. Koseki and Y. Iwagaki, 1983: Irregular wave refraction due to current, *J. of Hydr. Eng.*, ASCE, **109**, 9, 1203-1215

[179] Sanders, J.W., 1976: A growth-stage scaling model for the wind-driven sea, *Deutsch. Hydrogr. Z.*, **29**, 136-161

[180] Seelig, W.N., 1979, Effects of breakwaters on waves: laboratory tests of wave transmission by overtopping, *Proc. Conf. Coastal Structures*, 79, 2, 941-961

[181] Shemdin, P., K. Hasselmann, S.V. Hsiao and K. Herterich, 1978: Non−linear and linear bottom interaction effects in shallow water, in: Turbulent Fluxes through the Sea Surface, *Wave Dynamics and Prediction, NATO Conf. Ser.*, **V**, 1, 347−372

[182] Shewchuk, J.R., 1996. Triangle: a two-dimensional quality mesh generator and Delaunay triangulator, version 1.3. Available from: *http://www-2.cs.cmu.edu/ quake/triangle.html.*

[183] Smolarkiewicz, P.K. and J.A. Pudykiewicz, 1992: A class of semi-Lagrangian approximations for fluids, *J. Atmos. Sci.*, **49**, 2082-2096

[184] Snyder, R.L., Dobson, F.W., Elliott, J.A. and R.B. Long, 1981: Array measurement of atmospheric pressure fluctuations above surface gravity waves, *J. Fluid Mech.*, **102**, 1-59

[185] Stelling, G.S. and J.J. Leendertse, 1992: Approximation of convective processes by cyclic AOI methods, *Proceeding 2*[nd] *international conference on estuarine and coastal modeling*, ASCE Tampa, Florida, 771-782

[186] Stone, H.L., 1968: Iterative solution of implicit approximations of multidimensional partial differential equations, *SIAM J. of Numer. Anal.*, **5**, 530−558

[187] Struijs, R., 1994: A multi-dimensional upwind discretization method for the Euler equations on unstructured grids. PhD thesis. Delft University of Technology.

[188] SWAMP group, 1985: *Ocean wave modelling*, Plenum Press, New York and London

[189] Taylor, P.A. and R.J. Lee, 1984: Simple guidelines for estimating wind speed variations due to small-scale topographic features, *Climatol. Bull.*, 18, 3-32

[190] Thornton, E.B. and R.T. Guza, 1983: Transformation of wave height distribution, *J. Geophys. Res.*, **88**, C10, 5925-5938

[191] Tolman, H.L., 1990: Wind wave propagation in tidal seas, *Ph.D. thesis*, Delft University of Technology, Department of Civil Engineering, The Netherlands

[192] Tolman, H.L., 1991: A third-generation model for wind waves on slowly varying, unsteady and inhomogeneous depths and currents, *J. Phys. Oceanogr.*, **21**, 6, 782-797

[193] Tolman, H.J., 1992a: Effects of numerics on the physics in a third-generation wind-wave model, *J. Phys. Oceanogr.*, **22**, 10, 1095-1111

[194] Tolman, H.L., 1992b: An evaluation of expressions for the wave energy dissipation due to bottom friction in the presence of currents, *Coastal Engineering*, **16**, 165-179

[195] Tolman, H. L., 1995: On the selection of propagation schemes for a spectral wind−wave model. *NWS/NCEP Office Note 411*, 30 pp. + figures.

[196] Tolman, H.L., 2002: Distributed-memory concepts in the wave model WAVEWATCH III, *Parallel Comput.*, **28**, 35-52.

[197] Tracy, B. and D.T. Resio, 1982: Theory and calculation of the nonlinear energy transfer between sea waves in deep water. WES Report 11, US Army Corps of Engineers.

[198] Van Vledder, G. Ph., J.G. de Ronde and M.J.F. Stive, 1994: Performance of a spectral wind-wave model in shallow water, *Proc. 24*[th] *Int. Conf. Coastal Engineering*, ASCE, 761-774

[199] Van Vledder, G.Ph., T.H.C. Herbers, R.E. Jensen, D.T. Resio and B. Tracy, 2000: Modelling of non-linear quadruplet wave-wave interactions in operational wave models. *Proc. 27th Int. Conf. on Coastal Engineering*, Sydney, Australia.

[200] Van Vledder, G. Ph. and D.P. Hurdle, 2002: Performance of formulations for whitecapping in wave prediction models, *Proc. OMAE 2002*

[201] Van Vledder, G. Ph. and M. Bottema, 2003: Improved modelling of nonlinear four-wave interactions in shallow water, *Proc. 28*[th] *Int. Conf. Coastal Engineering*, ASCE, 459-471

[202] Van Vledder, G. Ph., 2006: The WRT method for the computation of non-linear four-wave interactions in discrete spectral wave models, *Coast. Engng.*, **53**, 223-242

[203] Vincent, C.L., J.M. Smith and J. Davis, 1994: Parameterization of wave breaking in models, *Proc. of Int. Symp.: Waves - Physical and Numerical Modelling*, Univ. of British Columbia, Vancouver, Canada, M. Isaacson and M. Quick (Eds.), Vol. II, 753-762

[204] Van der Vorst, H.A., 1989: High performance preconditioning, *SIAM J. Sci. Stat. Comput.*, **10**, 1174−1185

[205] WAMDI group, 1988: The WAM model − a third generation ocean wave prediction model, *J. Phys. Oceanogr.*, **18**, 1775−1810

[206] Webb, D.J., 1978: Non-linear transfers between sea waves, *Deep-Sea Res.*, **25**, 279−298

[207] Weber, S.L., 1989: Surface gravity waves and turbulent bottom friction, *Ph.D. thesis*, University of Utrecht, The Netherlands

[208] Weber, S.L., 1991a: Bottom friction for wind sea and swell in extreme depth-limited situations, *J. Phys. Oceanogr.*, **21**, 149-172

[209] Weber, S.L., 1991b: Eddy-viscosity and drag-law models for random ocean wave dissipation, *J. Fluid Mech.*, **232**, 73-98

[210] Wesseling, P., 1992: *An introduction to multigrid methods*, John Wiley and Sons, Chichester.

[211] Wesseling, P., 2001: *Principles of Computational Fluid Dynamics*, Springer-Verlag, Berlin, Heidelberg.

[212] Van der Westhuysen, A.J., 2007: Advances in the spectral modelling of wind waves in the nearshore, *Ph.D. thesis*, Delft University of Technology, Department of Civil Engineering, The Netherlands

[213] Van der Westhuysen, A.J., M. Zijlema and J.A. Battjes, 2007: Nonlinear saturation-based whitecapping dissipation in SWAN for deep and shallow water, *Coast. Engng.*, **54**, 151-170

[214] Wilson, B.W., 1965: Numerical prediction of ocean waves in the North Atlantic for December 1959, *Deutsch. Hydrogr. Z.*, **18**, 3, p. 114-130

[215] WISE Group, 2007. Wave modelling - The state of the art. Progr. Oceanogr., **75**, 603-674

[216] Whitham, G.B., 1974: *Linear and nonlinear waves*, Wiley, New York, 636 p.

[217] Wu, J., 1982: Wind-stress coefficients over sea surface from breeze to hurricane, *J. Geophys. Res.*, **87**, C12, 9704-9706

[218] Yan, L. 1987: An improved wind input source term for third generation ocean wave modelling, *Scientific report* WR-No 87-8, De Bilt, The Netherlands

[219] Yamaguchi, M., 1986: A numerical model of nearshore currents based on a finite amplitude wave theory, *Proc. 20th Int. Conf. Coastal Engineering*, ASCE, 849-863

[220] Yamaguchi, M., 1988: A numerical model of nearshore currents due to irregular waves, *Proc. 21th Int. Conf. Coastal Engineering*, ASCE, 1113-1126

[221] Yamaguchi, M., 1990: A numerical model for refraction computation of irregular waves due to time-varying currents and water depth, *Proc. 22th Int. Conf. Coastal Engineering*, ASCE, 205-217

[222] Young, I.R., 1988: A shallow water spectral wave model, *J. Geophys. Res.*, **93**, C5, 5113-5129

[223] Young, I.R., 1999: Wind generated ocean waves, Eds. R. Bhattacharyya and M.E. McCormick, Ocean Engineering Series, Elsevier, Amsterdam, 288 p.

[224] Young, I.R., and M.L. Banner, 1992: Numerical Experiments on the evolution of fetch limited waves, *Int. Union of Theor. and Appl. Mech. (IUTAM)*, Sydney, Australia, 267-275

[225] Young, I.R. and G. Ph. van Vledder, 1993: A review of the central role of nonlinear interactions in wind-wave evolution, *Phil. trans. R. Soc. London.* A., **342**, 505-524

[226] Young, I.R. and L.A. Verhagen, 1996a: The growth of fetch limited waves in water of finite depth. Part 1: Total energy and peak frequency, *Coastal Engineering*, **29**, 47-78

[227] Young, I.R. and L.A. Verhagen, 1996b: The growth of fetch limited waves in water of finite depth. Part 2: Spectral evolution, *Coastal Engineering*, **29**, 79-99

[228] Young, I.R. and L.A. Verhagen, 1996c: The growth of fetch limited waves in water of finite depth. Part 3: Directional spectra, *Coastal Engineering*, **29**, 101-121

[229] Young, I.R., Babanin, A., Zieger, S., 2013: The decay rate of ocean swell observed by altimeter. *J. Phys. Oceanogr.* **43**, 2322-2333.

[230] Zieger, S., A.V. Babanin, W.E. Rogers, and I.R. Young, 2015: Observation-based source terms in the third-generation wave model WAVEWATCH, *Ocean Modelling*, **96**, 2-25.

[231] Yu, J., W.E. Rogers, D.W. Wang, 2019: A Scaling for Wave Dispersion Relationships in Ice-Covered Waters, *J. Geophys. Res.*, **124**, doi:10.1029/2018JC014870.

[232] Zijlema, M. and Wesseling, P., 1998. Higher-order flux-limiting schemes for the finite volume computation of incompressible flow. Int. J. Comput. Fluid Dyn., **9**, 89-109

142

[233] Zijlema, M., 2005: Parallelization of a nearshore wind wave model for distributed memory architectures, in *Parallel Computational Fluid Dynamics - Multidisciplinary applications*, Eds. G. Winter and A. Ecer and J. Periaux and N. Satofuka and P. Fox, Elsevier Science B.V., Amsterdam, The Netherlands, 207-214

[234] Zijlema, M. and A.J. van der Westhuysen, 2005: On convergence behaviour and numerical accuracy in stationary SWAN simulation of nearshore wind wave spectra. *Coastal Engineering*, **52**, 237-256

[235] Zijlema, M., 2009: Parallel, unstructured mesh implementation for SWAN, *Proc. 31*[th] *Int. Conf. Coastal Engineering*, ASCE, 470-482

[236] Zijlema, M., 2010: Computation of wind-wave spectra in coastal waters with SWAN on unstructured grids. *Coastal Engineering*, **57**, 267-277

[237] Zijlema, M., G.Ph. van Vledder and L.H. Holthuijsen, 2012: Bottom friction and wind drag for wave models. *Coastal Engineering*, **65**, 19-26

[238] Zijlema, M., 2021: Physics-capturing discretizations for spectral wind-wave models, *Fluids*, **6**(2), 52.

# Index